LBL-35448
UC-408

Lawrence Berkeley Laboratory
UNIVERSITY OF CALIFORNIA

High Resolution Electron Diffraction Analysis of Structural Changes Associated with the Photocycle of Bacteriorhodopsin

B.-G. Han
(Ph.D. Thesis)

April 1994

Donner Laboratory

Biology & Medicine Division

Prepared for the U.S. Department of Energy under Contract Number DE-AC03-76SF00098

DISCLAIMER

LBL-35448
UC-408

High Resolution Electron Diffraction Analysis of Structural Changes Associated with the Photocycle of Bacteriorhodopsin

B.-G. Han
Ph.D Thesis

Department of Biophysics
University of California

and

Life Sciences Division
Lawrence Berkeley Laboratory
University of California
Berkeley, California 94720

April 1994

This work was supported by the National Institutes of Health, Grant No. GM36884, through the U.S. Department of Energy under Contract No. DE-AC03-76SF00098.

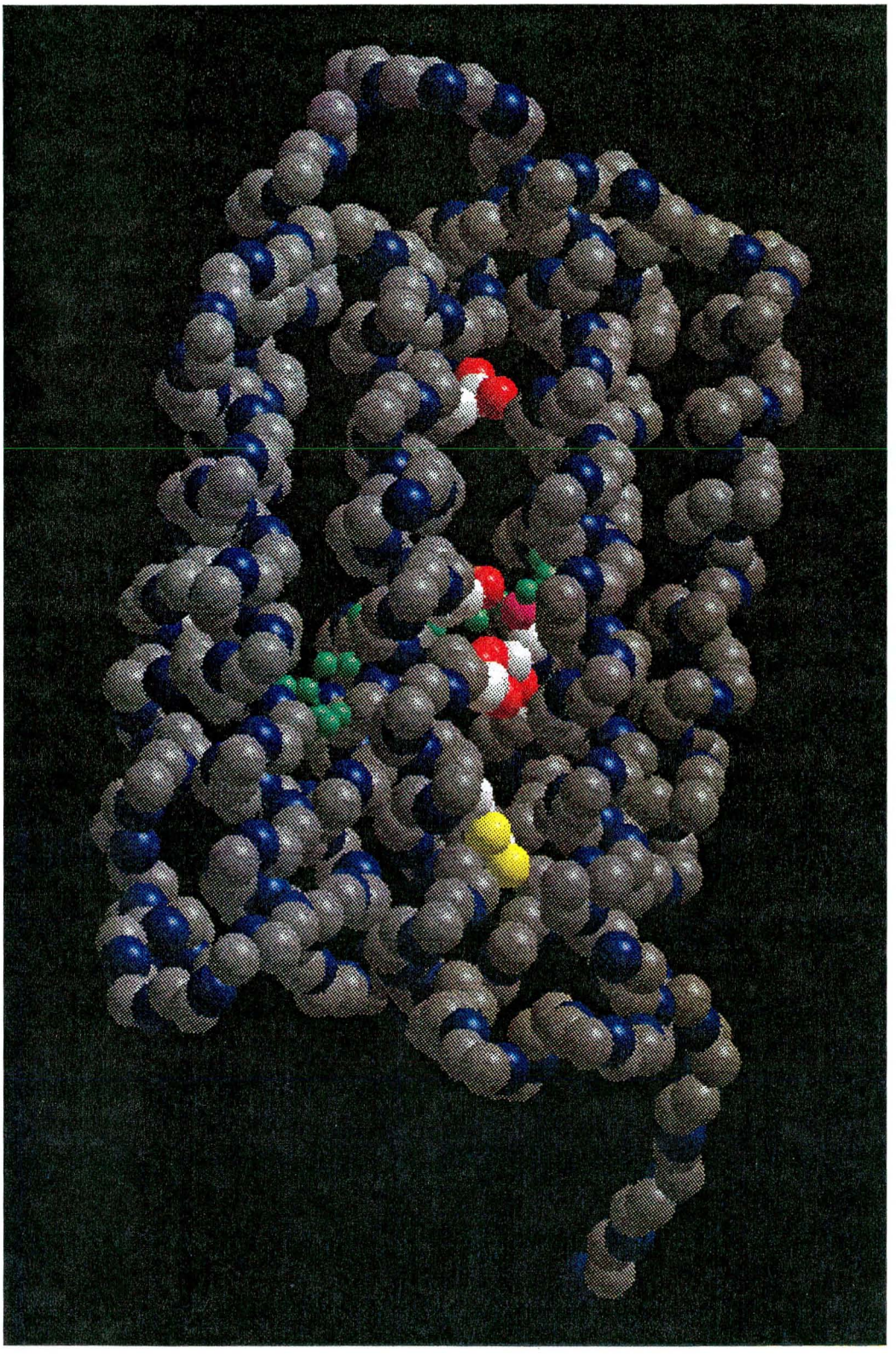

High resolution electron diffraction analysis of structural changes associated with the photocycle of bacteriorhodopsin

by

Bong-Gyoon Han

ABSTRACT

Changes in protein structure that occur during the formation of the M photointermediate of bacteriorhodopsin can be directly visualized by electron diffraction techniques. A modified preparation technique for glucose embedded crystals was employed to ensure sufficient hydration of the crystals, needed for the formation of the M intermediate at low temperature. Samples containing a high percentage of the M intermediate were trapped by rapidly cooling the crystals with liquid nitrogen following illumination with filtered green light at 240K and 260K respectively. Difference Fourier projection maps for M minus bR at two temperatures and for M_{260K} minus M_{240K} are presented. While it is likely that a unique M-substate is trapped when illuminated at 240K, my data indicate that the sample illuminated at 260K produces a mixture of the M_{240K} substate and a second M-substate which may have a protein structure similar to the N-intermediate.

The diffraction data clearly show that statistically significant structural changes occur upon formation of the M_{240K} specimen and then further upon formation of the second substate which is present in the mixture that is produced at 260K.

Imperfect specimen flatness can be a significant limitation in the application of electron crystallography to high resolution structure analysis of purple membranes. Our study shows that the choice of solid carbon stock that is used to make evaporated carbon films can have a very great effect on the preparation of flat specimens of glucose-embedded purple membrane. The degree of purity of the carbon does not seem to be the controlling factor, and other likely factors such as the type of mica used as a substrate, the evaporation apparatus used (and its limiting vacuum), and the use of a continuous versus an interrupted evaporation protocol do not have a discernible influence. The physical or chemical basis for the observed differences in specimen flatness is still unknown; however, the important conclusion at this point is that the choice of evaporating material does have a major effect on the flatness of purple membrane, the specimen used here.

A preliminary 3-D difference map, based on data collected with samples tilted up to 30°, has been constructed at a resolution of 3.5Å parallel to the membrane plane and a resolution of 8.5Å perpendicular to the membrane. The data have been analyzed by a number of different criteria to ensure that the differences seen

reflect real conformational changes at a level which is significantly above the noise in the map. The 3-D difference map shows that there are no significant changes in helix tilt angle and no lateral shifts in helix position, but that there are multiple, small movements throughout the protein, on the scale of individual amino acids. Furthermore, a comparison of the positions of specific backbone and side-chain groups relative to significant difference peaks suggests that it will be necessary to further refine the atomic resolution model before it will be possible to interpret the changes in chemical structure that occur in the protein at this stage of the photocycle.

This thesis is dedicated to my parents, Kyung-Suk,
Woo-Jin and Hye-Jin.

In the beginning was the Word, and the Word was with God, and the Word was God. He was in the beginning with God. All things came into being by Him, and apart from Him nothing came into being that has come into being. In Him was life, and the life was the light of men. And the light shines in the darkness and the darkness did not comprehend it.

ACKNOWLEDGEMENTS

I would like to thank my advisor, Dr. Robert Glaeser, who has encoraged me all along and has given me many scientific insights. He taught me how to do science and what real science is. Without his invaluable help, it would not have been possible to finish my degree including writing this thesis. I would like express my heartfelt gratitude to him.

Dr. Guy A. Perkins' and Dr. Janet Vonck's expertise and help contributed to the success of my electron diffraction work. Dr. Janet Vonck did almost all works of Chapter 4. I would like to thank to Dr. Ken H. Downing. He helped almost every, practical aspect of my work. Dr. Bing Jap has always encouraged me to do good science. Rick Burkard built every instrument for my work. I would like to thank Ed Berry, Thomas Earnest, Felicia Hendrickson, Li-Shar Huang, Theng-King Hwang, Carolyn Larabell, Eva Nogales, Alexander Pertsemlidis, Sharon G. Wolf, and Guangzhou Xu for their practical help and encouragement.

I would like to thank my mother, father, brother and sister for their encouragement. My wife Kyung-Suk deserves special thanks from me. She was a great friend, supporter and encourager. With her love and help, I could endure all hardships. Also, I would like to

thank my spritiual brothers for sharing and nourishing my life at Berkeley.

Finally I give thanks to God for creating this world which is filled with so much beauty, truth and harmony. I have just enjoyed the world which He has created.

TABLE OF CONTENTS

Chapter 1: INTRODUCTION 1

1.1 Structure and function of bacteriorhodopsin 2

1.1.1 Primary and secondary structure 2

1.1.2 Tertiary structure 2

1.1.3 Chromophore retinal 6

1.2 Photocycle of bR 9

1.2.1 Overall scheme of the photocycle 9

1.2.2. Two M substates 12

1.3 Previous diffraction study of the M intermediate 17

1.4 Comparison with halorhodopsin, sensory rhodopsin, and rhodopsin 19

1.4.1. Halorhodopsin 20

1.4.2. Sensory rhodopsin 24

1.4.3. Rhodopsin 25

1.5 Main purpose of dissertation 28

Chapter 2: THEORETICAL AND TECHNICAL ASPECTS OF ELECTRON CRYSTALLOGRAPHY 30

2.1. Electron scattering 31

2.2. Sample preparation and radiation damage 33

2.3. Three dimensional reconstruction of the structure:

projection theorem, hollow cone problem and flatness problem . 35

Chapter 3: EXPERIMENTAL METHODS 39

3.1 Sample preparation 39

3.1.1 Purification and fusion of bR 39

3.1.2 Preparation of specimen grids 40

3.1.3 Trapping of the M intermediate 41

3.2 Electron diffraction data collection and processing 48

3.2.1 Collection of diffraction patterns 48

3.2.2 Densitometry 49

3.2.3 Background subtraction and spot integration 50

Chapter 4: HYDRATION EFFECT 52

4.1 Ice condensation 52

4.2 Difference maps 58

4.3 Summary 67

Chapter 5: DIFFERENCE PROJECTION MAPS OF TWO SUBSTATES OF THE M INTERMEDIATE 68

5.1 Difference Fourier maps 68

5.2 Statistical evaluation 80

5.3 Comparison with previously published data 85

5.4 Discussion 88

Chapter 6: PREPARATION OF FLAT SPECIMENS 102

6.1 Introduction 102

6.2 Preparation methods 105

6.3 Results 108

6.4 Discussion 114

Chapter 7: A PRELIMINARY THREE-DIMENSIONAL DIFFERENCE MAP OF THE M_{240K} INTERMEDIATE 116

7.1 Introduction 116

7.3 Data collection and refinement 117

7.3 Three-dimensional difference Fourier map 130

7.4 Discussion 144

APPENDIX 149

REFERENCES 185

Chapter 1: INTRODUCTION

Bacteriorhodopsin (bR) is an integral membrane protein, found in the purple membrane (PM) of the halophilic bacterium *Halobacterium halobium* (Oesterhelt and Stoeckenius, 1971). bR acts as a light-driven proton pump which generates an electrochemical gradient that mediates ATP synthesis (Danon and Stoeckenius, 1974). When light illuminates bR, protons are pumped from inside to outside to generate an electrochemical potential gradient, as part of the process in which the light activated retinal drives a sequential photocycle. In anaerobic conditions, this bacterium produces PM consisting of bR and lipids in a 3:1 ratio. The PM can occupy, sometimes, 50% of the total cell surface area of this bacterium. In vivo, bR forms a hexagonal crystal lattice (p3), of diameter smaller than 0.5 μm. Each unit cell consists of 3 bR monomers.

1.1 Structure and Function of Bacteriorhodopsin

1.1.1 Primary and secondary structure

Each bR monomer is a single polypeptide, consisting of 248 amino acids with a molecular weight of 26,534 daltons. The primary structure of bR was first determined by sequencing the protein (Khorana et al., 1979). The secondary and tertiary structural organization, made up of seven trans-membrane rods, was first shown by Henderson and Unwin (1975) by electron crystallography, even before the primary structure of bR had been determined.

1.1.2 Tertiary structure

Attempts to obtain bR in the form of three-dimensional crystals needed for X-ray crystallography have failed to produce high quality 3-D crystals which diffract to high resolution, even though some poorly diffracting 3-D crystals have been obtained (Michel and Oesterhelt, 1980). The 3D structure of bR was solved by electron crystallography instead, using 2-D crystals, in the

pioneering work of Henderson et al. (1990) with 3.5 Å resolution parallel and 7 Å resolution perpendicular to the membrane plane. A schematic diagram of the structure, based upon the atomic resolution model, is shown in Figure 1-1. In spite of the relatively low resolution, Henderson et al. could be able to interpret the map in terms of a detailed chain-trace. The large amount of α–helical secondary structures makes interpretation easier, and the large body of structure-function correlations available from mutant studies and spectroscopy added a large amount of further structural information that guided the construction of the chain-trace.

Each bR monomer contains 7 transmembrane alpha helices, named A, B, C, D, E, F and G from the N terminus to the C terminus. Except helix D, all helices contain bulky residues, making it easier to interpret the electron density map. There exists a slight kinking at the three proline residues, which are approximately in the center of helices B, C and F. Helix G is slightly bent near Lys-216. The other helices are generally straighter.

A simplified model of the proton channel (Figure 1-2) has been proposed on the basis of the atomic model structure (Henderson et al., 1990). According to this model, the extracellular half of the channel, below the Schiff base, shows an open structure

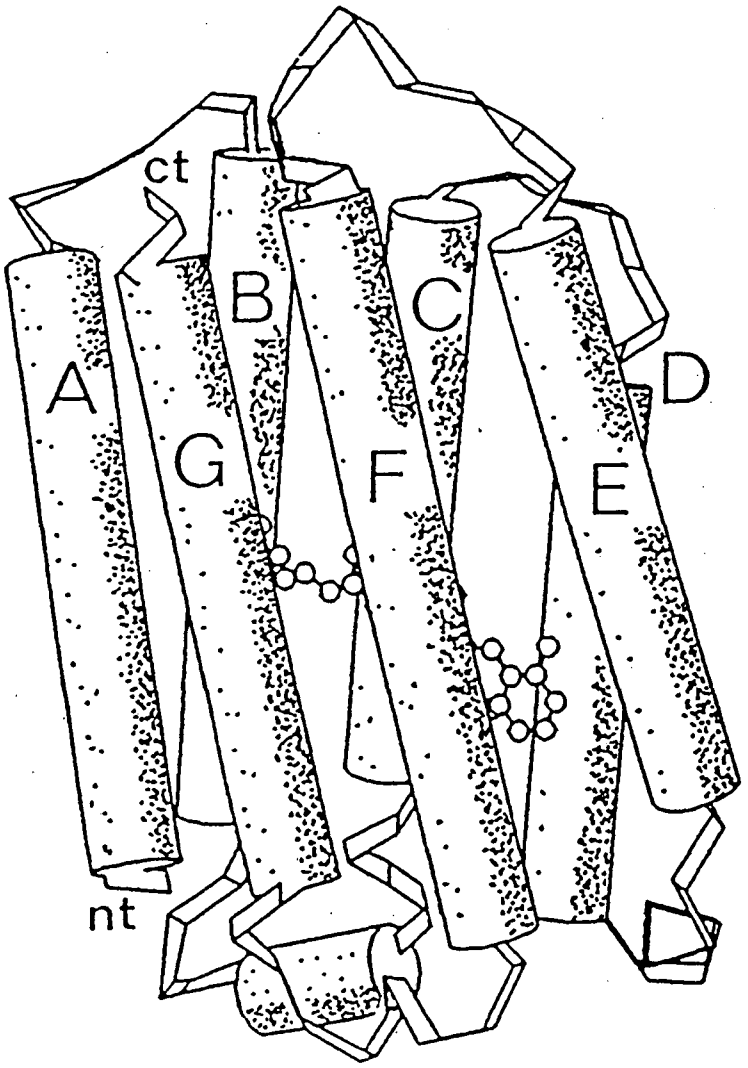

Figure 1-1. A cartoon of the protein fold of bR, based upon the atomic model structure of bacteriorhodopsin built by Henderson et al. (1990). The chromophore retinal is linked to the middle of helix G. The ionone ring is pointing toward the extracellular part of the membrane.

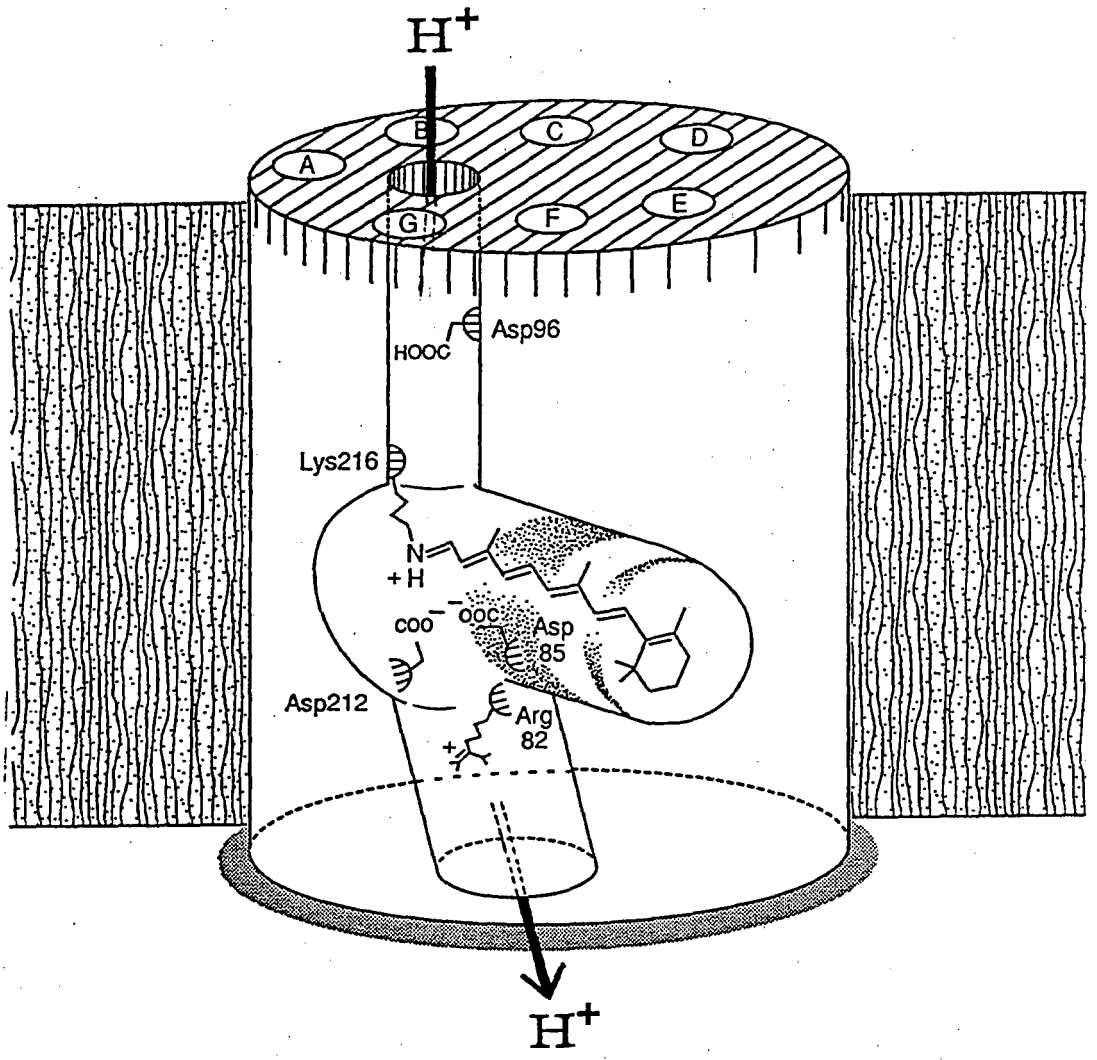

Figure 1-2. The model of the bR proton channel proposed by Henderson et al. (1990).

with sufficient room for a reasonable number of water molecules and with very hydrophilic residues, forming a hydrophilic and charge-rich channel between the Schiff base and the extracellular surface. In contrast to the extracellular half of the channel, the cytoplasmic proton uptake domain of the channel, above the Schiff base, is narrower ard hydrophobic with the single exception of aspartate 96, which acts as the internal proton donor to the Schiff base during the photocycle. The side chain of Asp-96 is positioned 10 to 12 Å above the Schiff base and 6 to 8 Å from the end of helices G and C (Henderson et al., 1990). The spatial distance of 10-12 Å between the Schiff base and Asp-96 may require some intermediate group for proton transfer, which could be Thr-89 and/or H_2O (Braiman et al., 1988; Cao et al., 1991). Recently, Arg-82 has also been proposed to act as an important component of the proton channel (Mathies et al., 1991).

1.1.3 Chromophore retinal

The chromophore retinal is covalently linked to lysine 216 in the form of a protonated Schiff base (Huang et al. 1982). The Schiff base is located roughly in the middle of the protein, and it is believed to form an important "switch" midway within a proton channel (Mathies et al., 1991). The position and orientation of the

retinal in bR_{568} has been studied by various techniques. Using deuterated retinal, neutron diffraction studies have shown that the projected position of the Schiff base is between helices C and G and that the β-ionone ring is located near helix E (Heyn et al., 1988). The polyene chain of the retinal makes a tilt angle of 20° with respect to the membrane plane (Heyn et al., 1977). The atomic model structure from Henderson et al. (1990) shows that the vertical position of the Schiff base is in the center of the protein and the ionone ring is about 5Å lower and nearer the extracellular surface, giving a tilt angle of 20° supporting previous linear dichroism measurements (Heyn et al., 1977).

The retinal binding site is well defined in the model structure of bR (Henderson et al., 1990). The retinal binding pocket is formed by 21 amino acids, including 4 tryptophans. Both Trp-86 and Trp-189 below the retinal and Trp-182 above the retinal form a sandwich structure. The side chains of Asp-85 and Asp-212 are approximately equidistant from and 4 Å below the Schiff base. Since both Asp-85 and Asp-212 are unprotonated in the ground state, they could be considered equally good candidates for the proton acceptor from the Schiff base. The more hydrophobic environment of Asp-85 relative to that of Asp-212 seems to favor Asp-85 as the proton acceptor (Henderson et al., 1990). Replacement of either Asp-212 (Needleman et al., 1991) or Asp-85 (Brown et al., 1993)

with a neutral residue causes a red-shift in the absorption maximum of the chromophore. Asp-85 is considered to be the principal proton acceptor. Replacement of D85 with a neutral residue lowers the pKa of the Schiff base from above 10 to 7 (Otto et al., 1990).

1.2 Photocycle of bR

1.2.1 Overall scheme of the photocycle

Intermediates of the photocycle can be distinguished by visible absorption spectroscopy (Fig. 1-3). The intermediates are named bR, J, K, L, M, N and O (Lozier and Niederberger, 1977; Mathies et al., 1991). The M-state intermediate is the only one in which the Schiff base is deprotonated, and as such it seems likely that structural changes between light-adapted bR and the M intermediate may be particularly important in understanding the molecular mechanism of light-driven proton pumping.

bR_{568} is the resting state of bacteriorhodopsin, and the chromophore is in the all-trans form. Asp-85 exists in the deprotonated form, and its negative charge is stabilized by the positive charge in Arg-82 (Figure 1-2). According to the C-T model (Fodor et al., 1988; Mathies et al., 1991), the bR_{568} state has a T protein conformational state, which is the lowest energy protein conformational state for the all-trans chromophore (The C state is the lowest energy conformation with a 13-cis chromophore.). When

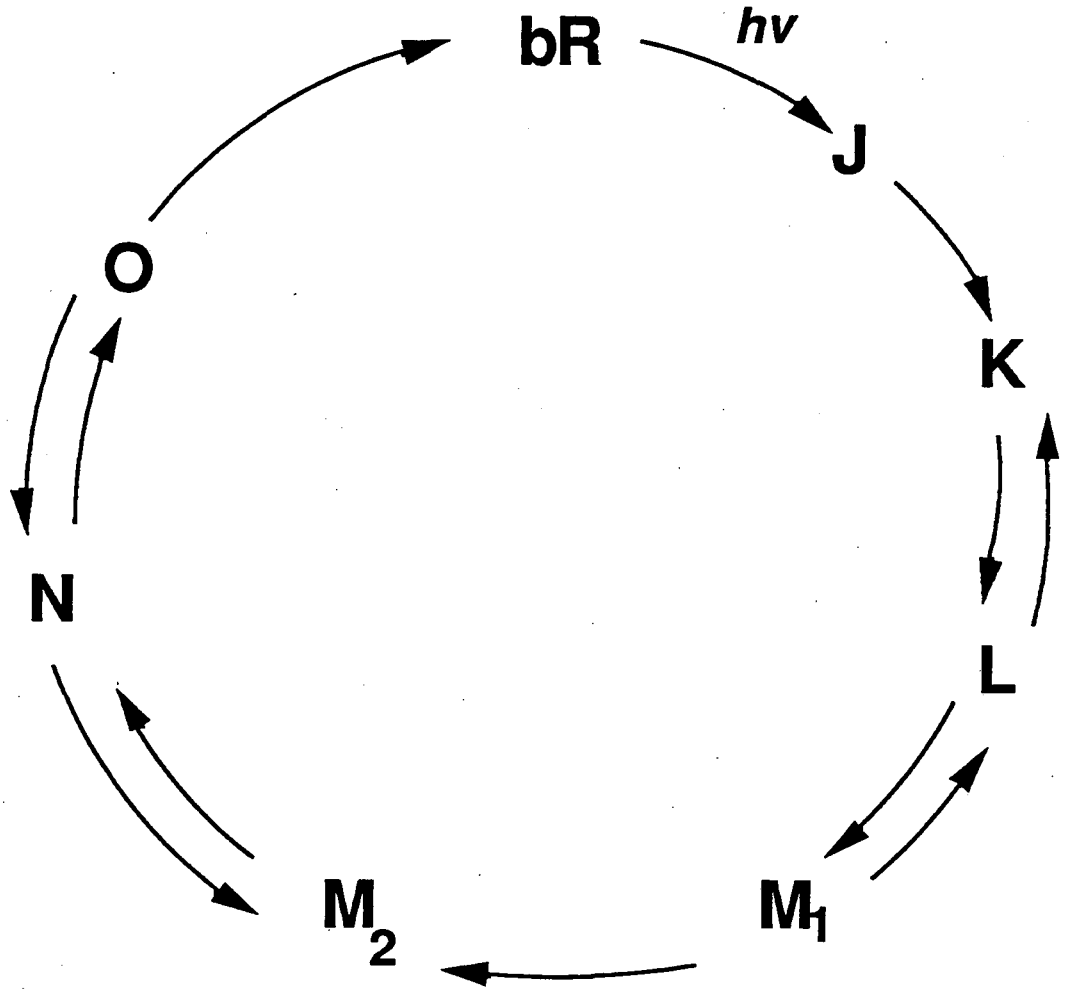

Figure 1-3. Photocycle of bacteriorhodopsin with two M substates.

bR_{568} is illuminated, a photon is absorbed by the retinal group. Part of the absorbed photon energy (~50 kcal/mol) is initially stored in the chromophore. Trans-cis isomerization occurs in the excited state, and the retinal remains in the 13-cis conformation when the excited electron returns to the ground state.

The trans → 13 cis isomerization of the retinal produces the K_{590} intermediate. The resulting cis-retinal ligand does not fit well within the T state protein conformation, and puts stress on the protein. The HOOP bands in the Resonance Raman spectrum (Braiman and Mathies, 1982) show, in fact, that the chromophore of the K state is distorted, implying that the T state protein conformation does not leave enough space for the retinal to relax to its proper, planar conformation.

In the $K_{590} \rightarrow L_{550}$ transition, the protein relaxes to a conformation that fits better for a 13-cis retinal, relieving stress between the protein and the ligand.

During the $L_{550} \rightarrow M_{412}$ transition, a proton is transferred from the Schiff base to Asp-85. The Schiff base exists in the deprotonated form only in this M state. The Schiff base deprotonation is accompanied by further changes in protein conformation, as

evidenced by the change in peak heights in the amide band regions (Perkins et al., 1992).

The 13-cis Schiff base is reprotonated in the $M_{412} \rightarrow N_{550}$ transition. Asp-96 has been regarded as an internal proton donor to the Schiff base. The deprotonation of Asp-96 appears to follow the decay of M. Dramatic elongation of the M decay time in the Asp-96 → Asn mutant supports the role of Asp-96 as the internal proton donor to the Schiff base (Otto et al., 1989).

Thermal relaxation then induces the $N_{550} \rightarrow O_{640}$ transition, presumably recovering much of the protein conformational change that occurred with M formation. This protein change then forces the 13-cis retinal back to the all-trans retinal. The deprotonated Asp-96 is likely to be reprotonated in this step (Mathies et al., 1991).

In the $O_{640} \rightarrow bR_{568}$ transition, the protonated Asp-85 is once again deprotonated, and the whole photocycle is completed.

1.2.2. Two M substates

Recently, the existence of two (or even three) M substates has been detected. In a study of the kinetics of appearance and

disappearance of various intermediates during the photocycle, Varo and Lanyi (1991a) showed that the data is best fitted by assuming two M substates linked by an irreversible step. Thermodynamic aspects indicate that vectorial transport of protons should be ensured by at least one irreversible step. By using Fourier Transform Infra Red (FTIR) spectroscopy, Ormos (1991) initially proposed that there exist two M substates, which can be trapped at 240K and 260K, respectively. The difference FTIR data, which have been confirmed by Perkins et al. (1992) for humidified, glucose-embedded specimens, establish that there are distinctly different peptide backbone conformational changes upon the formation of these two M intermediates. However, additional experiments by Ormos et al. (1992) have clearly attributed the differences in FTIR spectra, just described above, to differences in the amount of contaminating species, notably the N-intermediate, that can be formed in fully hydrated samples. This later work by Ormos et al. (1992) temporarily created an inexplicable conflict with the confirming studies of Perkins et al. (1992), which had shown that there are no contaminating species in glucose-embedded samples.

A resolution of this paradox was made clear by the recent FTIR study by Sasaki et al. (1992), which has shown that two different M substates can be trapped in the D96N mutant at high pH. One of these substates has the protein structure of N but an

unprotonated Schiff base and is therefore designated as the M_N substate. A natural explanation, then, is that the M_N-intermediate is trapped as a "contaminant" in glucose-embedded samples at 260K, just as the N-intermediate is trapped as a contaminant in fully hydrated samples. This explanation is supported by the observation that aspartate 96 remains fully protonated in glucose-embedded samples (Perkins et al., 1992; Vonck et al., 1994). Evidently, D96 cannot deprotonate at 260K in the glucose-embedded protein, and the photocycle stops at the M_N substate just as it does for the D96N mutant (which also cannot deprotonate, of course.)

To check for the presence of contaminating, non-M intermediates produced in my sample preparation method, Vonck et al. (1994) used the M-photoreversal method that was introduced by Ormos et al. (1992), but with glucose-embedded samples. After cooling the sample, bR background scans were taken; then the M-intermediate was produced by illuminating the sample and FTIR scans were repeated; finally, the M-intermediates were removed from the sample by illuminating with blue light and the FTIR spectra were recorded a third time. Control scans of the green-illuminated sample were taken after a waiting period equal to the length of time required for the blue illumination, to eliminate effects of decay. After green illumination, a spectrum similar to those published earlier (Ormos, 1991; Perkins et al., 1992) was

obtained (Fig. 1-4). Unlike the case of fully hydrated samples, blue light drives the glucose-embedded sample completely back to the bR state: the difference between the spectra taken before illumination and after green and blue illumination consists of noise only. This shows that my preparation method, unlike Ormos's, produces a negligible amount of non-M intermediates. Even so, the sample prepared at 260K must be contaminated by a fraction of protein that has an N-state conformation (i.e. by an M_N-like state), because the FTIR spectra of my glucose-embedded sample at 260K is very similar to the FTIR spectra of Ormos (1991) at 260K.

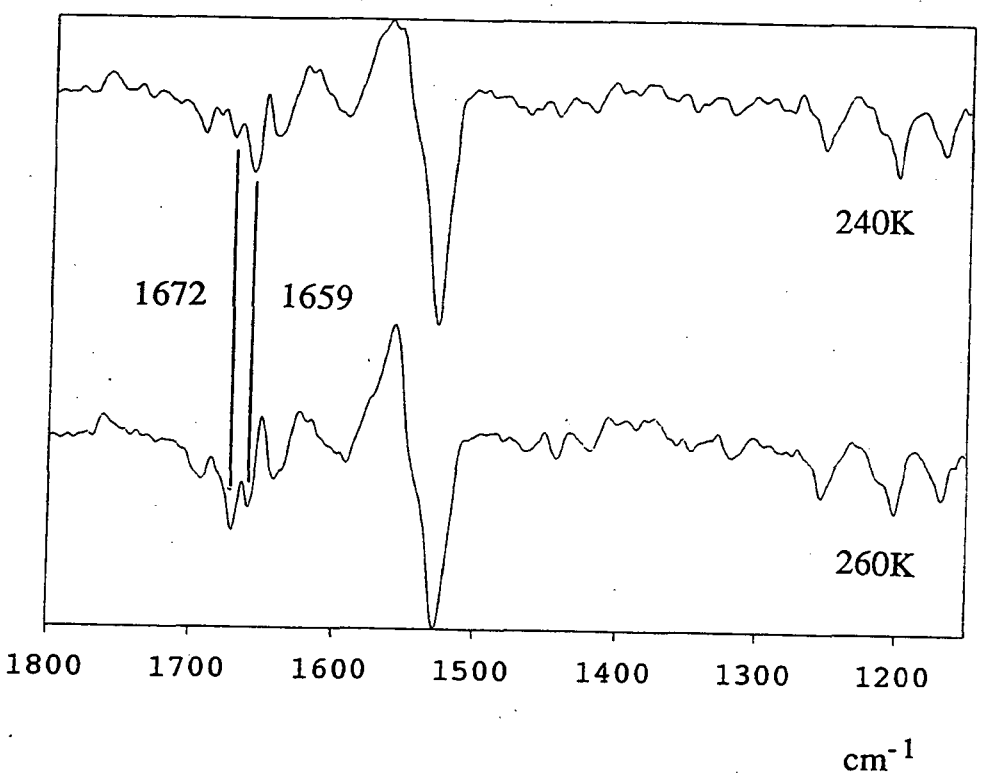

Figure 1-4. M-bR difference FTIR spectra at 240K and 260K from the blue light photo reversal experiment using humidified, glucose-embedded bR samples. Data were obtained by Dr. Janet Vonck.

1.3 Previous diffraction studies of the M intermediate

An initial electron diffraction study (Glaeser et al., 1986) indicated that there was only a very small conformational change in the formation of the M intermediate. More recent neutron (Dencher et al., 1989) and X-ray (Koch et al., 1991; Nakasako et al., 1991) diffraction studies suggest that the structural change, while small, is bigger than first estimated.

In the most recent high resolution electron diffraction studies of frozen hydrated samples, using the D96G mutant, Subramaniam et al. (1993) also show that there are significant conformational changes in the formation of the M intermediate. Although Subramaniam did not use spectroscopy to characterize the exact nature of the M intermediate trapped in this mutant protein, it is most likely that he has trapped predominantly M_N, because the reprotonation of the Schiff base is blocked by the removal of the proton donor, aspartate 96.

The discrepancy between the first electron diffraction work by Glaeser et al. and more recent diffraction studies can possibly be explained in terms of inadequate hydration of the glucose-

embedded specimen. FTIR and visible spectroscopy work by Perkins et al. (1992) shows that hydration is a critical factor in allowing formation of the M intermediate, when the sample is illuminated at low temperature. The conformational change of bR in the first electron diffraction work might have been limited because functionally critical water molecules were not present. Also, the noise level in humidified glucose-embedded samples is significantly lower than in the dry, glucose-embedded samples used by Glaeser et al. as has just recently been shown by Han et al. (1994a). The rather high noise level in the data obtained from dry, glucose-embedded samples, which is described in Chapter 4, may have been another obstacle in detecting structural changes.

1.4 Comparison with halorhodopsin, sensory rhodopsin, and rhodopsin

Three membrane proteins in *Halobacterium halobium* (bacteriorhodopsin, halorhodopsin and sensory rhodopsin), as well as rhodopsin, the dim-light vision photoreceptor in mammals, all form a group that uses retinal as the chromophore (Khorana, 1993). Each protein seems to have 7 helices spanning the membrane, as has been proved in the case of bacteriorhodopsin by electron crystallography (Henderson et al., 1990). In every rhodopsin protein, the chromophore retinal is covalently linked to the ε-amino group of a lysine in the form of a Schiff base. The light induced isomerization of the double bond in the chromophore retinal induces specific protein conformational changes related to the specific biological function of each rhodopsin molecule. Bacteriorhodopsin transports protons from the inside to the outside of the cell; halorhodopsin transports chloride ions from the outside to the inside of the cell; sensory rhodopsin is involved in the control of phototaxis; and rhodopsin acts as a visual photoreceptor.

1.4.1 Halorhodopsin

The function of halorhodopsin has been identified as being an inwardly directed chloride ion pump (Schobert and Lanyi, 1982). Recently, Bamberg et al. (1993) showed that, depending on light conditions, halorhodopsin acts either as a light-driven chloride pump or as an inwardly directed proton pump. Chloride pumping is caused by green light, and proton pumping is induced by additional blue light. This proton flow is in the opposite direction, of course, to proton transport by bacteriorhodopsin.

After photoisomerization of all trans retinal to 13 cis-retinal, halorhodopsin goes through a series of photointermediates that can be distinguished by visible absorption spectroscopy (Figure 1-5). Light activated halorhodopsin can go through the photocycle (H_{578} trans $\rightarrow$ H_{520} cis $\rightarrow$ H_{640} $\rightarrow$ H_{565} trans $\rightarrow$ H_{578} trans) which leads to inward chloride transport within 14 ms. This chloride transport is not connected with reversible deprotonation of the Schiff base.

However, halorhodopsin can produce H_{410} in a side photocycle (H_{578} trans $\rightarrow$ H_{520} cis $\rightarrow$ H_{410} cis $\rightarrow$ H_{410} trans $\rightarrow$ H_{578} trans), which leads to the inward proton transport (Bamberg et al., 1993). This proton transport is connected with reversible deprotonation of the Schiff base, as in the case of bacteriorhodopsin proton transport.

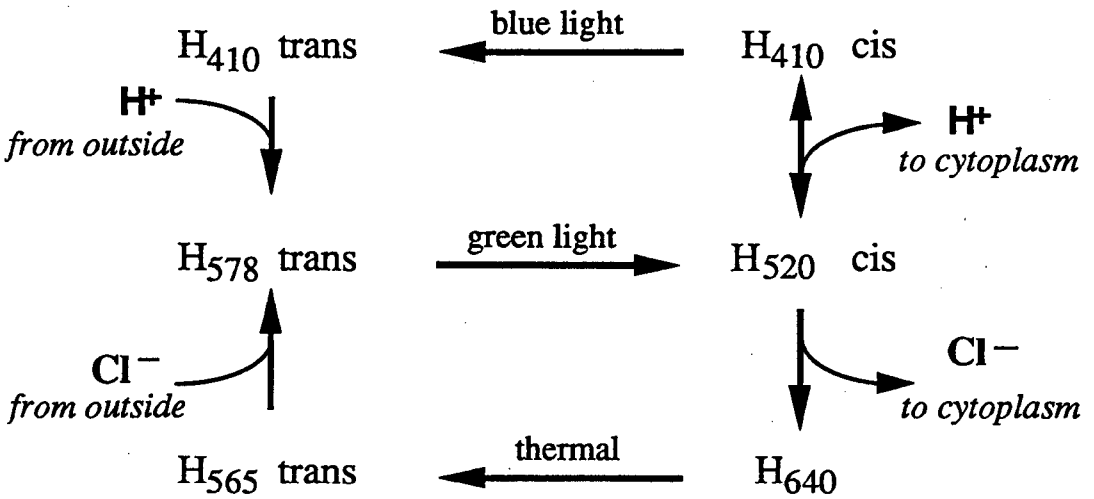

Figure 1-5. Model of the proton and Cl^- transport cycles in halorhodopsin (Bamberg et al., 1993).

The photocycle product H_{410} cis is produced from the photointermediate H_{520} cis and contains a deprotonated Schiff base in the 13-cis configuration. H_{410} cis returns in a thermal reaction to the ground state with a slow time constant in the range of seconds. In the presence of additional blue light illumination, the

chromophore retinal isomerizes from 13-cis to all trans H_{410}. This trans H_{410} state returns to the ground state much faster than the 13-cis H_{410} state, allowing blue light regulation of chloride pumping.

Another connection between hR and bR exists in terms of the effect that azide has on hR and on the D96N mutant of bR. It is known that azide can accelerate the normally slow proton transport rate of D96N mutant of bacteriorhodopsin back to the normal (or even higher) level (Tittor et al., 1989). Halorhodopsin lacks an aspartic acid residue corresponding to Asp 96 in bacteriorhodopsin, as does the D96N mutant of bacteriorhodopsin. It is interesting, therefore, that azide accelerates the accumulation of the H_{410} state by catalyzing the deprotonation reaction of the Schiff base (Hegemann et al., 1985). As a result, chloride transport is inhibited by azide in green light, but can be reactivated by blue light.

With a 32% identity of primary amino acid sequence between bacteriorhodopsin and halorhodopsin, the two proteins have been suggested to share a similar structure consisting of seven-transmembrane α–helices (Blanck and Oesterhelt, 1987; Henderson et al., 1990). In the retinal binding site, 62 % of the residues are identical in the two proteins, while in the rest of the molecule only 10 % of residues are identical (Henderson et al., 1990). Halorhodopsin lacks both aspartic acid residues corresponding to aspartate 85 and 96 in bacteriorhodopsin, which act as crucial proton donor and acceptor together with the Schiff base in

bacteriorhodopsin. These two amino acids are replaced by a threonine and an alanine, respectively, in hR (Blanck and Oesterhelt, 1987). In the narrow upper channel, the changes in halorhodopsin make the size of the protein side chains smaller by the equivalent of 5 methylene groups, suggesting that the halorhodopsin channel, designed for Cl^- ions, is larger than the bR proton channel (Henderson et al., 1990).

The amount of halorhodopsin in *Halobacterium halobium* is equivalent to only 10% of the bacteriorhodopsin content, making the purification and crystallization of the halorhodopsin more difficult than that of bacteriorhodopsin (Oesterhelt et al., 1992; Kong, 1989). A new strain D2, in which the expression level of halorhodopsin is raised to 50 to 60% of that of bacteriorhodopsin, has been established (Heymann et al., 1993). The increased level of expression of halorhodopsin in strain D2 results in the crystallization of this protein either *in vivo* or during the isolation procedure (Havelka et al., 1993). The halorhodopsin projection map obtained with these specimens is similar to that of bacteriorhodopsin, showing that the position of the seven helices of an individual halorhodopsin molecule must be very similar to that in bacteriorhodopsin. The only slight difference between two molecules appears in the region of helices D and E (Havelka et al., 1993).

1.4.2. Sensory rhodopsin

Sensory rhodopsin I (sR-I) acts as one of two signal-transducing proteins which are involved in phototaxis of *Halobacterium halobium*. Both an attractant response and a repellent response are mediated by a photocycle between the resting-state sR_{587} and a long lived photoproduct S_{373} (Spudich and Bogomolni, 1984).

On the basis of a hydropathy analysis of the primary structure, sR-I has also been proposed to have seven transmembrane helices (Blanck et al., 1989). All of the key residues involved in proton pumping by bacteriorhodopsin are present in sR-I, with the exception of aspartate 96. In the retinal binding site, 62 % of the residues are conserved between bacteriorhodopsin and sensory rhodopsin I, whereas in the rest of the molecule only 10 % of residues are conserved. In the narrow upper channel, the changes that occur in sensory rhodopsin, make the size of the protein side chains larger by the equivalent of 8 methylene groups, suggesting that the sensory rhodopsin channel must be narrower, and may be completely blocked (Henderson et al., 1990).

The retinal group and its interaction with the protein have been studied by spectroscopy. Resonance Raman spectroscopy

shows that sR-I, halorhodopsin and bacteriorhodopsin have similar chromophore configurations (Fodor et al., 1989). The FTIR spectra show that the Schiff base C=N stretch of sR-I is down-shifted 15 cm^{-1} relative to bR showing that the sR-I protonated Schiff base has a weaker electrostatic interaction with nearby counterions in the retinal binding pocket relative to bR (Fodor et al., 1989; Bousche et al., 1991). The S_{373} minus sR_{587} difference FTIR spectrum lacks a 1762 cm^{-1} peak, assigned to the protonation of the Schiff base proton acceptor, Asp-85, in bacteriorhodopsin. This fact suggests that the homologous residue in sR-I, Asp-76, does not undergo a protonation change during the $sR_{587} \rightarrow S_{373}$ photoreaction, while the Schiff base itself appears to be deprotonated (Bousche et al., 1991).

1.4.3. Rhodopsin

Rhodopsin consists of a single polypeptide chain of 348 amino acids of which only about 50% is in the membrane-embedded domain. Bovine rhodopsin has three domains (cytoplasmic, membrane, and intradiscal), while bacteriorhodopsin carries out proton transport mainly through the membrane-embedded domain. Rhodopsin in the resting state contains 11-cis retinal which is covalently linked to Lys-296 by the Schiff base, while bacteriorhodopsin in resting state contains all-trans retinal, linked to Lys-216 (Fig. 1-6). The protonated Schiff base in rhodopsin is

stabilized by the carboxylate counterion of Glu-113 (Sakmar et al., 1989). The projection structure of rhodopsin was obtained at 9 Å (Schertler et al., 1993). The projection map shows four resolved peaks, assigned to four transmembrane helices, and an elongated arc-shaped feature, assigned to the three remaining, more tilted helices. The structure of rhodopsin seems to be a bundle of seven transmembrane helices mostly perpendicular to the membrane plane, as is true of bR. However, the seven helices seem to be tilted in slightly different ways than is true of bacteriorhodopsin (Schertler et al., 1993; Baldwin et al., 1988).

Light-induced isomerization of 11-cis retinal to all-trans retinal (Fig. 1-6) in rhodopsin leads to the successive photointermediates: rhodopsin → photorhodopsin → bathorhodopsin → lumirhodopsin → metarhodopsin I → metarhodopsin II → metarhodopsin III → opsin plus all-trans retinal. Metarhodopsin II contains an unprotonated Schiff base, and it is the active species that allows binding and activation of transducin, leading to the biochemical cascade which finally closes the cGMP-dependent cation channels in the plasma membrane. Closing these channels, in turn, results in hyperpolarization of the rod cells followed by nerve excitation (Khorana, 1993).

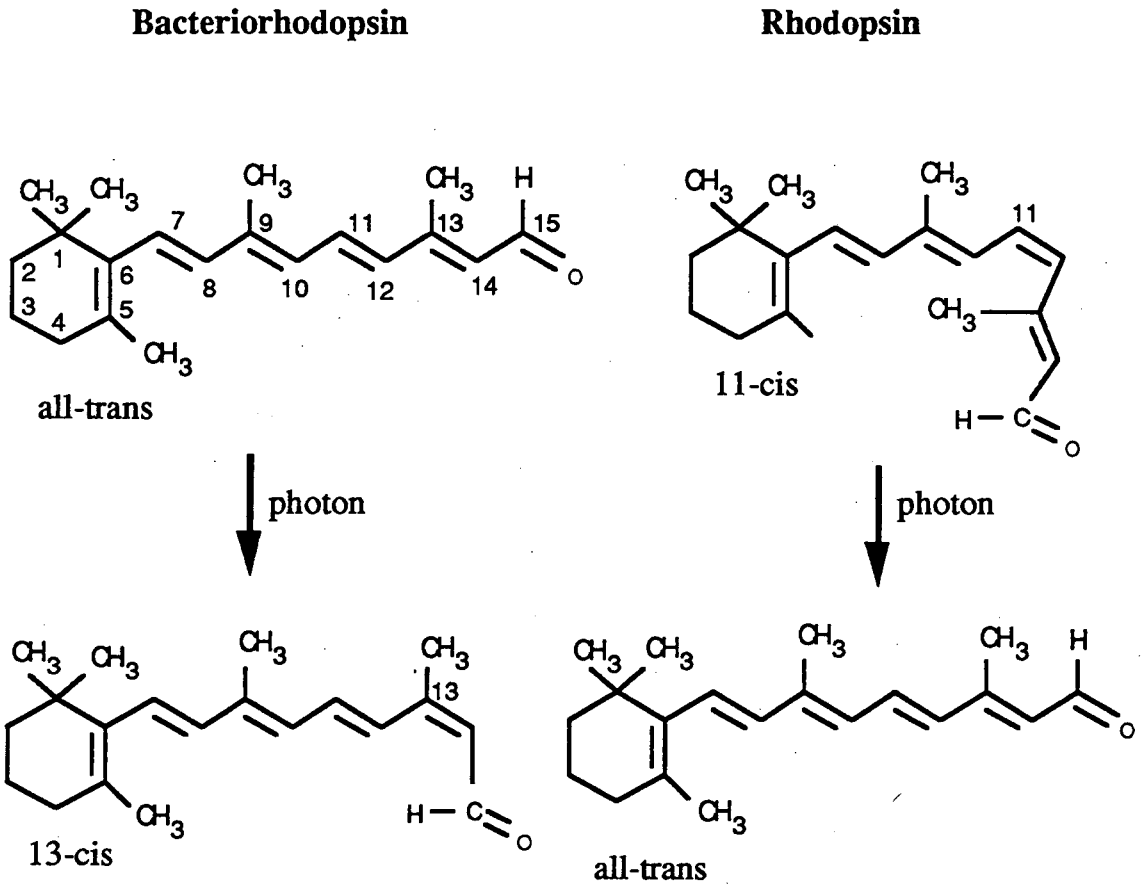

Figure 1-6. Light-induced isomerization of the retinal chromophore in bacteriorhodopsin and rhodopsin.

1.5 Main purpose of dissertation

We can learn a great deal about the molecular mechanism of proton pumping by bR, by crystallographic structure analysis of defined intermediates in the photocycle. We may also observe more general principles that serve as a paradigm for active transport in other biological systems. Since an atomic resolution model of light-adapted bR is already known, it is natural to use electron diffraction data obtained from trapped intermediates to calculate 3-D difference Fourier maps. A major goal of this work is to understand the structural basis for the proton pumping mechanism in bR at atomic resolution. In this thesis paper, high resolution structural difference maps are constructed using electron diffraction techniques.

To overcome potential problems due to partial dehydration that can occur in glucose-embedded samples (Perkins et al., 1993), a new protocol for preparing humidified, glucose-embedded bR has been used. Even when equilibrated at high humidity, these samples appear to be inhibited in the M to N step, compared to fully hydrated bR. At 240K virtually pure M is trapped, while at 260K a mixture of two, structurally distinct M substates is produced, one of

which is the M substate that is trapped at 240K while the other M is believed to be similar to the M_N substate formed by the D96N mutant (Sasaki et al., 1992; Han et al., 1994a, Vonck et al., 1994). The large difference in projection maps of M-bR at 240K and 260K, which is documented in Chapter 5, confirms that statistically significant conformational changes occur first upon formation of the M substate and then further upon formation of the M_N substate.

Chapter 2: THEORETICAL AND TECHNICAL ASPECTS OF ELECTRON CRYSTALLOGRAPHY

The recent development of electron crystallography, including electron diffraction and high resolution electron imaging, has made it possible to determine the structure of biological macromolecules at atomic resolution (DeRosier, 1993; Baldwin et al., 1988; Kühlbrandt and Downing, 1989; Henderson et al., 1990; Jap et al., 1990). The strong scattering power of electrons allows us to use very thin specimens, like biological membranes, with a thickness of only one or two molecules (Glaeser, 1992). Electron crystallography can be a powerful alternative for solving the structure in the case that large, well-ordered 3-dimensional crystals are not available for X-ray diffraction studies. Also, electrons can be focused to produce a high resolution image from which the amplitudes and phases of structure factors can be retrieved computationally, while X-ray crystallography needs multiple heavy atom derivatives for phase retrieval.

There exist several technical difficulties in electron crystallography. First, a hydrated state of the sample must be preserved in the high vacuum needed for an electron microscope. Second, biological samples can be destroyed very easily from

radiation damage, before the original structure can be observed. Third, the thickness of samples should be less than a few hundred angstroms, due to the strong scattering of electrons.

2.1. Electron scattering

The physical basis of electron scattering is different from that of X-ray scattering. Electrons are scattered by the shielded Coulomb potential of the atomic nuclei, while X-rays are scattered by the electron charge density. As a result, the density maps in electron microscopy represent the Coulomb potential while those in X-ray represent the electron density. Both functions, however, are cusp-shaped and are centered about the atomic nucleus.

Electrons interact much more strongly with matter than do X-rays. The atomic scattering intensities in electron scattering are more than 100,000 times larger than those in X-rays. Due to this strong interaction, it is possible to obtain a good, single crystal electron diffraction pattern from very small samples. Suitable crystals can be only 1 - 4 μm in diameter, and one or two molecules thick, which corresponds to about one billionth the amount of sample normally used for X-ray diffraction. This fact makes electron crystallography suitable for solving the structure of membrane

proteins, some of which have only been crystallized in 2-dimensional, monolayer crystals.

Other differences between the scattering amplitudes of electrons and X-ray include the fact that electron amplitudes decrease more rapidly with scattering angle than do X-ray amplitudes, and electron amplitudes show less discrimination between heavy and light atoms.

2.2. Sample preparation and radiation damage

The relatively high vacuum of 10^{-5} torr, needed to prevent excessive scattering of the electron beam by gas molecules inside the electron microscope column, makes it difficult to maintain a hydrated state for biological specimens. Almost all biological macromolecules which give nice electron diffraction patterns in the hydrated state will not give diffraction patterns when they are dehydrated, as has been already known from X-ray crystallography. Conventional sample preparation techniques for fixation, embedding, freeze-drying, and negative staining destroy, to varying degrees, the native structure of biological macromolecules (Glaeser, 1982).

Two major techniques have been developed to prevent dehydration of biological specimens. The first technique uses frozen hydrated samples. The thin, wet specimens are rapidly frozen, and the frozen hydrated samples are then observed at low temperature in the microscope. In the second technique, the hydrated structure of biological specimens is preserved by embedding the specimens with nonvolatile hydrophilic molecules like simple sugars (Henderson and Unwin, 1975).

Biological molecules are highly susceptible to radiation damage. When biological molecules are irradiated by the electron beam, the molecular structure is damaged due to molecular excitation, ionization, and subsequent chemical reactions (Glaeser and Taylor, 1978; Hayward and Glaeser, 1979). The rate at which radiation damage occurs can be reduced as much as 10 times by lowering the temperature in the case of large, hydrated biological macromolecules. High-resolution images can then be recorded with a total exposure around 3 electrons/Å^2, which is significantly less than the exposure that will cause complete destruction of biological specimens. Even when cryoprotection is used to get exposures as high as ~3 electrons/Å^2, the statistical fluctuation of electrons in the final image will obscure the high resolution structural features of macromolecules completely.

The only way to obtain high resolution structure under the limit of low electron dose is to combine a large number of images of identical objects and average out the statistical fluctuations. Two-dimensional monolayer crystals are particularly appropriate for this type of averaging technique, because the motif in one unit cell is repeated exactly in all other unit cells.

2.3. Three dimensional reconstruction of the structure: projection theorem, hollow cone problem and flatness problem.

The data obtained from electron diffraction patterns and images can be mathematically converted by Fourier transformation to give an object's Coulomb potential.

The data in a single diffraction pattern or in a single image corresponds to data on a single central section in Fourier space. This relationship can be expressed mathematically by the projection theorem:

$$\boldsymbol{F}_{2D}\, I(x,y) \propto F(S_x, S_y, 0)$$

where the symbol $\boldsymbol{F}_{2D}\, I(x,y)$ represents the 2-D Fourier transform operation and $F(S_x, S_y, S_z)$ represents the three-dimensional Fourier transform of the Coulomb potential of the object. The projection theorem states that the Fourier transform of a two-dimensional projection image of an object is equivalent to a section cutting through the center of the three dimensional Fourier transform.

If we have many different projections of the object in the form of electron diffraction patterns or images, each taken at a different angle, this data represents many different two-dimensional, central sections through the 3-dimensional Fourier transform of Coulomb potential. The amplitudes from the diffraction patterns are then combined with the phases from the images. By obtaining many different central sections in Fourier space, we can fill up the whole 3-dimensional Fourier transform of the object. Once the whole 3-dimensional Fourier transform $F(S_x, S_y, S_z)$ is complete, we can calculate the 3-dimensional Coulomb potential of the object by inverse Fourier transformation (Glaeser, 1982; Chiu et al., 1993; Amos et al., 1982):

$$V(\mathbf{r}) = \boldsymbol{F}^{-1}{}_{3D}[F(\mathbf{S})]$$

where $V(\mathbf{r})$ represents 3-dimensional Coulomb potential of the object in real space.

There is a special problem in actually getting the complete 3-D structure factors, $F(\mathbf{S})$, from central sections. This problem, called the "hollow cone problem" in constructing three-dimensional structure in electron microscopy, is due to the fact that projections of the structure can only be obtained over a limited range of tilt angles $\pm 60°$ (Glaeser, 1982; Glaeser et al., 1989). The limited range

of tilt angles leaves a conical section of reciprocal space inaccessible to experimental measurement. We can nevertheless construct an inverse Fourier transform with the accessible but incomplete data.

The experimentally obtained, incomplete data $F_{obs}(S)$ in reciprocal space can be expressed as the product between the complete 3-dimensional data in reciprocal space $F(S)$ and a 3-dimensional aperture function $A(S)$:

$$F_{obs}(S) = F(S) \cdot A(S)$$

The three dimensional aperture function $A(S)$ is unity everywhere within the domain of observation and is zero within the hollow cone. The final inverse Fourier transform is the convolution product of the real Coulomb potential $V(r)$ of the object and a 3-dimensional point spread function $a(r)$:

$$\boldsymbol{F}^{-1}[F_{obs}(S)] = \boldsymbol{F}^{-1}[F(S)] * \boldsymbol{F}^{-1}[A(S)] = V(r) * a(r).$$

This equation shows that the resolution in the z direction should be degraded by the 3-dimensional point spread function $a(r)$. If the range of tilt angles is $\pm 60°$, corresponding to 87% of reciprocal space, the final map is elongated by a factor of 1.3 in the direction of the missing data (Glaeser et al., 1989).

The preparation of flat specimens is a critical requirement for constructing a complete, high resolution 3-D data set. Sheet-like biological specimens can be easily wrinkled. If samples are not flat enough because of wrinkling, diffraction spots become broadened at high tilt angles to such an extent that each diffraction spot cannot be separated. For geometrical reasons, this broadening effect is much more serious at high tilt angle and high resolution (high z^* value). The wrinkling of the specimen should be less than 0.2 degree for high resolution 3-D data collection (Glaeser et al., 1991).

Techniques to reliably prepare flat specimens have not been fully established. Recent progresses in preparing flat specimens is discussed further in Chapter 6.

Chapter 3: EXPERIMENTAL METHODS

3.1 Sample preparation

3.1.1 Purification and fusion of bR

Purple membranes were isolated and purified from *Halobacterium halobium* strain ET1001, according to the protocol of Oesterhelt and Stoeckenius (1971).

The purified, native purple membrane patches were fused in a special fusion buffer according to the protocol of Baldwin and Henderson (1984), to produce membrane patches with a diameter larger than 4 μm. The final concentration of a purple membrane suspension is adjusted to be 3 mg/ml with 0.1 M potassium phosphate buffer at pH 5.2. The purple membrane suspension is mixed with octyl glucopyranoside (OG) and dodecyltrimethylammonium chloride (DTAC), which are adjusted to a final concentration of 6 mM and 200 μM, respectively. The concentration of DTAC is critical to produce large, single-thickness crystals. A high concentration of DTAC causes aggregation of purple

membranes, and a low concentration of DTAC is not enough to facilitate fusion. DTAC is extremely hydroscopic, however, causing the reagent to become sticky and making it hard to quantify the exact amount of DTAC. Some trial and error to find the optimum concentration of DTAC was required to get membrane sheets that are both large in diameter, and not stacked together in the form of double-thickness crystals. The best result was obtained by trying various concentrations of DTAC within ±7% variation from 200 μM. Membrane patches larger than 4 μm were obtained after 3 weeks.

3.1.2 Preparation of specimen grids

The specimen grids for electron microscopy were made as described by Glaeser and Downing (1990). Aged hydrophobic carbon film, evaporated on top of a mica, was cut to the size of a 300 mesh copper grid and floated onto a glucose solution in pH 6.5, 10 mM MOPS buffer. The carbon film was picked up by a copper grid and 2 μl of glucose solution was added to the liquid underneath the carbon film, supported by the copper grid. Fused membranes (2.5 μl) were added to the liquid under the carbon film and mixed with the preexisting solution. After mixing, some of the excess solution was removed with the pipette. The remaining solution was blotted with a filter paper in air which was equilibrated at 80 % relative

humidity by bubbling the air through a saturated ammonium sulfate solution. After equilibrating in the 80% humidity air stream for 10 minutes, the grid was plunged into liquid nitrogen, to prevent further drying.

3.1.3 Trapping of the M intermediate

The M intermediate was trapped in an appropriate form for electron diffraction study as follows. The grid was held in the flowing humid air for 10 minutes (Fig. 3-1 (a)). Then the grid was rapidly plunged into liquid nitrogen (Fig. 3-1 (b)). The "frozen" specimen grid was transferred into a Gatan cryo-specimen holder under liquid nitrogen (Fig. 3-1(c)). The blade shutter of the specimen holder was opened to ambient air at a specimen temperature of -110 °C for 90 seconds to condense an excess amount of ice on the specimen grid (Fig. 3-1(d)). This ice condensation step was needed to prevent dehydration of the sample in the stream of dry, cold nitrogen gas that was subsequently used for warming the sample to 240K or 260K. After the ice condensation step, the blade shutter was closed and the specimen holder was inserted into a home made chamber in which the specimen temperature was equilibrated by flowing cold nitrogen gas at either 240K or 260K, as is shown schematically in Fig. 3-1(e). The

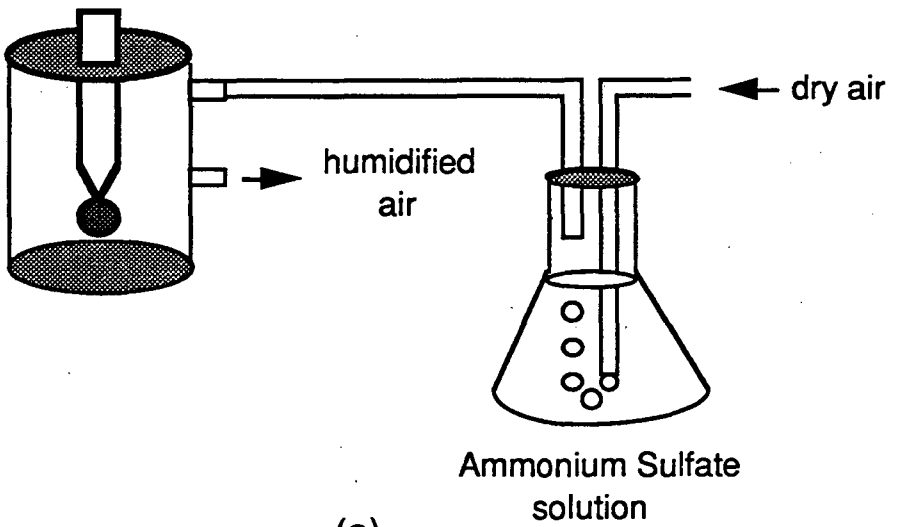
dry air
humidified
air
Ammonium Sulfate
solution

(a)

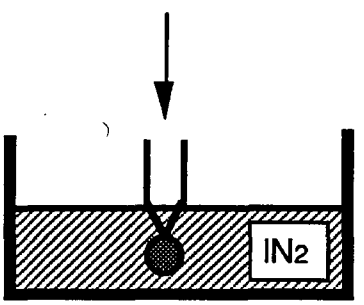
IN2

(b)

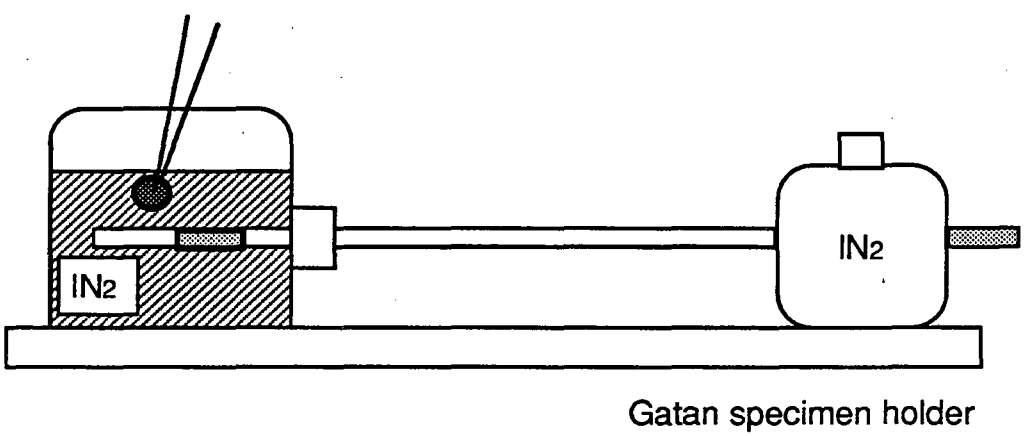
IN2
IN2
Gatan specimen holder

(c)

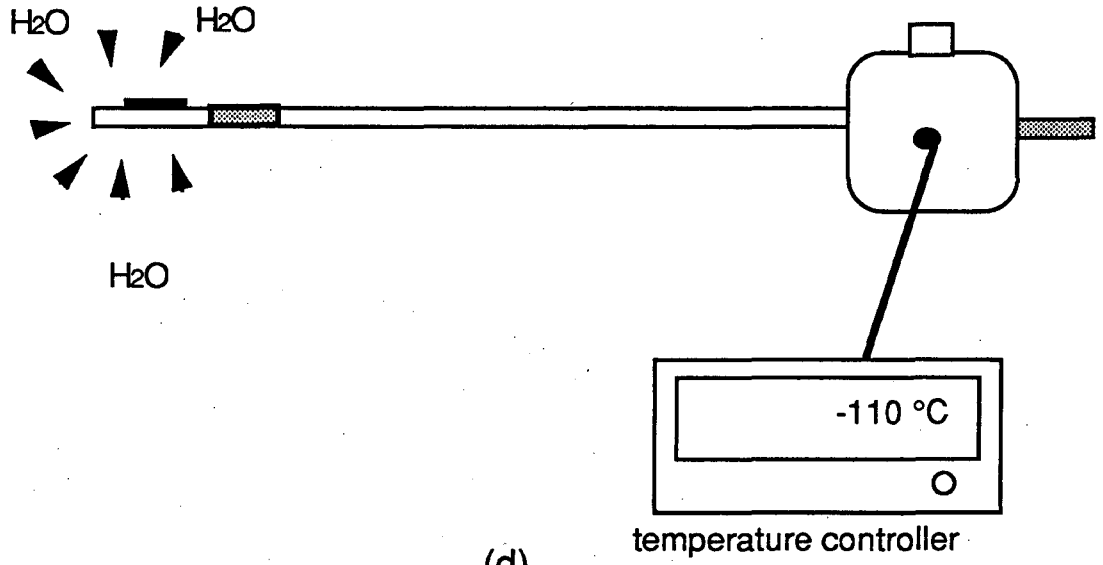
H2O
H2O
H2O
-110 °C
temperature controller

(d)

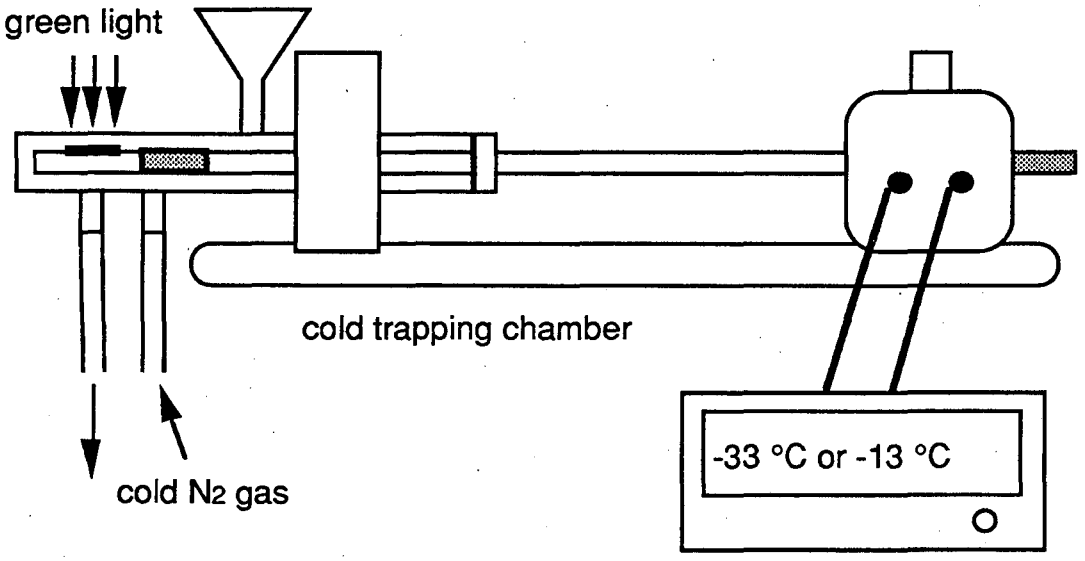
green light
cold trapping chamber
cold N2 gas
-33 °C or -13 °C

(e)

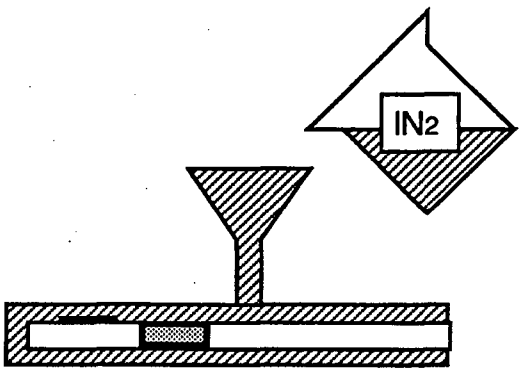

(f)

Electron Microscope

(g)

Figure 3-1. Sample preparation protocols (a) The specimen grid was incubated at 80 % relative humidity for 10 minutes in a stream of air which was humidified by bubbling the air through a saturated ammonium sulfate solution. (b) The hydrated specimen grid was plunged into liquid nitrogen. (c) The frozen grid was loaded into the Gatan specimen holder at liquid nitrogen temperature. (d) The specimen grid was exposed to ambient air to condense ice on the surface of a sample at -110 °C, in the dark. After 90 seconds, the shutter of the specimen holder was closed and the specimen holder was inserted into a home-made cold trapping chamber, pre-equilibrated at -33 °C or -13°C by a steady flow of cold nitrogen gas. (e) When the sample was equilibrated at -33 °C or -13°C, the shutter was opened and the sample was illuminated with filtered green light for 1 minute. (f) Immediately after the heater and the green light was turned off, liquid nitrogen was poured directly on top of the specimen grid to trap the M intermediate. (g) The frozen sample was inserted into the electron microscope.

temperature of this cold N_2 gas was controlled by adjusting the rate of boil-off in the supply Dewar. The automatic temperature control of the Gatan cryo-specimen holder was also set to the corresponding temperature. The temperature of the specimen holder was checked by reading both the Gatan temperature control gauge and another thermocouple attached near the specimen grid. When the temperature readouts of both the Gatan temperature control gauge and the thermocouple were stabilized at 240K or 260K, as described, the blade shutter was opened to expose the specimen grid to previously focused, filtered green light for 30 seconds. Then liquid nitrogen was poured onto the grid and the green light was turned off (Fig. 3-1(f)). After the temperature dropped below 210K, the Gatan blade shutter was closed and the Gatan cryo-specimen holder was inserted into the electron microscope (Fig. 3-1(g)). The remaining excess amount of ice was sublimed by heating the sample to 180K in the microscope vacuum for at least 15 minutes. Then the specimen grid was cooled again to 110K in preparation for the diffraction data collection.

Two different sets of diffraction data were collected for the sample in the bR568 state, to avoid any systematic error which could be caused by the two different maximum temperatures that are used as part of the sample preparation techniques for M_{240K} and M_{260K}. The bR568 data set needed for each substate was collected

from samples that were prepared using the same protocol that was used to trap each M substate, but omitting the illumination by green light. These "reference" data sets are named bR_{240K} and bR_{260K}, corresponding to M_{240K} and M_{260K} respectively.

3.2 Electron diffraction data collection and processing

3.2.1 Collection of diffraction patterns

Electron diffraction data were recorded on Kodak SO-163 film, using a JEOL JEM 4000 EX electron microscope at an accelerating voltage of 400 kV. Specimens were examined under low dose conditions (about 1 electron/Å^2/minute) in a defocused diffraction mode, called the "search" mode, to provide a high contrast, low resolution image. When a good crystal was found, the crystal was moved into the optical center of the electron microscope. The shutter was then closed and the electron microscope was switched to the "diffraction" mode, in which the beam diameter had been adjusted in advance to 3 μm at the specimen plane, and the beam current had been adjusted so that the diffraction pattern could be observed for 30-50 sec before complete fading. The final accumulated electron dose, for an exposure time of about 40 seconds, was 3 electrons/Å^2 on the specimen plane. Diffraction patterns were first examined by checking brief (1 sec) exposures captured on a frame grabber, displayed on the Gatan TV monitor.

Only diffraction patterns which diffracted better than 15 order and showed no sign of twinning were used for further processing.

3.2.2 Densitometry

Electron diffraction patterns were digitized using a Perkin Elmer PDS densitometer. A 10 μm square aperture was used to digitize the film in 10 μm steps over an area of 2240 X 2240 steps. The acceleration and deceleration of the densitometer stage introduced wave patterns at the edge of the scanned image, especially when a high scan-speed was used. A slow scan-speed was therefore used to minimize these wave patterns, and as a result the whole scanning process took 4 hrs per film. The space between the films and the supporting glass on the densitometer stage, was partially evacuated by air pump, to make the films flat. Sometimes Newton rings appeared in the digitized images due to light interference; this effect could be removed by decreasing the pumping rate. The scanned arrays were averaged down by a factor of four after conversion of the measurements to optical densities, in order to produce 560 X 560 arrays, which saves processing time and computer memory.

3.2.3 Background subtraction and spot integration

Background subtracted spot intensities were measured, and specimen tilt angles, tilt axes, temperature factors, scale factors and twin proportions were refined using programs developed by Baldwin and Henderson (1984). Only those diffraction patterns were used which extended to at least 3.5 Å resolution, and which had minor twin proportions less than 10 %. Unavoidable, small fluctuation in tilt angles, within ±5°, resulted in a slight distribution of measured intensities along each reciprocal lattice line. Curves were fitted to the measured intensities for each reciprocal lattice line, and intensities at the (h,k,0) plane were interpolated from the fitted curves. The final diffraction data were confined to 3.8 Å and 3.5 Å for the projection map and three-dimensional map, respectively. The final amplitude data in the (h,k,0) plane were combined with the published phase data (Henderson et al., 1990) to produce difference Fourier projection maps. Contour levels for the difference Fourier projection maps were chosen so that one contour level corresponds to one tenth of the contour level used for the projection map of bR in Fig. 3-2.

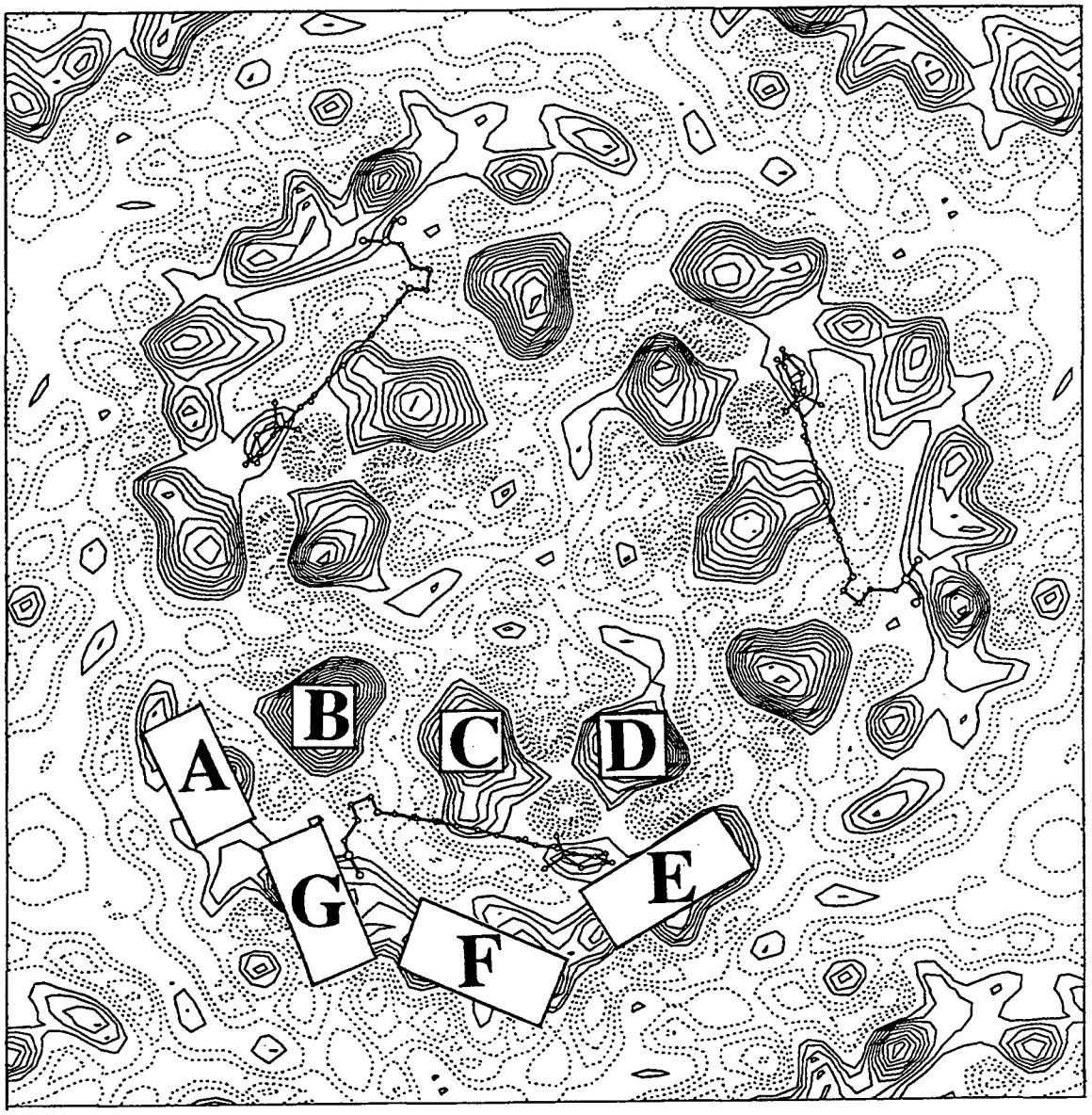

Figure 3-2. Projection map of bR from the data of Henderson et al. (1990). The positions of lysine 216 and retinal are superimposed on the map.

Chapter 4: HYDRATION EFFECT

Sufficient hydration of glucose-embedded PM is essential for formation of the M-intermediate at low temperatures (Perkins et al., 1992; Perkins et al. 1993). A new technique had to be developed, therefore, to prepare hydrated samples in an appropriate form for electron diffraction study, as described in Chapter 3, Experimental Methods.

4.1 Ice condensation

A heavy amount of ice, which was condensed on top of the specimen surface to prevent dehydration of samples, could block the electron beam completely. Excess ice should be sublimed by heating up the sample to -90 °C for 10 minutes before data collection. Both the sublimed ice from the top of the specimen grid and evaporated water from the emulsion of wet photographic films can once again condense on top of the specimen grid, when it is cooled again to liquid nitrogen temperature. Condensed small ice crystals increased background scattering seriously and caused sharp ring diffraction patterns to appear especially at 3.6 Å resolution.

The ice crystals caused a more serious effect for that resolution zone in our new sample preparation technique, which uses the intentional ice-condensation step, rather than the conventional technique which uses relatively dry specimens. The ring diffraction patterns could be removed, however, by heating the specimens to -90 °C every hour.

Fig. 4-1 shows an electron diffraction pattern from conventionally prepared, glucose-embedded purple membranes. Fig. 4-2 and Fig. 4-3 show electron diffraction patterns from humidified, glucose-embedded purple membranes. Fig. 4-2 shows a ring diffraction pattern at 3.6 Å due to the condensed ice crystals. In Fig. 4-3, the ring diffraction pattern was completely removed by occasional heating of the specimen to -90°C.

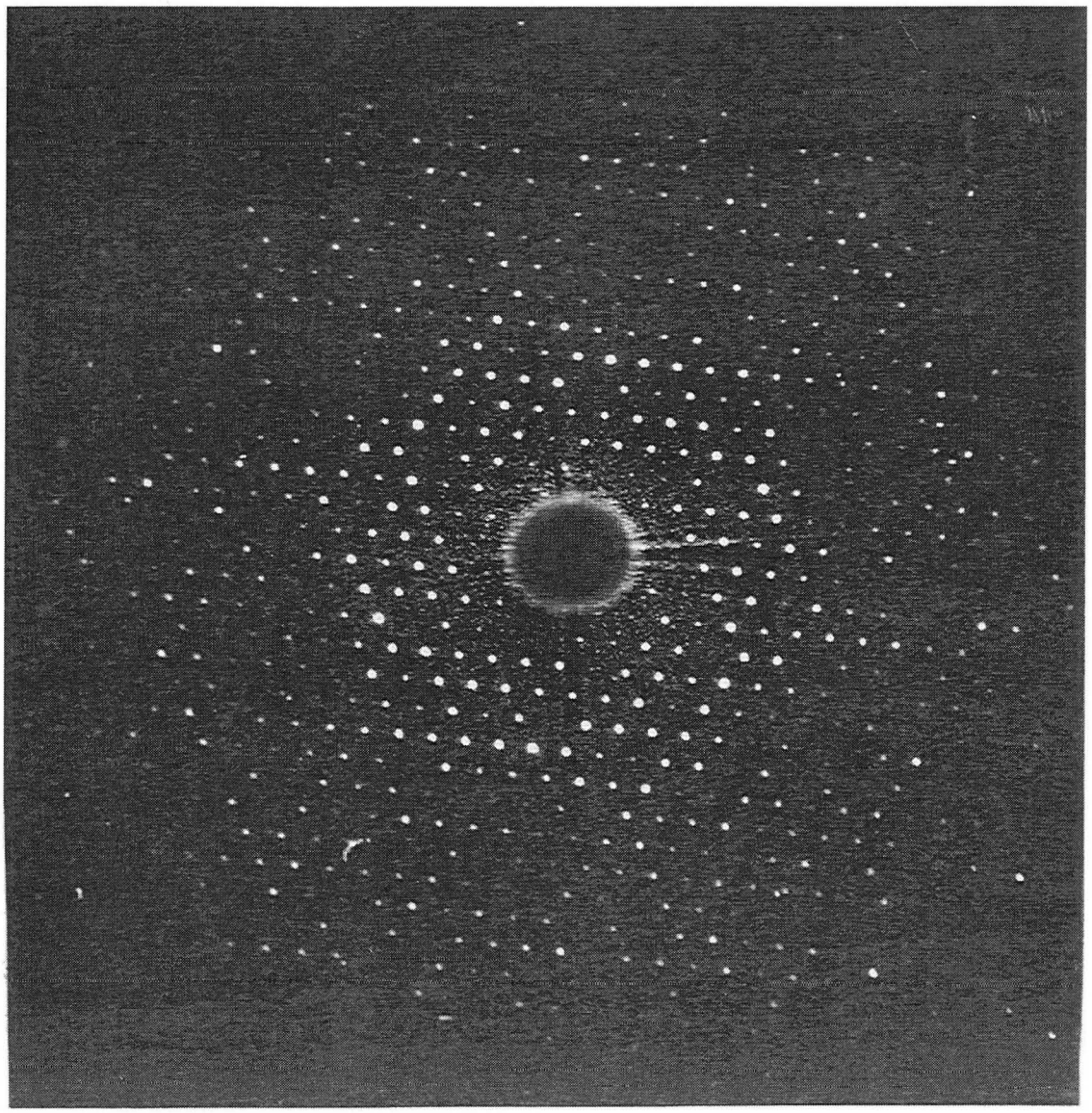

Figure 4-1. A diffraction pattern from conventional glucose-embedded bR.

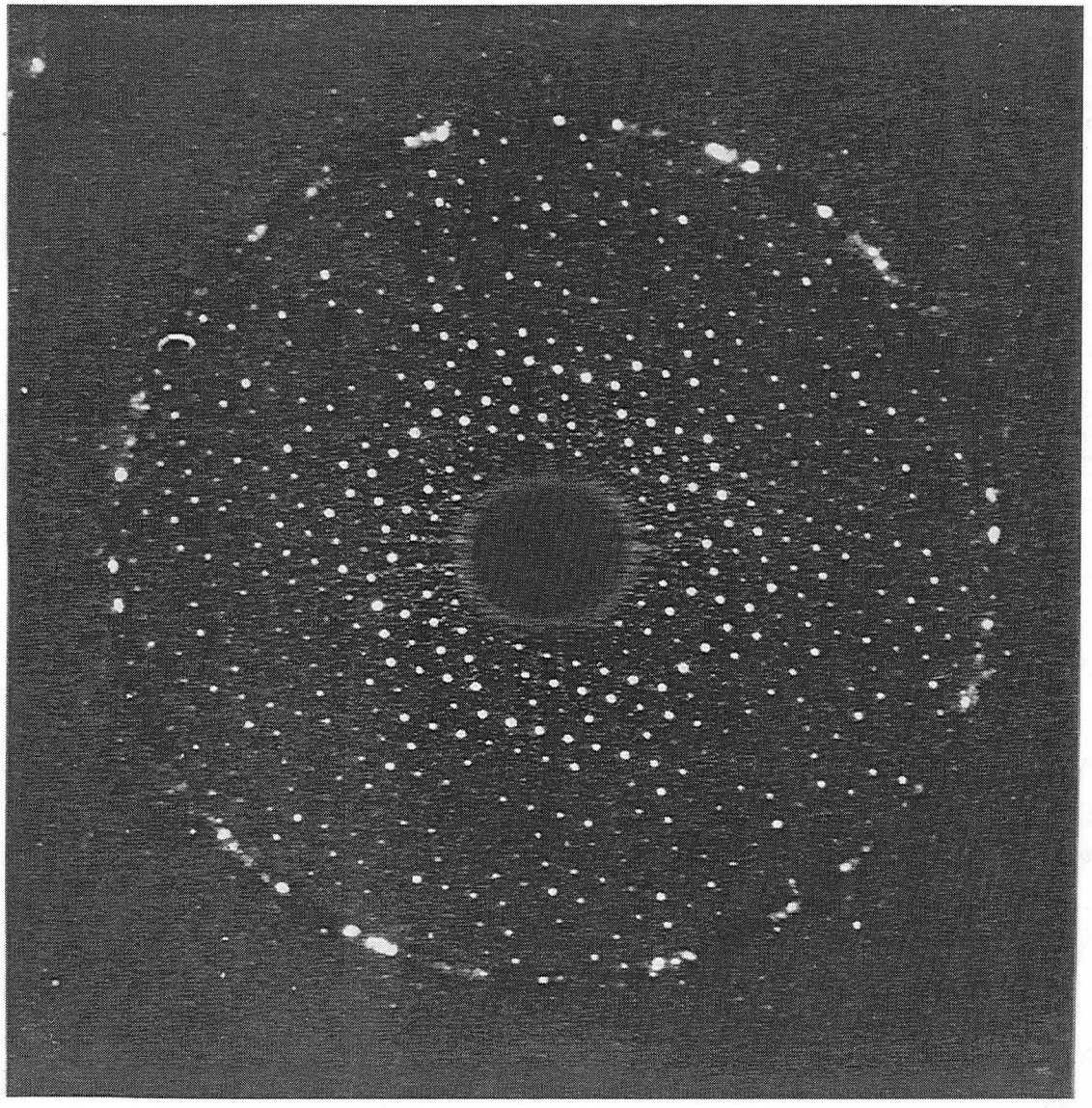

Figure 4-2. A diffraction pattern from humidified, glucose-embedded bR. Ring diffraction patterns, due to ice crystals, appear at about 3.6 Å resolution.

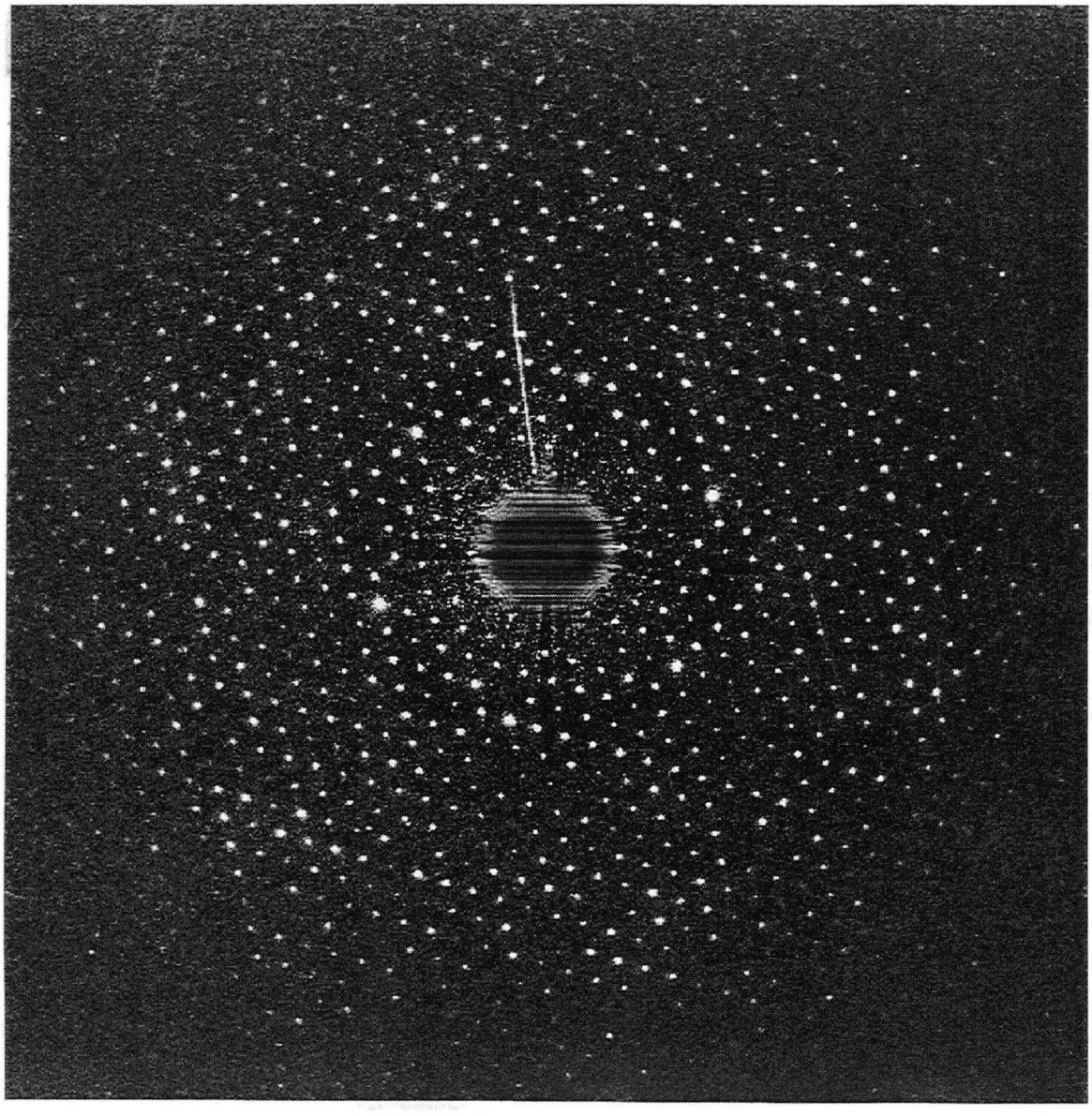

Figure 4-3. A diffraction pattern from humidified, glucose-embedded bR. Diffraction patterns extend up to 2.6 Å in the film. Ring diffraction patterns, due to ice crystals, have been avoided by heating the sample to 90 °C for 10 minutes. (Ted Pella 62-106 carbon and Ted Pella mica were used to prepare this carbon support film.)

4.2 Difference maps

In order to determine whether our hydration protocol itself would result in structural changes, a difference Fourier map was computed between PM equilibrated in 80% relative humidity and plunge-frozen, and PM prepared in the conventional way. Hydrated samples were prepared for this preliminary work as described in Chapter 3, Experimental Methods, but omitting the heating step. Dehydrated samples were kept at ambient humidity for 30 minutes, inserted in the microscope and kept in the microscope vacuum for 30 minutes before cooling. Diffraction patterns were recorded at -160 °C and processed by Dr. Janet Vonck in both cases.

A total of 12 films each were used to evaluate the differences between the hydrated and the dehydrated samples. Difference maps based on these data are shown in Fig. 4-4 to 4-7. To test the reproducibility of these features, two independent difference maps were calculated from separate halves of the data, i.e. 6 films for each set. These maps show essentially the same features, but with different variations in peak heights (4-7). The correlation coefficient for these two, independent data sets is 0.69, showing

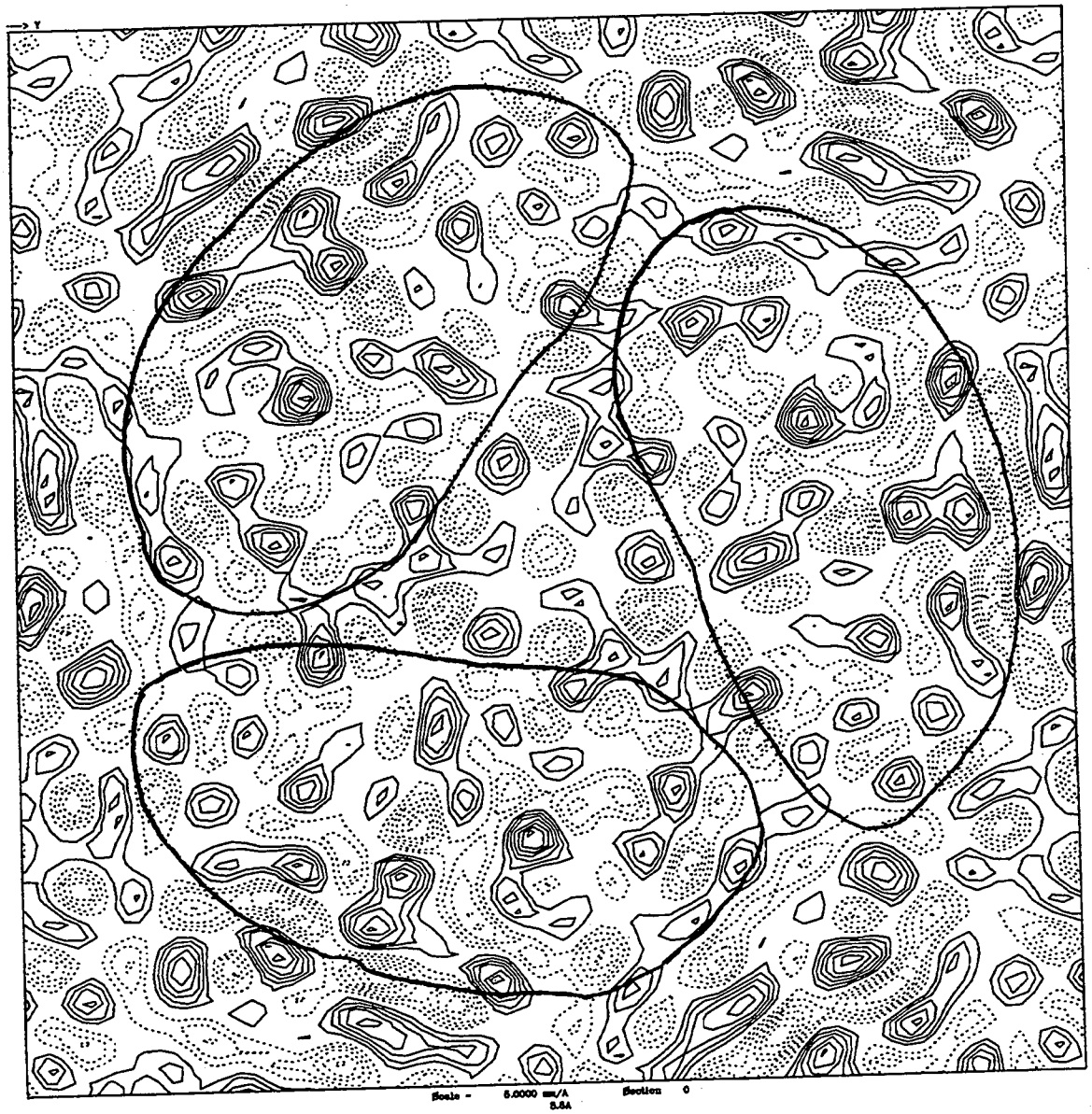
Scale - 5.0000 nm/A
5.8A
Section 0

Figure 4-4. Difference maps of glucose embedded bR to show the effect of hydration. Continuous lines represent positive signals and discontinuous lines represent negative signals. Contour levels are 1/10 of those in Figure 5. The approximate protein boundary within the plane of the membrane is drawn. This is a difference map for data from 12 films of bR equilibrated in 80 % relative humidity, minus 12 films of dry bR.

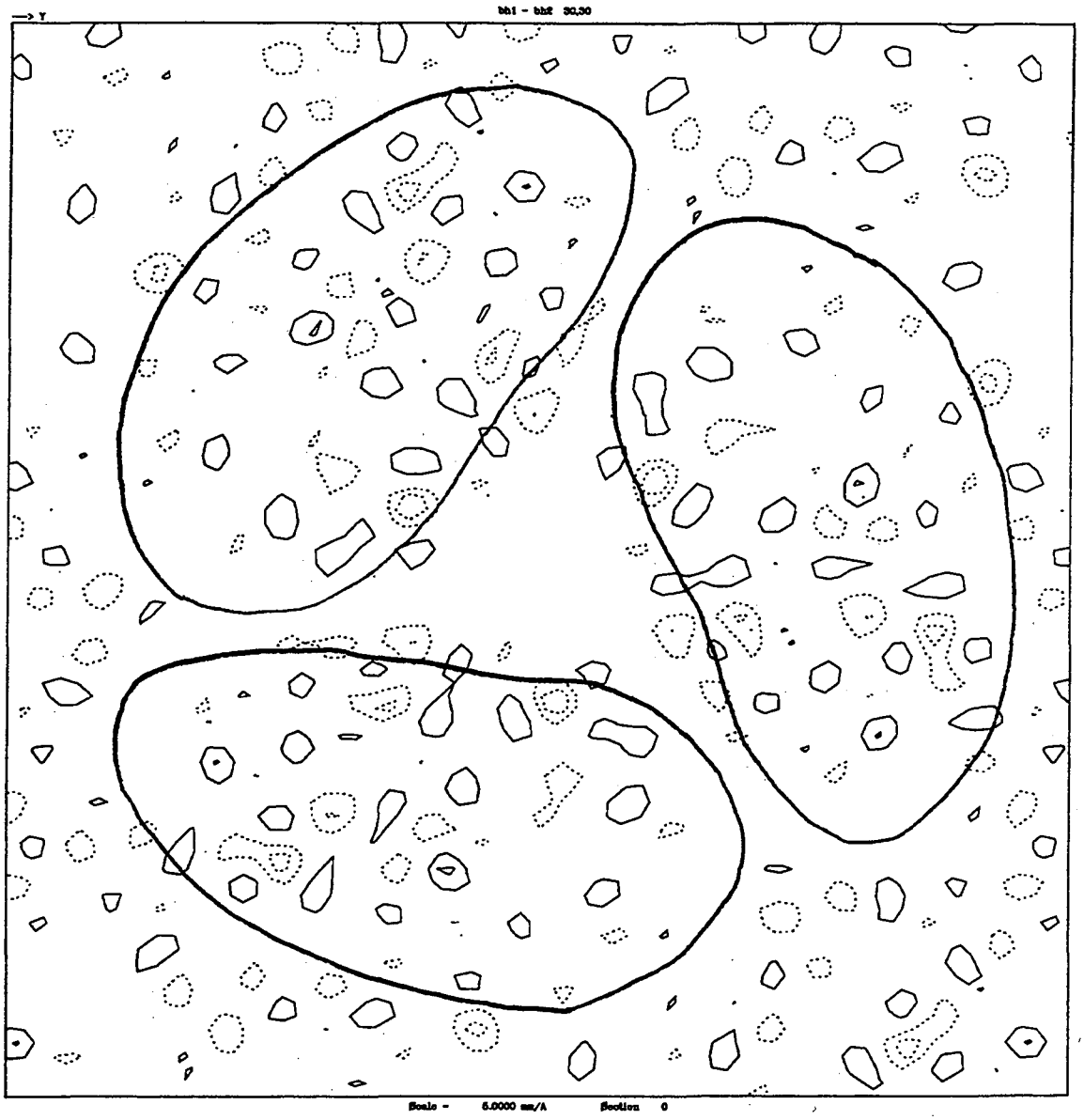

Figure 4-5. Difference map which shows the noise level in the data for humidified, glucose embedded bR. The 12 films in the "humidified specimen" data set were divided into two independent halves and processed as described in Methods, to give independent estimates of the (h,k,0) intensities.

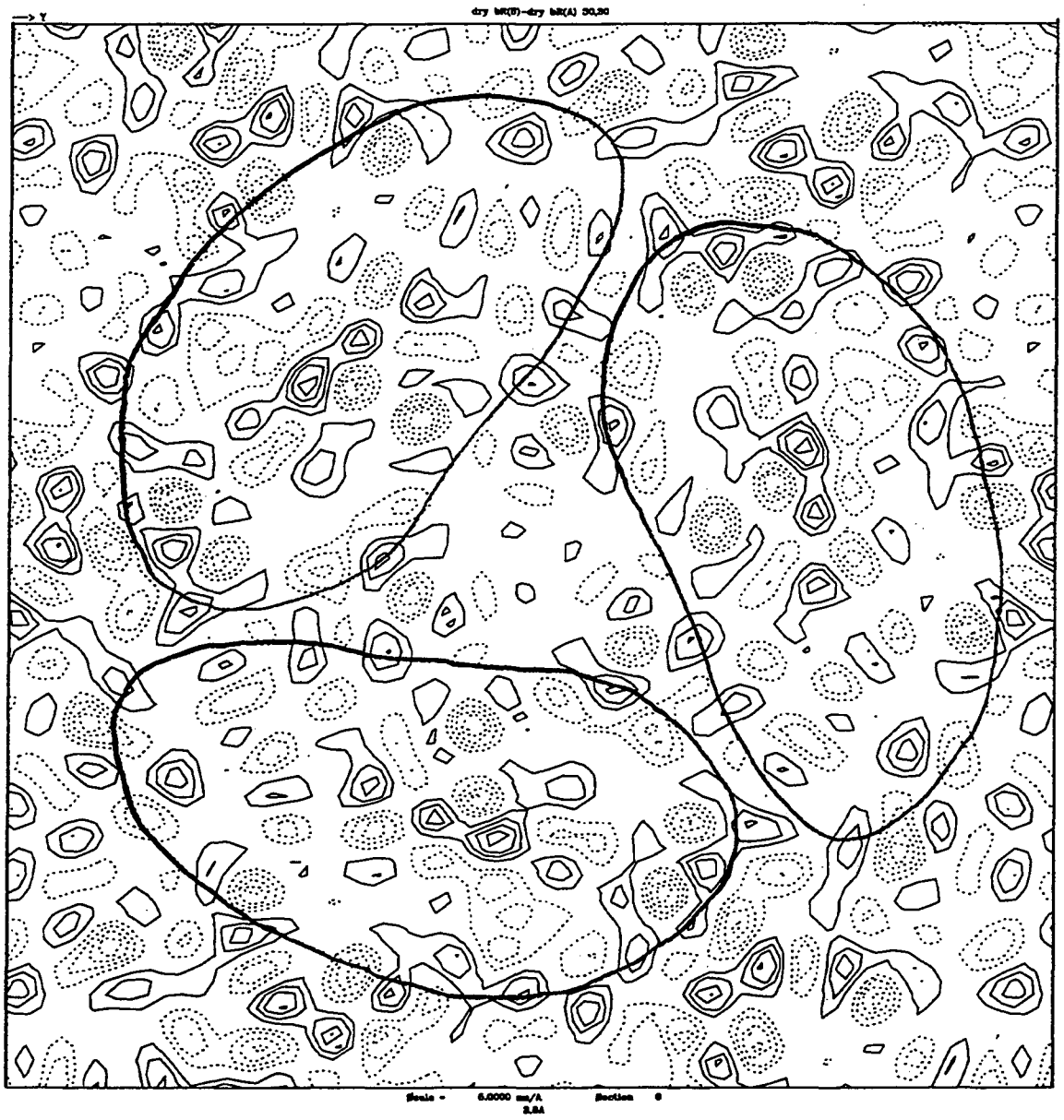

Figure 4-6. Difference map which shows the noise level in the data for dry bR.

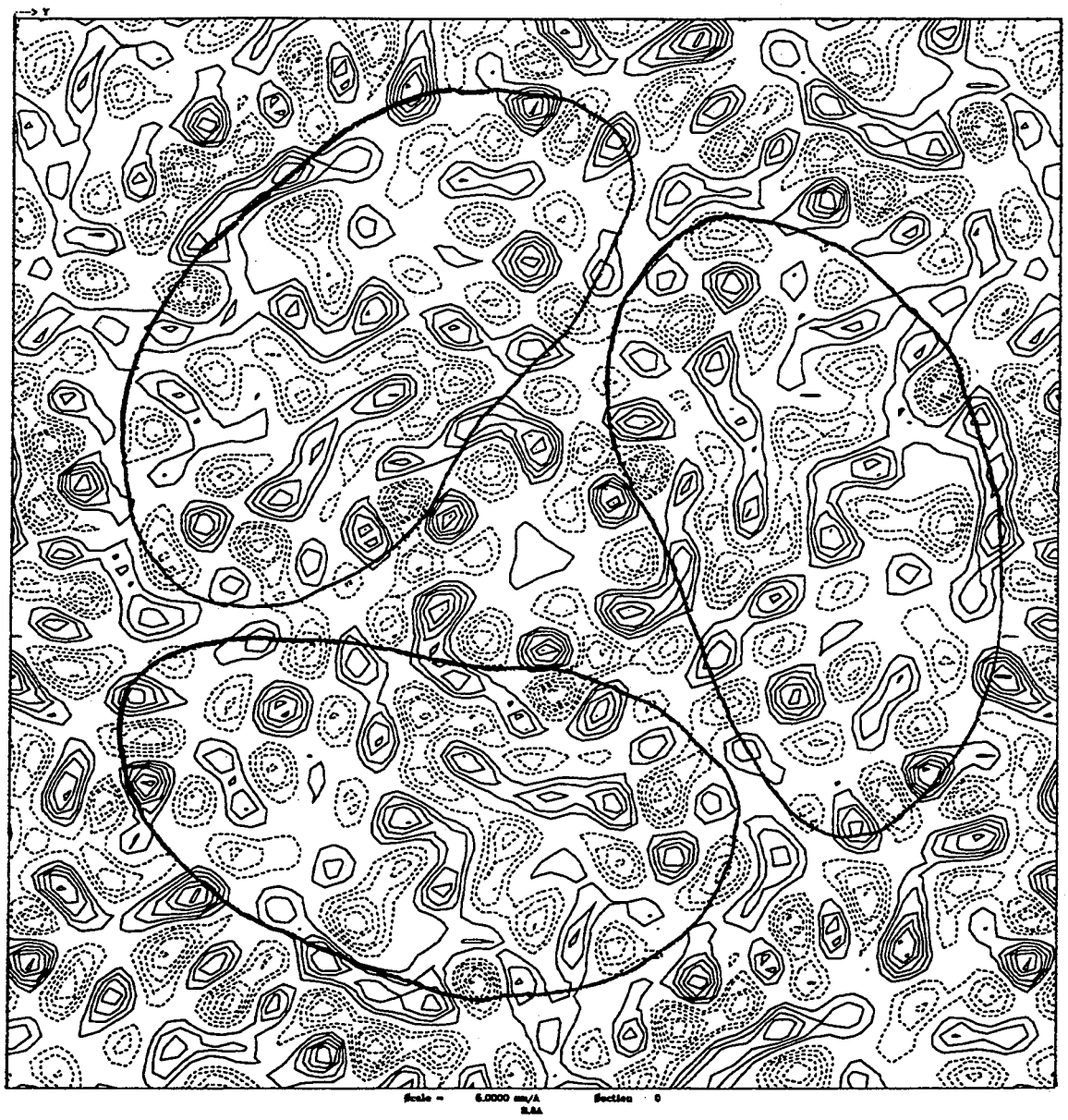

(a)

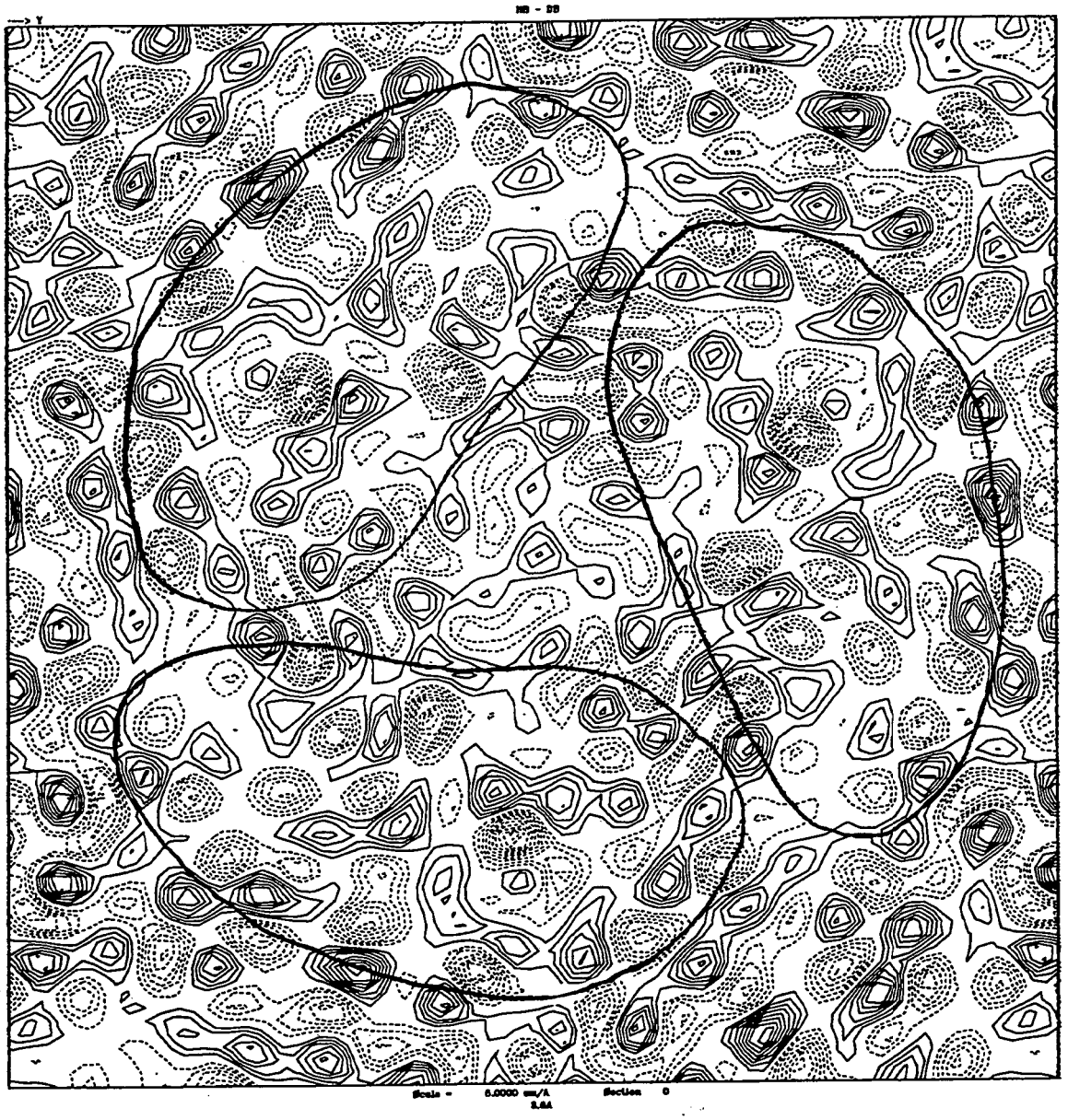

(b)

Figure 4-7. Two hydrated bR minus dry bR difference maps to show the reproducibility of hydration effect. 12 diffraction patterns from dry bR and 12 diffraction patterns from hydrated bR, are divided into independent, two halves. Two independent difference maps are made from totally independent data sets in Figure 4-7 (a) and (b).

that there is a significant difference in structure between the hydrated samples and the dry samples.

The internal consistency of the hydrated data sets and the dehydrated data sets, respectively, of Vonck was tested by dividing each set into two sets of 6 films and calculating the difference Fourier map between the halves. Features seen in these maps must result from random noise. An interesting outcome of this test is the finding that the noise level in the hydrated set (Fig. 4-5) is much lower than in the dehydrated data (Fig. 4-6). Evidently the new preparation method, which maintains improved hydration, not only keeps the protein in a state that permits the photocycle to proceed to the M-state at low temperature (Perkins et al., 1992), but also ensures a more reproducible initial structure than is the case when using dry, glucose embedded PM.

4-3. Summary

The difference Fourier map between humidified and dehydrated samples (Fig. 4-4) shows that there are significant differences in structure between samples prepared by the usual type of "glucose embedding" technique and our new "hydration technique", which was developed to guarantee the normal formation of the M intermediate at low temperature (Perkins et al., 1993). The hydration technique ensures more reproducible structures of bR than does the conventional glucose embedding technique, as indicated by the much lower noise level in the hydrated data set (Fig. 4-5) than in the dehydrated data set (Fig. 4-6).

Chapter 5: DIFFERENCE PROJECTION MAPS OF TWO SUBSTATES OF THE M INTERMEDIATE

5.1 Difference Fourier maps

The complete set of difference amplitudes in the (hk0) plane, along with the amplitudes for the M_{240K} and M_{260K} intermediates are shown in Table 1. A total of 12, 14, 14, and 12 films were used to construct the table for M_{240K}, bR_{240K}, M_{260K}, and bR_{260K}, respectively.

The difference maps and controls for the M-intermediates are shown in Fig 5-1 to 5-6. All contour levels used in these displays are 1/10 of the contour intervals used in the display of the bR map itself, Figure 3-2.

Fig. 5-1 represents the difference map between the M_{240K} substate and the bR_{240K} reference data set. This map shows that small conformational changes occur throughout the molecular envelope of the protein monomer, and even within the area of the lipid, upon formation of the M_{240K} intermediate. Major positive

Table 1 Structure factor amplitudes and difference amplitudes

H	K	F_{M240K}	ΔF_{M240K}	F_{M260K}	ΔF_{M260K}	H	K	F_{M240K}	ΔF_{M240K}	F_{M260K}	ΔF_{M260K}
1	4	11431	-624	11439	-532	6	2	6071	219	5571	-287
1	5	16081	857	15590	286	6	3	2328	-336	2357	-411
1	6	3092	-280	2396	-1050	6	4	4790	-524	4989	-377
1	7	13189	-32	12479	-156	6	5	3156	-78	3240	172
1	8	4491	-529	4311	-84	6	6	1860	-586	2025	-349
1	9	5488	170	5353	379	6	7	4659	-432	4607	-57
1	10	3532	-522	3980	-335	6	8	9979	407	10039	516
1	11	4213	-111	3754	-626	6	9	1802	107	1627	-409
1	12	10706	1055	10206	367	6	10	3404	-191	3899	438
1	13	6955	-125	6707	-187	7	0	9220	267	9698	1030
2	3	7043	-463	7836	-2	7	1	10176	696	10158	780
2	4	20172	787	20031	-134	7	2	2546	-604	2468	-323
2	5	5309	-270	5805	151	7	3	4295	-994	4498	-619
2	6	7888	-43	7816	261	7	4	1739	-541	1570	-554
2	7	8380	-770	8425	-171	7	5	2858	-377	3684	534
2	8	9475	167	9861	782	7	6	2275	-1005	2858	-492
2	9	6540	604	6275	6	7	7	7771	1138	8028	813
2	10	4259	-619	4934	-205	7	8	1851	202	1347	-408
2	11	4952	-318	5323	-637	7	9	3662	-185	3492	-324
2	12	3977	-275	4189	-422	8	0	2754	-711	2747	-84
2	13	1678	-226	1538	-379	8	1	1871	-483	2136	-242
3	2	12827	825	13066	1068	8	2	5345	-588	5500	-601
3	3	2226	-170	3220	1225	8	3	4887	238	4981	637
3	4	14977	1012	14739	406	8	4	2922	-444	3318	18
3	5	13749	-764	14496	107	8	5	7369	617	7682	1056
3	6	3890	-704	4084	-305	8	6	4539	-617	4403	-909
3	7	6573	-331	6920	-10	8	7	3939	-402	3730	-377
3	8	4812	27	4706	586	8	8	5597	116	5383	161
3	9	3046	676	3328	829	9	0	4614	-47	4425	115
3	10	2558	254	2569	-100	9	1	7527	-862	8072	-441
3	11	7163	-104	6967	-74	9	2	4812	595	4228	85
3	12	4641	147	4737	130	9	3	5257	-262	5395	-151
4	0	12316	-128	12323	268	9	4	4732	109	5118	-79
4	1	15136	-94	14535	-749	9	5	5442	227	5391	-439
4	2	10774	-401	10867	-309	9	6	4028	-304	3658	-624
4	3	23590	-351	23737	-257	9	7	1660	-45	1487	-450
4	4	6353	556	6352	286	10	0	2566	-907	2428	-1523
4	5	4991	-630	5716	413	10	1	2418	273	2492	406
4	6	3611	-141	3426	188	10	2	5884	264	6361	381
4	7	5385	627	5464	851	10	3	8696	-546	8741	-288
4	8	5294	40	5893	777	10	4	1941	332	1564	-424
4	9	5181	428	4726	-319	10	5	6360	632	6451	806
4	10	6408	312	6640	250	10	6	2700	-65	2559	-117
4	11	2833	463	3044	911	11	0	5527	294	5711	443
5	0	17011	102	16897	-504	11	1	6225	993	5929	1241
5	1	4958	-131	4704	-157	11	2	4717	-903	5372	-83
5	2	17205	-142	16914	-663	11	3	4034	43	3648	-295

H	K	F_{M240K}	ΔF_{M240K}	F_{M260K}	ΔF_{M260K}	H	K	F_{M240K}	ΔF_{M240K}	F_{M260K}	ΔF_{M260K}
5	3	5136	-892	4902	-1048	11	4	1303	4	1160	-299
5	4	2518	-464	2730	46	11	5	5525	-116	5388	127
5	5	3204	143	2412	43	12	0	4457	-228	4928	67
5	6	3588	-161	3613	-305	12	1	1568	411	1094	-510
5	7	6044	-220	5763	-414	12	2	3143	338	3435	972
5	8	1526	-158	1580	-571	12	3	1581	-224	1615	-843
5	9	1579	32	1479	-377	13	0	3605	-747	4520	288
5	10	2121	-249	2328	-166	13	1	5465	-60	5318	-45
5	11	2415	-702	1746	-1216	13	2	6094	458	5970	402
6	0	12136	-10	12859	672	14	0	3156	1100	2604	349
6	1	14325	208	13970	-68						

peaks with more than four contour levels appear near helices E and G. The highest peak is the one near helix G, with six contour levels. The most prominent negative peak appears directly over the position of the Schiff base. Fig. 5-2 shows the difference noise map between two independent halves of the M_{240K} data set. Almost every peak in this noise map is within two contour levels. The height of peaks introduced by the formation of the M_{240K} intermediate (Fig. 5-1) is obviously much higher than the height of peaks caused by noise alone (Fig. 5-2).

The difference map between the M_{260K} and the bR_{260K} reference data set is shown in Fig. 5-3. Major positive peaks that are higher than four contour levels appear near helices B, F and G. The major negative peaks appear near helices F and G. Fig. 5-4 represents the difference noise map between two independent M_{260K} data sets. Almost all peaks in this noise map are within two contour levels, which again are obviously much lower than the peak heights detected in the M_{260K} difference map.

Fig. 5-5 shows the M_{260K} minus M_{240K} difference map calculated by subtracting Fig. 5-1 from Fig. 5-3. A major positive peak with five contour levels appears between helices C and G, very close to the projected position of the Schiff base. Another positive peak with five contour levels appears between helices C and D.

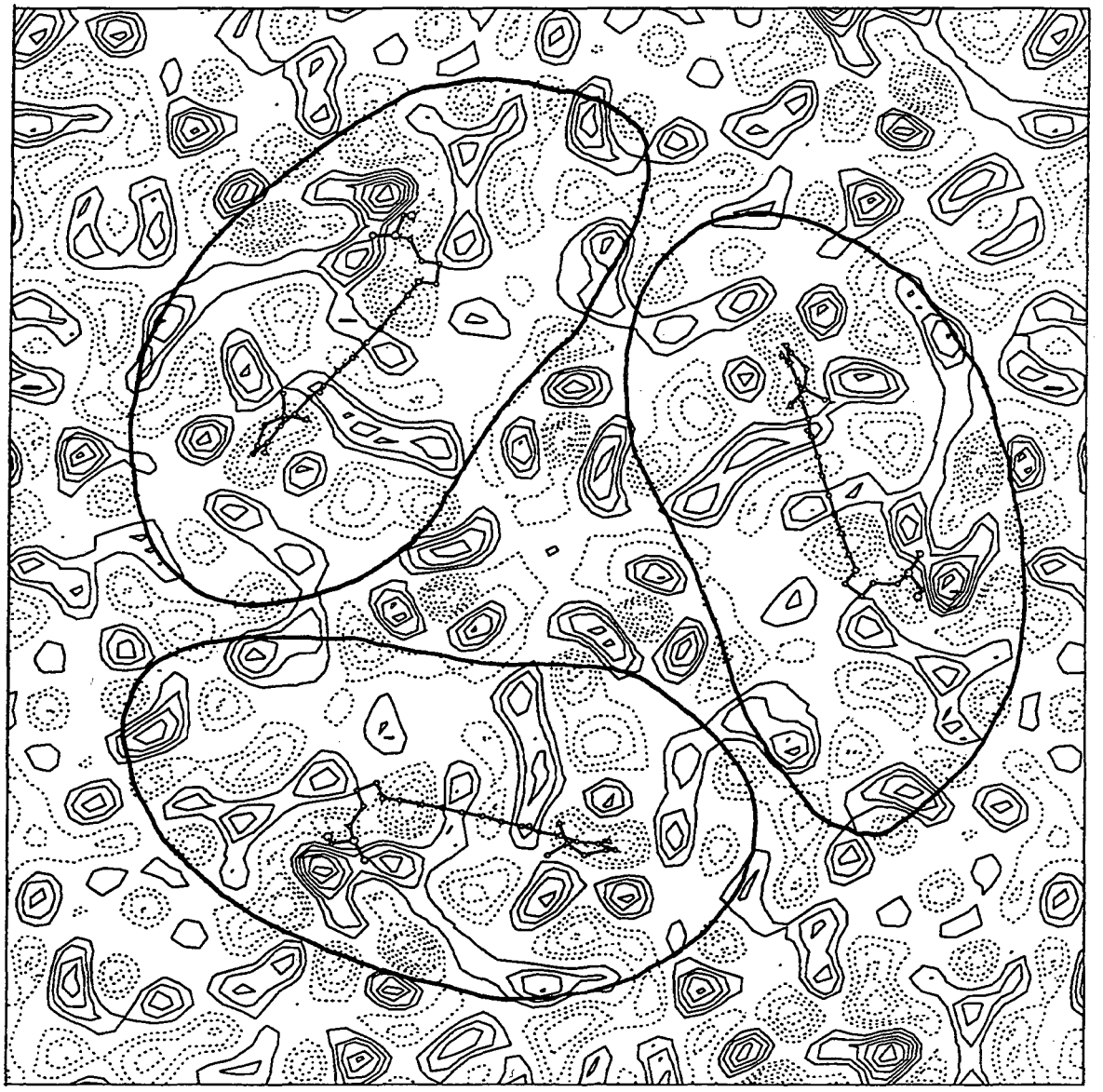

Figure 5-1. Difference map of structural changes that occur in the formation of M_{240K} at -33 °C, obtained using 12 illuminated and 14 unilluminated crystals, at 3.8 Å resolution. The map was contoured at one tenth of the contour level used for the projection map shown in Fig. 3-3. Continuous lines represent positive signals and discontinuous lines negative signals. The approximate protein boundary of each monomer is drawn. The positions of lysine 216 and retinal are superimposed on the map.

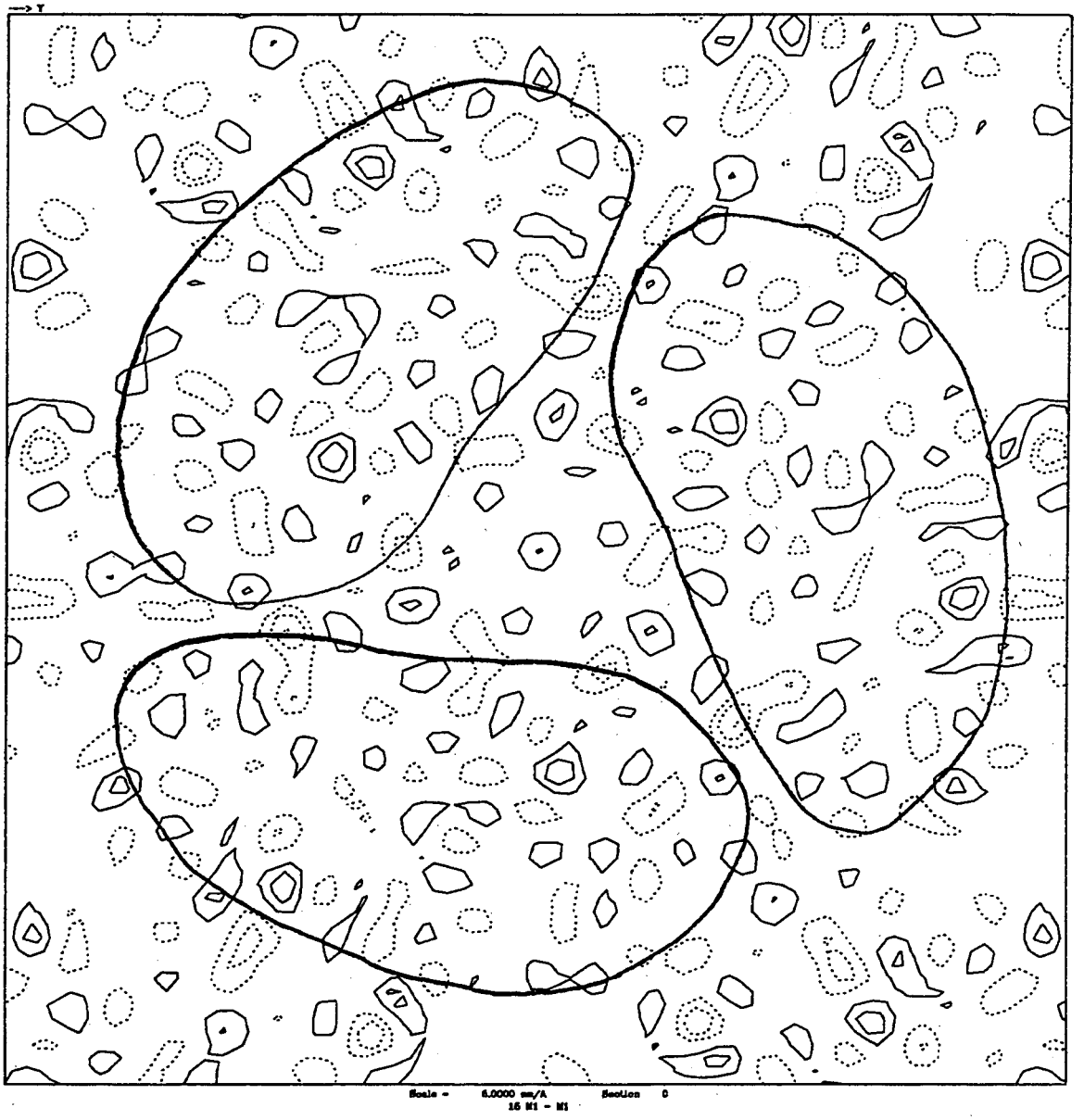

Figure 5-2. Difference noise map between two independent M_{240K} data sets, each consisting of 6 films.

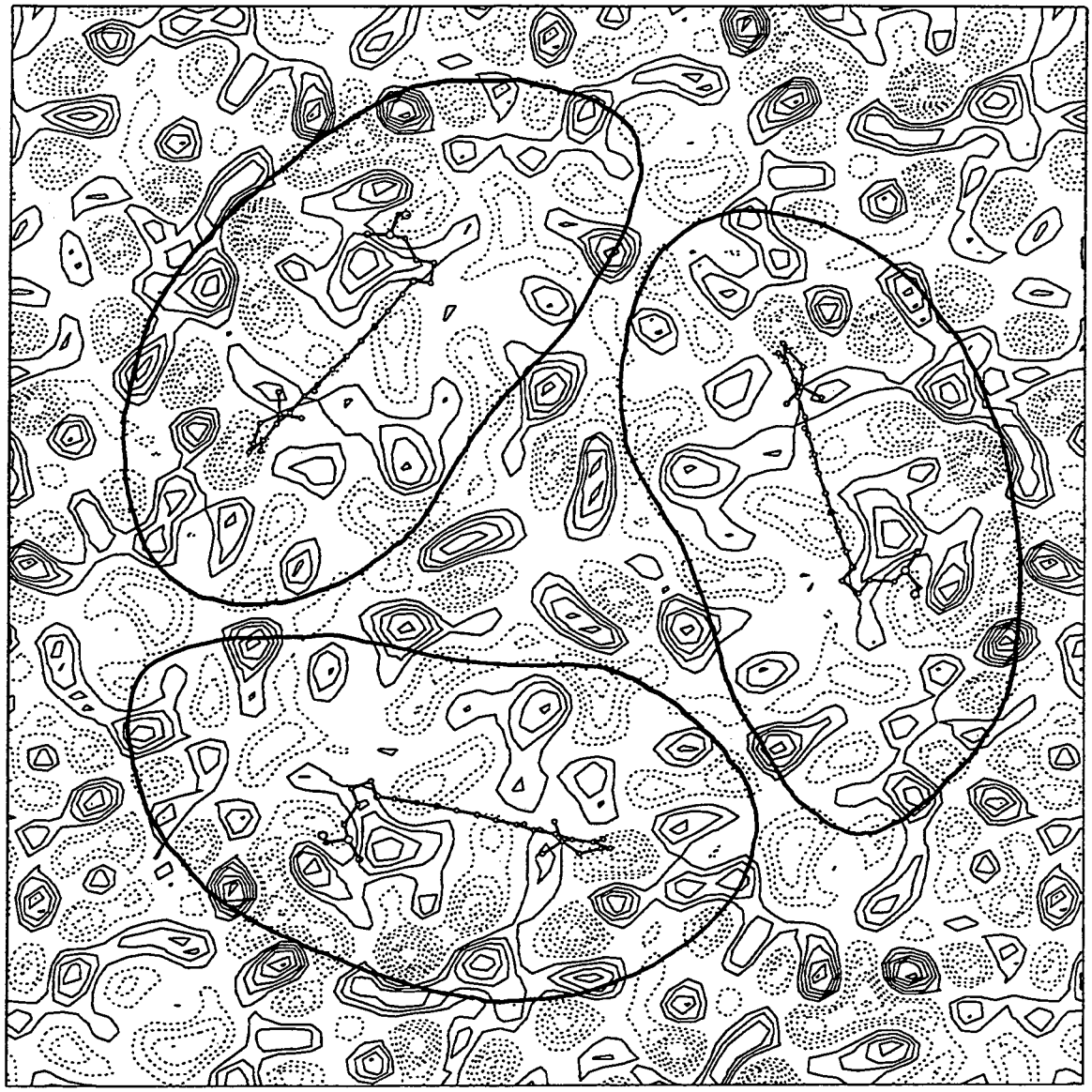

Figure 5-3. Difference map of structural changes that occur in the formation of M_{260K} at -13 °C, obtained using 14 illuminated and 12 unilluminated crystals. The positions of lysine 216 and retinal are superimposed on the map.

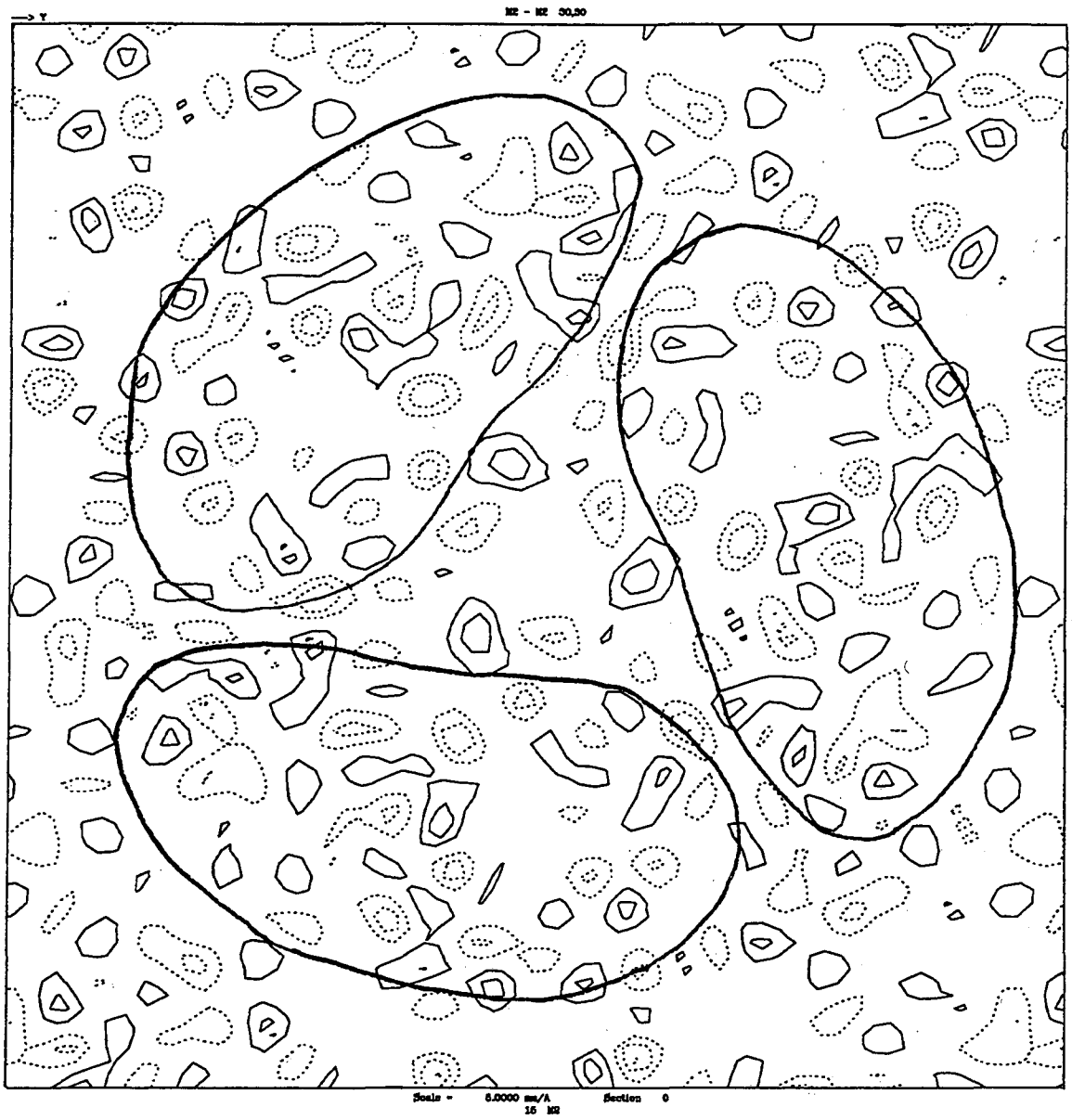

Figure 5-4. Difference noise map between two independent M_{260K} data sets, each consisting of 7 films.

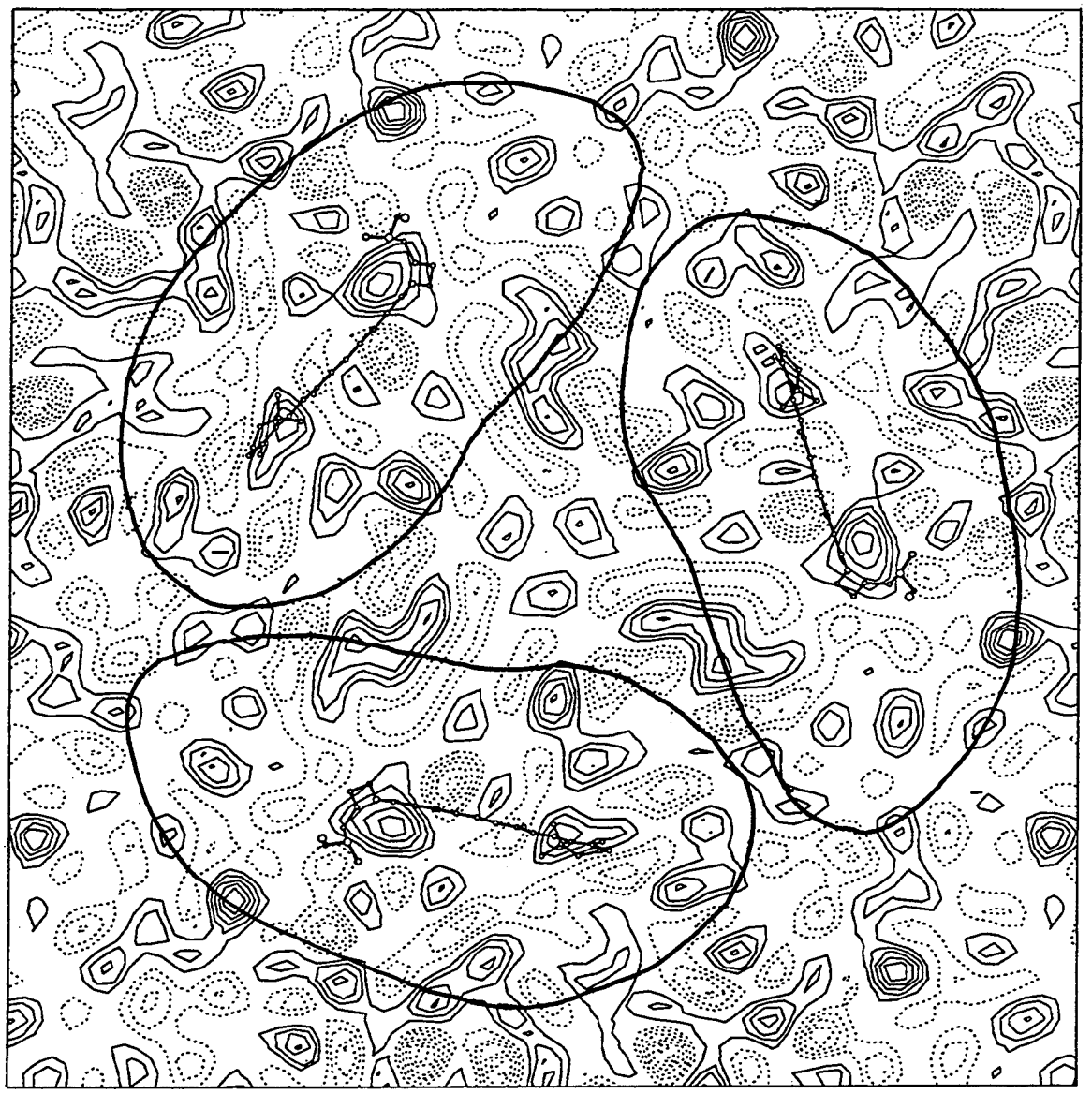

Figure 5-5. Difference map of structural changes that occur during the transition from the M_{240K} substate to the M_{260K} substate, obtained by subtracting Fig. 5-1 from Fig. 5-3.

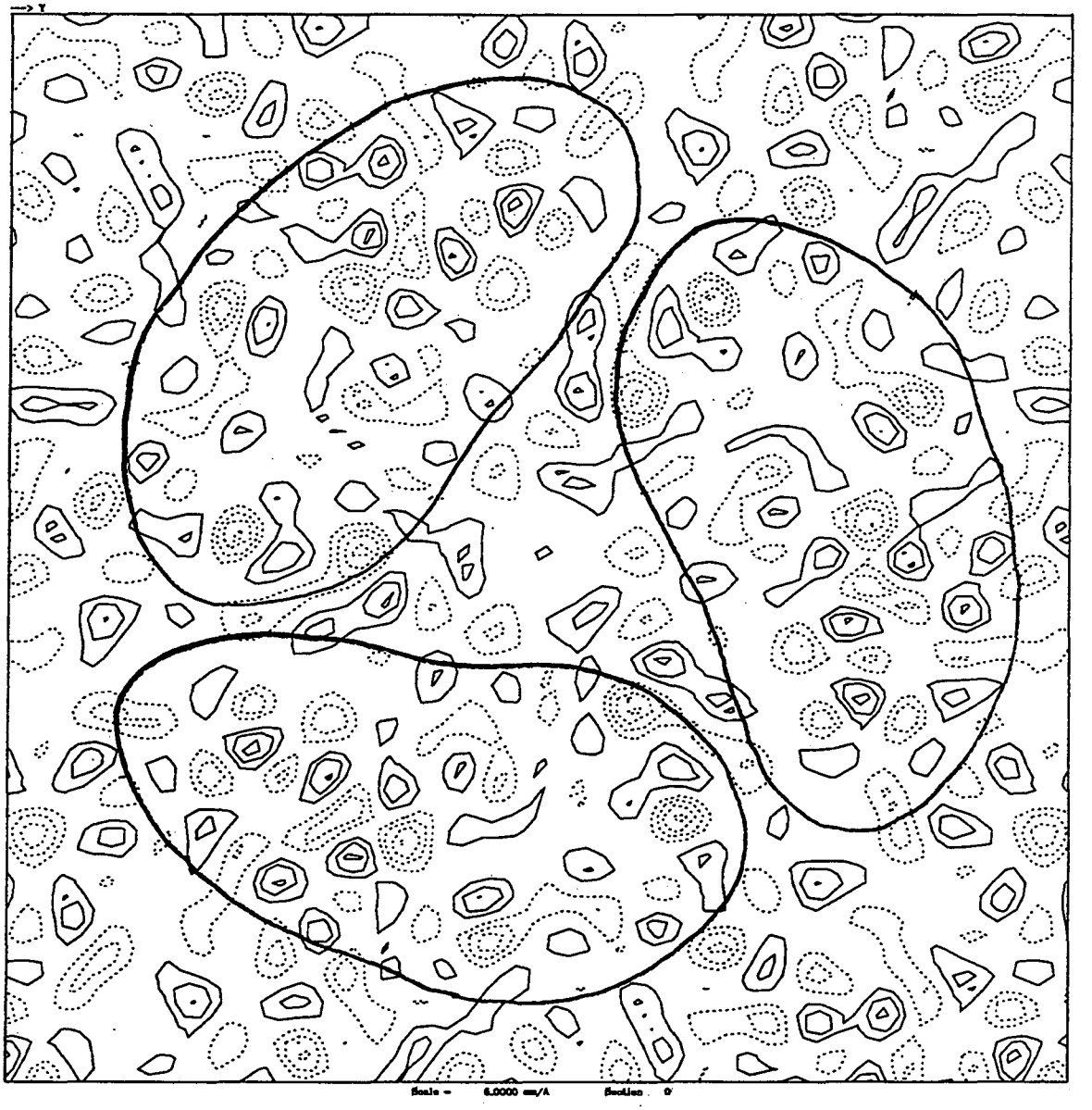

Figure 5-6. Difference map obtained by subtracting the bR_{240K} diffraction amplitudes from the bR_{260K} diffraction amplitudes.

These two positive peaks appear to be coupled with nearby negative peaks.

The difference map between the bR_{260K} and bR_{240K} reference data sets is shown in Fig. 5-6. The peaks in this map represent both random errors in measurement plus potential systematic signals introduced by the different thermal history involved in the sample preparation techniques for these two reference data sets. The peak levels of the bR_{260K} minus bR_{240K} map shown in Fig. 5-6 are slightly higher than those of the M_{240K} and M_{260K} noise maps shown in Fig. 5-2 and 5-4, both of which are formed from data collected from samples that had a single thermal history. This bR_{260K} minus bR_{240K} map therefore suggests that the different thermal cycling techniques used here to form the M_{240K} and M_{260K} substates can introduce a small amount of non-random signal. These data confirm that it is worthwhile to continue to use appropriate reference samples (bR_{240K} and bR_{260K}, respectively) when calculating the M_{240K} and M_{260K} difference maps.

5.2 Statistical evaluation

To test the accuracy of the difference amplitude data, I divided each initial set of data into two data sets, and derived measurements of F(h,k,0) from each data set. ΔF(h,k,0) data sets were constructed in two different ways for M_{240K} and M_{260K} data sets. In the first case, the measured M amplitude data were divided randomly into two halves and two separate, independent F(h,k,0) values were derived from these two M amplitude data sets as described in Chapter 3, Experimental Methods. All measured bR data, however, were used to produce a single F(h,k,0) data set. Two difference amplitude data sets were then constructed by subtracting the single bR, reference F(h,k,0) data set from the two independent M data sets.

In the other case, both the M and the bR data sets were randomly divided into two halves, and two independent F(h,k,0) data sets were derived for bR as well as for M. Two independent difference amplitude data sets were then constructed by subtracting independent bR reference data sets from independent M data sets.

The similarity between independent data sets was evaluated by calculating the correlation coefficient (Hoel, 1971):

$$C = \frac{\Sigma \Delta F_1 \Delta F_2 - \dfrac{\Sigma \Delta F_1 \Sigma \Delta F_2}{n}}{\left\{\Sigma (\Delta F_1)^2 - \dfrac{(\Sigma \Delta F_1)^2}{n}\right\}^{1/2} \left\{\Sigma (\Delta F_2)^2 - \dfrac{(\Sigma \Delta F_2)^2}{n}\right\}^{1/2}}$$

where ΔF_1 and ΔF_2 are the difference amplitudes of the first and second data sets and n is the total number of terms in the indicated summation. The calculated correlation coefficients for several different resolution zones are summarized in Table 2 and Table 3 for the M_{240K} and M_{260K} data sets, respectively. The overall correlation coefficient of the M_{240K} data set for all reflections is slightly higher than that of M_{260K} (0.91 vs. 0.90) when single bR_{240K} and bR_{260K} reference data sets were used. The overall correlation coefficient of the M_{260K} data set is, however, higher than that of M_{240K} (0.79 vs. 0.68) when two independent reference data sets were used.

The number of atoms that would have moved by a distance comparable to the resolution of each resolution zone was estimated using statistical evaluation as follows (Glaeser et al., 1986):

$$m = N\left(\frac{<|\Delta F|>}{<|F|>}\right)^2$$

Table 2

Statistical evaluation of the differences in diffraction amplitudes for bR_{240K} and M_{240K}.

Resolution zone (Å)	Number of reflections	Correlation # coefficients	m*	Correlation † coeffcients	m*
15.0 - 7.2	26	0.89	2.6	0.84	2.9
7.2 - 5.3	28	0.95	21.9	0.76	21.7
5.3 - 4.4	30	0.89	22.3	0.74	14.0
4.4 - 3.8	31	0.88	22.3	0.40	6.5
All reflections	115	0.91		0.68	

The values of ΔF_1 are difference amplitudes between 6 M_{240K} and 14 bR_{240K} diffraction patterns. The values of ΔF_2 are difference amplitudes between another 6 M_{240K} and the same 14 bR_{240K} diffraction patterns.

† The values of ΔF_1 are difference amplitudes between 6 M_{240K} and 7 bR_{240K} diffraction patterns. The values of ΔF_2 are difference amplitudes between another 6 M_{240K} and another 7 bR_{240K} diffraction patterns.

* m represents the estimated number of atoms that would have moved to produce the observed difference amplitudes.

Table 3

Statistical evaluation of the differences in diffraction amplitudes for bR_{260K} and M_{260K}.

Resolution zone (Å)	Number of reflections	Correlation # coefficients	m*	Correlation † coeffcients	m*
15.0 - 7.2	26	0.91	3.5	0.88	5.2
7.2 - 5.3	28	0.88	15.7	0.69	14.6
5.3 - 4.4	30	0.93	22.6	0.82	21.1
4.4 - 3.8	31	0.89	15.7	0.72	13.1
All reflections	115	0.90		0.79	

The values of ΔF_1 are difference amplitudes between 7 M_{260K} and 12 bR_{260K} diffraction patterns. The values of ΔF_2 are difference amplitudes between another 7 M_{260K} and the same 12 bR_{260K} diffraction patterns.

† The values of ΔF_1 are difference amplitudes between 7 M_{260K} and 6 bR_{260K} diffraction patterns. The values of ΔF_2 are difference amplitudes between another 7 M_{260K} and another 6 bR_{260K} diffraction patterns.

* m represents the estimated number of atoms that would have moved to produce the observed difference amplitudes.

N is the total number of atoms, estimated to be 2300 (1913 atoms from bR and ~400 atoms due to lipid molecules, excluding hydrogen) within the unit cell. $<|F|>$ is the mean value of the modulus of the structure factor within each resolution zone. $<|\Delta F|>$ is the estimated value of the true modulus of the difference structure factor calculated from

$$<|\Delta F|> = (c<|\Delta F_1|><|\Delta F_2|>)^{1/2}$$

where $<|\Delta F_1|>$ and $<|\Delta F_2|>$ are the mean values, within each resolution zone, of the modulus for the two data sets and c is the correlation coefficient. In the case of the M_{240K} data set, when a single bR_{240K} reference data set was used, m starts small (2.6) in the low resolution zone, increases more than 8 times in the next resolution zone, and stays almost the same for higher resolution zones. When two independent bR_{240K} data sets were used as references, the M_{240K} data set shows a maximum value for m in the 7.2-5.3 Å resolution zone. In the case of M_{260K}, the m value is small for the low resolution zone, becomes maximum within the 5.3-4.4 Å resolution zone, and decreases somewhat in the last resolution zone. There is no significant difference in the estimated m values in the case of the M_{260K} data sets, when the two different procedures of generating $\Delta F(h,k,0)$ values are compared.

5.3 Comparison with previously published data

Table 4 represents the correlation coefficients between the ΔF's that I have measured for the two M substates, and previously published difference amplitude data sets for the M intermediate. The electron amplitude data from Subramaniam et al. were measured out to 3.5 Å resolution and my data were limited to 3.8 Å, whereas the X-ray amplitude data from Nakasako et al. and Koch et al. were limited to 7 Å and involved the superposition of diffraction orders with identical (or unresolved) Bragg spacings. The difference amplitude data from Subramaniam et al. (1993) for the D96G mutant specimen are much more highly correlated with the M_{260K} than with the M_{240K} substate (0.81 vs. 0.43 for the low resolution zone (15.0 - 7.2 Å) and 0.69 vs. 0.34 for the full, 15.0 - 3.8 Å resolution zone). The ΔF's obtained by Subramaniam et al. for the wild type M intermediate, however, are more highly correlated with M_{240K} than M_{260K} for the low resolution zone and equally correlated with M_{240K} and M_{260K} for the whole data. The X-ray difference amplitude data from Koch et al. is slightly better correlated with M_{240K} than with M_{260K}, while the X-ray difference amplitude data from Nakasako et al. is more highly correlated with the M_{260K}

Table 4

Correlation coefficients between the M substates and previously published difference amplitude data sets for the M intermediate.

	$F_{M\,240K}$-$F_{bR\,240K}$		$F_{M\,260K}$-$F_{bR\,260K}$	
	Resolution zone			
	15.0-7.2Å	15.0-3.8Å	15.0-7.2Å	15.0-3.8Å
Subramaniam et al. (1993)				
D96G mutant	0.43	0.34	0.81	0.69
wild type	0.60	0.52	0.39	0.52
Koch et al. (1991)	0.62	-	0.57	-
Nakasako et al. (1991)	0.44	-	0.63	-
F_{M240K}-F_{bR240K}	1.00	1.00	0.49	0.58
F_{M260K}-F_{bR260K}	0.49	0.58	1.00	1.00

difference amplitude data than with the M_{240K} difference amplitude data. As a reference, correlation coefficients for my M_{240K} and M_{260K} difference amplitude data sets were calculated. The correlation coefficient between the M_{240K} and M_{260K} data sets is 0.58 for the whole data, which is considerably lower than the correlation coefficients obtained for two halves of the M-bR data sets in Table 2 and Table 3 (0.91 and 0.90 for M_{240K} and M_{260K}, respectively). The M_{260K} intermediate is more highly correlated with the D96G mutant specimen of Subramaniam et al. than with the M_{240K} intermediate (0.69 vs. 0.58).

5.4 Discussion

I have shown that reproducible differences exist between difference maps, using electron diffraction data collected for samples of humidified, glucose embedded purple membrane that have been illuminated by green light at 240K and 260K. At both temperatures, only M is trapped, as shown by Perkins et al. (1992) using visible absorption spectroscopy. Exclusive formation of M under these conditions is further confirmed by the fact that blue light, which is only appreciably absorbed by the M_{412} intermediate, can drive the FTIR spectrum of such samples completely back to the bR ground state. From this evidence it can be concluded that there are at least two M-substates, each with a different protein conformation.

The initial FTIR evidence for two substates of the M-intermediate (Ormos, 1991) has been called into question in a subsequent paper by Ormos et al. (1992). In the later experiments Ormos et al. used blue light to selectively remove the M-intermediates from a previously photo-activated sample. In this way M minus bR difference spectra were constructed by subtracting spectra obtained before and after blue light illumination. Ormos et al. found that there is only one type of FTIR difference spectrum produced in this way between M and bR_{568}, regardless of the temperature of the experiment, and this spectrum is similar to the

previous M_{240K}-bR difference spectrum published by Ormos (1991). Ormos proposed that the earlier M_{260K} difference spectrum represented a mixture of a single M intermediate and the N intermediate.

The blue light photoreversal method introduced by Ormos was used to check for the presence of non-M intermediates produced in our sample preparation protocol. This result (Fig. 1-4) clearly showed that pure M is trapped at 240K and a mixture of M_{240K} and another M substate, presumably M_N, is trapped at 260K (Vonck et al, 1994).

The explanation for this difference must lie in the use of different sample preparation conditions. While Ormos' samples are fully hydrated, our glucose-embedded samples are only partially hydrated. It is well known that the hydration level has a profound influence on the photocycle. Specifically, the M_1 to M_2 step as well as the M to N step are slowed in partially dehydrated samples (Varo and Lanyi, 1991c; Cao et al., 1991), while glucose-embedded samples do not form M at all at low temperature without taking precautions against dehydration (Perkins et al., 1993). In our case, the partial dehydration seems to inhibit the M to N step at 260K, since in otherwise similar conditions the fully hydrated samples used by Ormos et al. form N, while the humidified, glucose-embedded samples form only M.

Sasaki et al. (1992) recently showed the existence of an intermediate (which they called M_N) with the protein structure of N but a deprotonated Schiff base indicative of M. This intermediate was trapped in the D96N mutant (which lacks the aspartate group that reprotonates the Schiff base in the M to N step), at high pH (to prevent Schiff base reprotonation from the medium). Apparently the protein structural change giving rise to the N intermediate had taken place in this sample, but due to lack of a proton to reprotonate the Schiff base, the retinal remained in the deprotonated configuration specific for M.

Assuming that this M_N intermediate is trapped in our samples as well, we can now reconcile our results (Vonck et al., 1994) quite easily with those of Ormos et al. (1992). The only difference would be that our 260K samples contain a mixture of M and M_N, while the samples in Ormos' experiments contained a mixture of M and N. In our case, then, unlike that of Ormos et al., all bR molecules could be photoreversed by blue light, which is absorbed by the retinal containing a deprotonated Schiff base.

The possibility that our M260K is a mixture of M and M_N substates is supported by electron diffraction data. If we assume that some M_N intermediate is trapped in our glucose-embedded

samples at 260K, and that the M-state of the D96G sample used by Subramaniam et al, is a pure M_N (like that of D96N), then we should expect that a linear combination of the diffraction data for the M_{240K} sample plus the diffraction data for the mutant bR M-state should correspond well with the diffraction data for the M_{260K} sample. Fig. 5-7 shows that the correlation coefficient between the M_{260K} diffraction data and the linear combination described above takes a maximum value of 0.78 at a ratio of 49% mutant and 51% M_{240K}. This maximum is much higher than the correlation coefficient between M_{240K} and M_{260K}, which is 0.58. Also, this maximum is much higher than the correlation coefficient between M_{mutant} and M_{260K}, which is 0.69. This indicates a good correspondence, as we had expected.

Fig. 5-8 shows a M-bR difference Fourier map made by mixing 49% mutant and 51% M_{240K} difference amplitude data. Almost all peaks in this map (Fig. 5-8) are in similar locations as those in the M_{260K} difference Fourier map (Fig. 5-3), supporting the idea that our M_{260K} samples are a mixture of pure M_{240K} and M_N. Fig. 5-9 shows the difference between my M_{260K} difference map (Fig. 5-3) and the "mixture difference map" (Fig. 5-8). The peaks in this difference map represents the random noise plus systematic signals introduced by different sample preparation protocols between our experiment and mutant experiment (Subramaniam et al., 1993). The

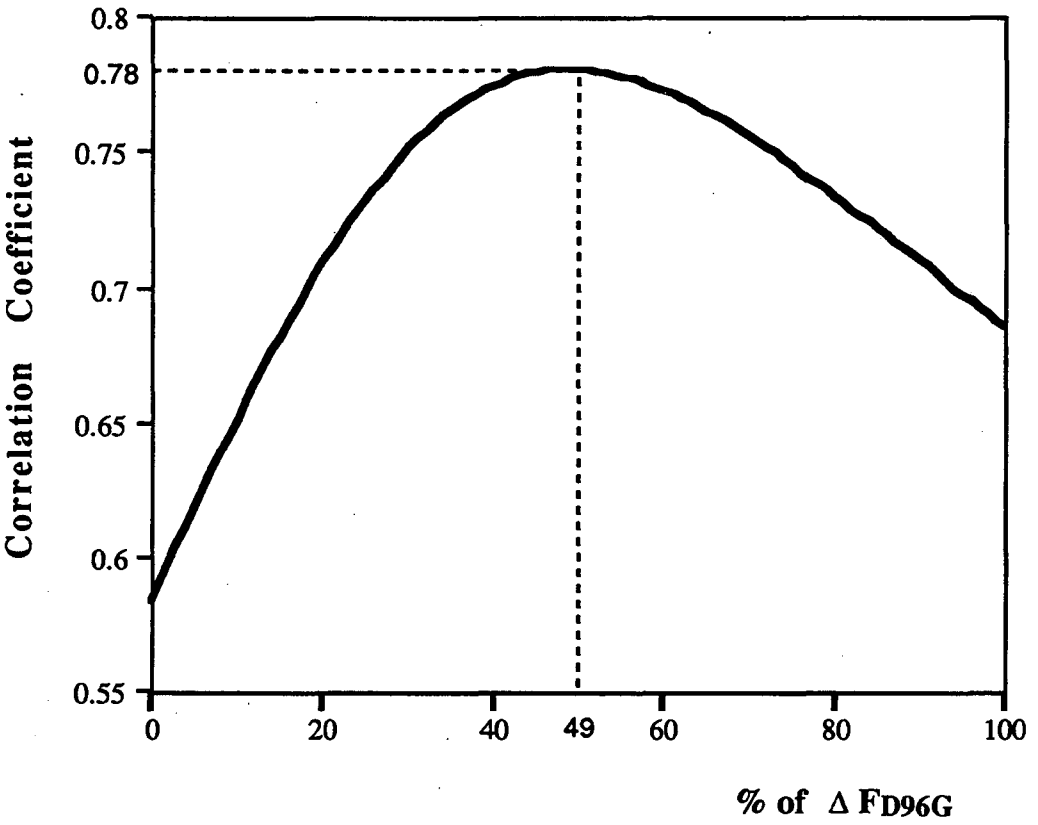

Figure 5-7. Correlation coefficients of M-bR electron diffraction amplitude data. Linear combinations were made of the M-bR difference amplitudes, ΔF_{M240K} (Han et al., 1994a) and ΔF_{MD96G} (Subramaniam et al., 1993). Correlation coefficients were calculated between the mixtures and ΔF_{M260K} (Han et al., 1994a).

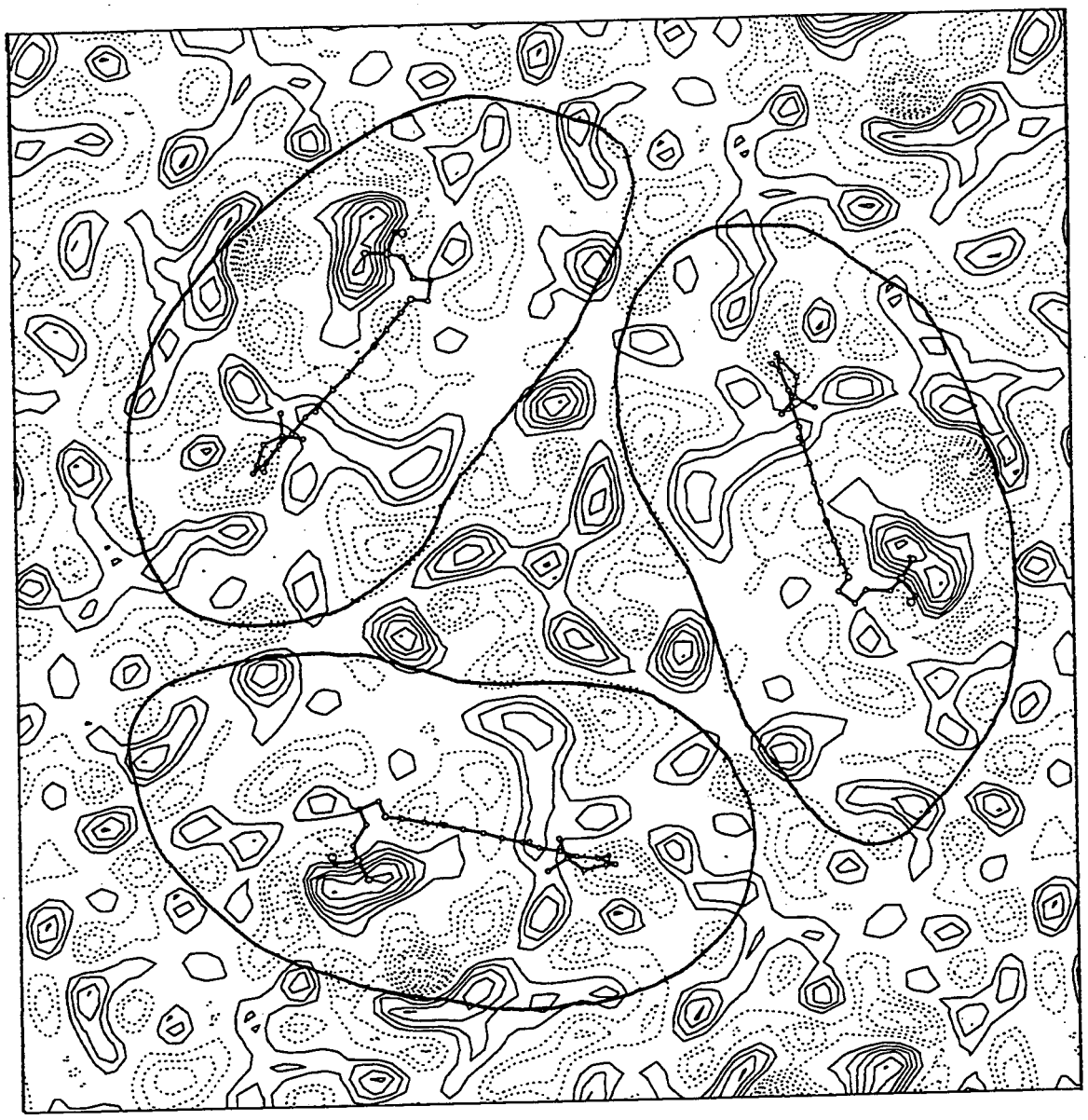

Figure 5-8. A synthesized difference map made by mixing the M-bR difference amplitudes, ΔF_{M240K} (Han et al., 1994a) and ΔF_{MD96G} (Subramaniam et al., 1993) at the ratio of 51% and 49%, respectively.

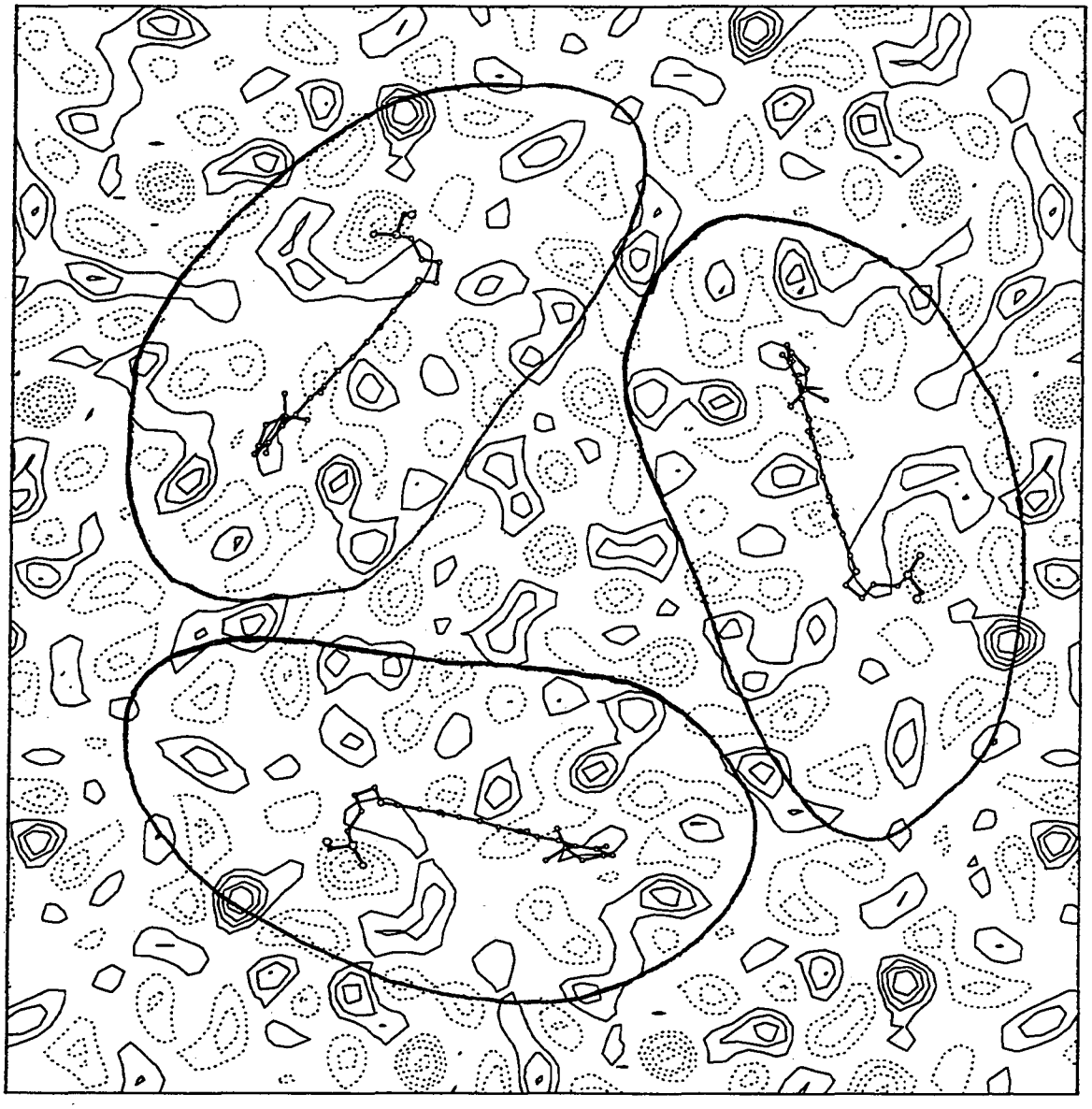

Figure 5-9. The difference noise map made by subtracting the synthesized difference map (Fig. 5-8) from the M_{260K} difference map (Fig. 5-3).

height of peaks in this map is obviously lower than that in the mixture difference map (Fig. 5-8).

The optimal ratio of M and M_N estimated from the correlation curve, Fig. 5-7, is similar to the ratio that also best accounts for the M_{260K} FTIR difference spectrum as a mixture of M and N FTIR spectra, confirming the previous conclusion that M_{260K} sample is a mixture of M_{240K} and M_N (Vonck et al., 1994).

While there may be many possible reasons why our humidified, glucose-embedded samples are not able to reprotonate the Schiff base (at 260K), once the M_N intermediate has been formed, we would like to mention two alternative models that seem to be especially worth consideration. The first model proposes that the cytoplasmic half of the proton-transport channel normally contains a string of continuously hydrogen-bonded water molecules, which serve as the "proton wire" to transfer the proton from asp96 to the deprotonated Schiff base (Nagle, 1987; Deamer and Nichols, 1989). If as few as one of these water molecules would be removed in the glucose-embedded state, reprotonation of the Schiff base would no longer be possible. However, it has been shown by Cao et al. (1991), in an analysis of osmotic effects on the photocycle, that much more water is essential for the reprotonation step than the amount that would form a single, 12 Å line of water molecules. The

second model is inspired by the suggestion of Subramaniam et al. (1993) that a widening of the structure occurs on the cytoplasmic surface in the M-state of the D96G mutant, which we now believe to be an N-like (i.e. M_N) protein conformation. In this model, the M to M_N transition introduces the opening of a cleft or channel where water can flow in, and proton transfer is then possible from asp96 to the Schiff base. If no free water is available when the M_N state is formed, as may be the case in our glucose embedded samples, proton transfer from asp96 to the Schiff base could not occur. This second model is attractive in that: (1) The aqueous hydration of asp96 which would occur provides a natural explanation for the large decrease in pKa which causes the carboxylic acid group of asp96 to dissociate. (2) Direct, aqueous communication between the cytoplasmic side of the protein and the Schiff base, postulated in this model, explains how the Schiff base can be reprotonated in the D96N mutant, and why the rate of that reprotonation depends upon the bulk pH (Holz et al., 1989; Cao et al., 1991). (3) Creation of a water-filled channel on the cytoplasmic side of an N-like state in hR can be easily pictured as allowing vectorial release of Cl^- to the cytoplasm in the halorhodopsin photocycle.

What is the relationship of the M intermediate found in our experiments, to the kinetically and spectroscopically identified M_1 and M_2 intermediates in the photocycle? Sasaki et al. (1992) suggest

that the M intermediate that occurs together with M_N presents the M_2 intermediate and M_N is a normally unstable intermediate between M_2 and N. Evidence for this interpretation is the apparent equilibrium between M and M_N as seen in the decay of the D96N sample (Sasaki et al., 1992). If this interpretation is correct, the photocycle around the M-intermediate can be described as $L \leftrightarrow M_1 \rightarrow M_2 \leftrightarrow M_N \leftrightarrow N$. The M state that is normally seen in FTIR spectra would then be M_2. This is supported by the observation that in the few experiments in which different M substates are resolved, M_1 appears as a transient intermediate during the rise of M (Varo and Lanyi, 1991a; Zimanyi et al., 1992; Varo et al., 1992).

One can speculate on the possibility that M_1 (which has never been resolved in FTIR experiments) has a similar protein structure as L, essentially only differing in the protonation states of asp85 and the Schiff base, and could be named "M_L" in analogy with M_N in the nomenclature of Sasaki et al. (1992). The resulting photocycle can be represented as $bR \rightarrow K \leftrightarrow L \leftrightarrow M_L \rightarrow M \leftrightarrow M_N \leftrightarrow N \leftrightarrow O \rightarrow bR$. During the light-induced $bR \rightarrow K$ reaction, the retinal isomerizes from the all-trans to the 13-cis form (Braiman and Mathies, 1982). In $K \rightarrow L$, the protein relaxes to accommodate the changed geometry of the retinal, in a way that changes the pKa of the Schiff base and/or asp85 (Varo and Lanyi, 1991b). Subsequently, in the $L \rightarrow M_L$ step, the Schiff base proton is transferred to asp85. This is followed by

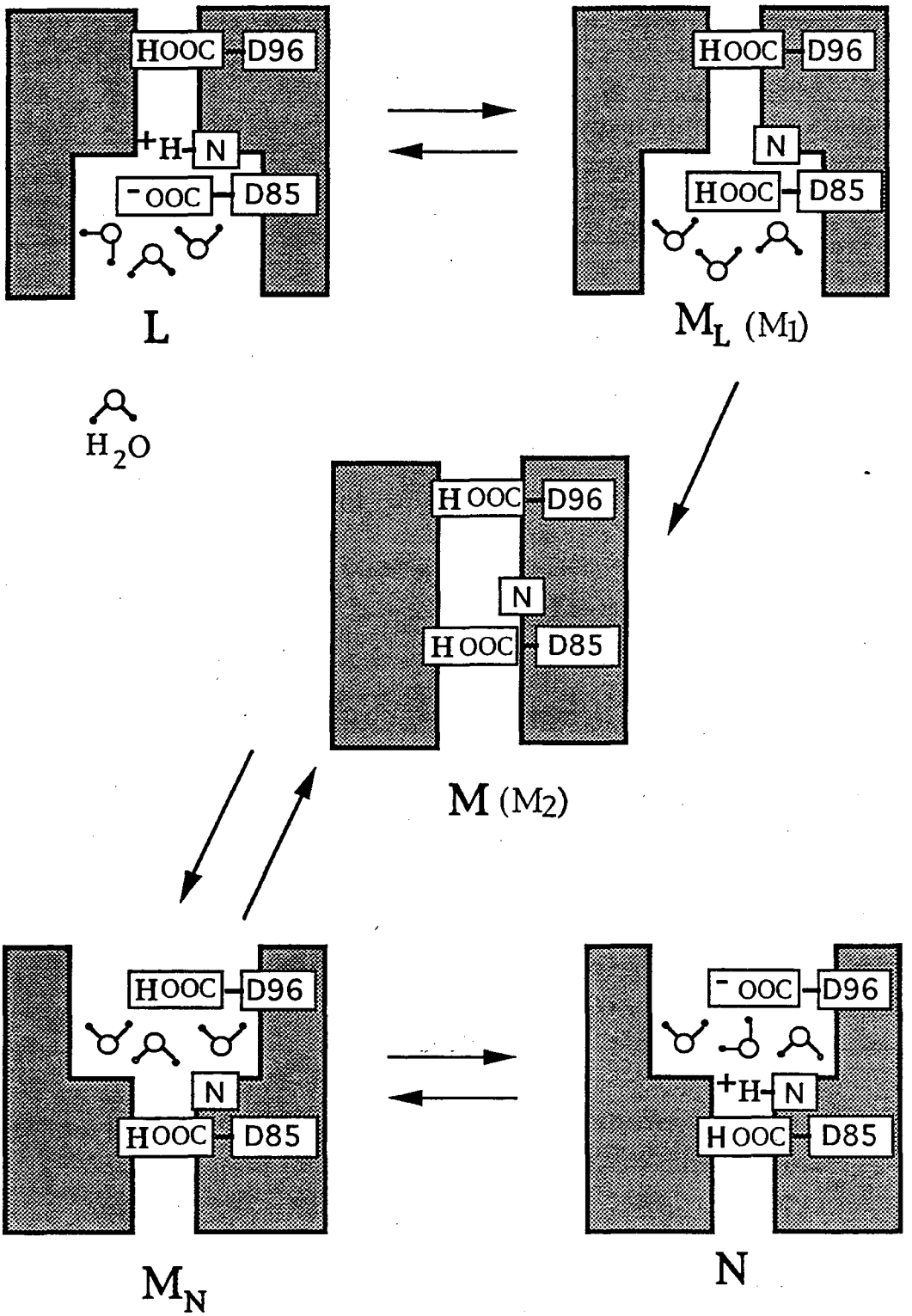
HOOC
D96
+H
N
-OOC
D85
L
M_L (M_1)
H_2O
M (M_2)
M_N
N

Figure 5-10. A proposed photocycle scheme including 3 M substates, M_L, M, and M_N. Three protein conformations are proposed. In the first protein conformation, L and M_L are in equilibrium and have outward facing channels, exposing aspartate 85 to water to facilitate proton transfer from the Schiff base to aspartate 85. In the second protein conformation, the extracellular proton channel is closed and water is no longer available to aspartate 85, stabilizing the protonated form of aspartate 85. The third protein conformation has an inward facing channel that has opened up, exposing aspartate 96 to water so as to facilitate proton transfer from aspartate 96 to the Schiff base.

the $M_L \rightarrow M$ (or in the earlier nomenclature $M_1 \rightarrow M_2$) conformational change, which, in our model closes the outward facing proton channel (Fig. 5-10). This involves withdrawal of asp 85 from the aqueous compartment, thus stabilizing the neutral, protonated carboxyl group. In M, the deprotonated Schiff base is consequently not accessible from either side, but in the $M \rightarrow M_N$ step an inward facing channel opens and the inflowing water allows transport of the now destabilized asp96-proton to the Schiff base (Fig. 5-10). In $N \rightarrow O$ the retinal reisomerizes (Smith et al., 1983) and the outward facing channel reopens, asp 85 deprotonates and the protein relaxes to the ground state (Souvignier and Gerewert, 1992). The idea that active transport (and exchange transport) membrane proteins should cycle between inward facing and outward facing conformation is, of course, well-established, and, indeed, the first models that postulate cyclic access of the Schiff base of bR to opposite sides of the membrane have been proposed several years ago (Stoeckenius, 1979; Nagle and Mille, 1981).

The possibility to study the part of the photocycle around the M-intermediate and test the model described above by direct structural methods is quite promising at this point. Our electron diffraction study in projection shows the existence of a substantial conformational change in the M to M_N step. Subramaniam et al. (1993) have used the D96G mutant (which accumulates M due to

the absence of a proton donor for the Schiff base) to study the M intermediate by electron diffraction. It seems likely that they, like Sasaki et al. with the D96N mutant protein, have trapped predominantly the M_N intermediate, which is N-like in protein structure. If the mutant M-state is indeed not significantly contaminated by M, it will be more useful than our M_{260K} mixture for getting diffraction data, provided that the problem of getting adequate specimen flatness can be solved. If it can be shown that M_1 has a protein structure similar to L, trapping of L may be a way to study the changes associated with the M_1 to M_2 transition.

Chapter 6: PREPARATION OF FLAT SPECIMENS

6.1 Introduction

Multiple projections at tilt angles up to 60° or more are an important requirement for the reconstruction of a high-resolution, 3-dimensional density map. In the case of bacteriorhodopsin, missing data, ranging from 45° to 90° degree tilt angles, degraded the resolution of the electron density map from 3.5 Å in the membrane plane to 7-10 Å in the direction perpendicular to the membrane plane (Henderson et al., 1990).

The technical difficulty in preparing flat specimens represents a major drawback for collecting 3-D data sets. Imperfect flatness causes the electron diffraction spots in the direction perpendicular to the tilt axis to become blurred (Glaeser et al., 1991). The blurred diffraction spots can eventually overlap one another to such an extent that it is almost impossible to extract intensity data from individual spots.

Factors that determine whether a given carbon film will give good specimens have not been fully established. Butt et al. (1991) reported that the surface roughness of the carbon, on the mica-side

of the film, is decreased when the carbon is evaporated in multiple thin layers. They further suggest that the laminated structure which is produced in this way could be a governing factor in explaining why their carbon films could be used to prepare two-dimensional crystals of the Light Harvesting Complex that diffract sharply at tilt angles as high as 60 degrees. Glaeser et al. (1991) reported that heating the carbon film shortly after evaporation leads both to a significant increase of the hydrophobicity of the carbon film and to an improved likelihood that any given carbon film would support the preparation of flat specimens of purple membrane. Other factors that could, in principle, have a significant effect on the surface properties of the carbon film include (1) the type of mica used as substrate, (2) the rate of evaporation of the carbon, (3) the residual vacuum in the particular vacuum evaporator that is used, and (4) the partial pressure of hydrocarbons or other contaminants in the system.

The possibility that the type of carbon used for evaporation may be an important factor was also suggested by the consistent, exceptionally good quality of films made for us by Wang and Kühlbrandt in the EMBO Laboratory, Heidelberg. The possibility that starting material could be important seems at first to be improbable, due to the high purity of carbon sold for this purpose in all cases. In addition, the starting material is necessarily broken down into an atomic vapor, together with a smaller population of atomic clusters during evaporation (Martelli et al., 1983), and all

memory of the original bonding structure within the original carbon stock would have to be lost. Nevertheless, investigating whether the choice of carbon stock could explain subsequent differences in specimen flatness represented something to try, in the effort to understand how to overcome the problem of imperfect flatness.

We have found that the starting stock of carbon does in fact make a very big difference for the preparation of glucose-embedded, fused purple membranes. The type of evaporator or the type of mica, on the other hand, have no discernible influence under normal conditions (Han et al., 1994b).

6.2 Preparation methods

The sources of carbon rod and mica that are included in this study are summarized in Table 5. Each company provides several kinds of carbon rod with different degrees of purity. Ted-Pella Inc. provides Spectro-Tech grade carbon rods (Item number: 62-106) and Spectroscopically pure carbon rods (Item number: 60-11). Fullam Inc. provides spectroscopically pure carbon rods (Item number: Fullam 12020). Two different spectroscopically pure carbon rods (Item number: E416, E410), with different amount of impurities, were also purchased from Agar. E416 carbon rods from Agar are the same material as the 60-11 carbon rods from Ted Pella. Two different kinds of mica were purchased from Ted Pella, Inc. and from Agar.

Carbon was evaporated by resistive heating, onto freshly cleaved mica using two different models of Denton vacuum evaporator. An initial vacuum of 0.9×10^{-6} torr and 2.0×10^{-6} torr was achieved using the Denton 520A and Denton DV-502 evaporators, respectively, both of which were pumped by oil diffusion pumps, using a liquid N_2-cooled trap. The amount of carbon evaporated was adjusted to produce films with a thickness around 150 - 200 Å. Carbon films with similar thickness were mailed to us from Heidelberg. The carbon films made here were always stored at least

Table 5. Desciption of carbon rods, micas and number of independent experiments.

	Spectro-Tech grade carbon rods from **Ted Pella, Inc.**	Spectroscopically pure carbon from **Fullam**	Spectroscopically pure carbon rods from **Agar**	Spectroscopically pure carbon rods from **Agar**
Item number	62-106	12020	E416	E410
Purity	Impurities < 400ppm	Impurities :1000ppm	Impurities < 20ppm	Impurities < 2ppm
mica from **Ted Pella,** Inc.	more than 10 times	2 times	-	-
	blurred at 45°	sharp at 45°	-	-
mica from **Agar**	2 times	3 times	4 times	1 time
	blurred at 45°	sharp at 45°	sharp at 45°	blurred at 45°

5 days before use to have a consistent history with films mailed to us from Heidelberg.

The samples of glucose-embedded purple membrane were prepared using the "mica-facing" surface of the carbon film, as described by Glaeser and Downing (1990). Purple membranes were mixed with a glucose solution in pH 6.5, 10 mM MOPS buffer and loaded on a carbon film supported by a molybdenum (Mo) grid. A Mo grid was used in order to reduce the subsequent wrinkling of carbon film when the specimen is cooled to liquid nitrogen temperature (Glaeser, 1992; Booy and Pawley, 1993). The specimen grid was blotted with filter paper to remove extra solution, as described in Chapter 3 Experimental Methods, and transferred into a Gatan cryo-specimen holder.

The flatness of specimens prepared on different samples of carbon film was checked by tilting the grid to 45° and by observing the sharpness of diffraction spots in the direction perpendicular to the tilt axis. The sharpness of diffraction spots was first judged by looking briefly at images displayed from a Gatan TV monitor. Diffraction patterns were then recorded on SO163 film using a JEOL JEM 4000 EX electron microscope at an accelerating voltage of 400 kV.

6.3 Results

We have never been able to get flat purple membranes on carbon films made from Pella Spectro-Tech grade carbon rods (Item number: 62-106) (Table 5). In our experience, specimens made on this carbon are completely unusable at 45° tilt, even though they can give remarkably good diffraction patterns before tilting. Fig. 4-3 shows an electron diffraction pattern recorded from untilted purple membrane prepared on a Pella 62-106 carbon film. The diffraction spots extend out to 2.6 Å resolution. Fig. 6-1 shows the best possible electron diffraction pattern obtained at 45° tilt angle, using the same carbon film. The diffraction spots perpendicular to the tilt axis are so blurred that they cannot be separated.

In contrast to the consistently bad results that we have had with the Pella Spectro-Tech grade of carbon, we have repeatedly found that the carbon films made for us in Heidelberg were consistently excellent. Sharp diffraction patterns could be obtained routinely at a tilt angle of 45°, and acceptable patterns and images (Kühlbrandt and Wang, 1991) could be obtained with some frequency even at 60° tilt. The carbon stock used by Wang and Kühlbrandt is the stock item E416 purchased from Agar; evaporation is carried out in an oil diffusion-pumped system, using resistive heating of the carbon.

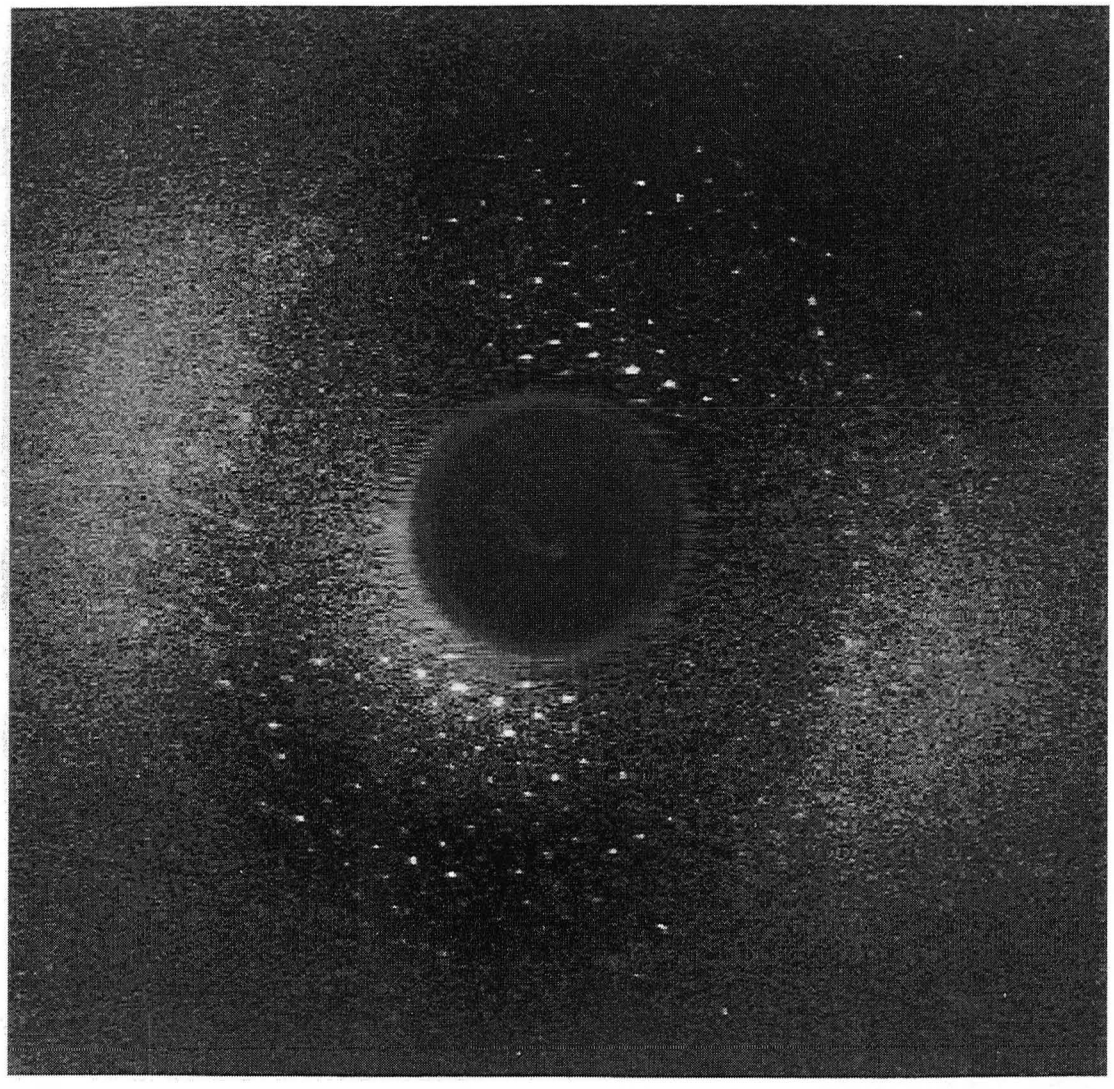

Figure 6-1. An electron diffraction pattern from purple membranes tilted to 45°. Ted-Pella 62-106 carbon and Agar mica was used.

Carbon films made with different starting stock give remarkably better results when tilted. Carbon from Fullam (item number:12020), characterized as spectroscopically pure carbon, actually has the highest level of impurities among the carbon stock materials tried so far. The frequency with which membranes were found, on any one grid, that showed sharp diffraction patterns at high tilt angles, was about two times higher at 45° and three times higher at 30° than specimens prepared on the Heidelberg carbon. Five independent films have been tried so far, and all five carbon films were consistently good. Fig. 6-2 and Fig. 6-3 show diffraction patterns at 45° tilt angle for specimens prepared on Fullam 12020 carbon, using mica from Ted Pella and mica from Agar, respectively. The sharpness of the diffraction spots perpendicular to the tilt axis is greatly improved for both samples, in comparison to the example shown in Fig. 6-1.

The quality of specimens that could be prepared on the Fullam carbon films does change with time of storage after evaporation. It was not uncommon to find that I could no longer make good samples after 1 month. The fact that "good" carbon films have a limited shelf life has been noted previously by Henderson et al. (1990), and we have also found this to be case for the carbon films sent to us from Heidelberg.

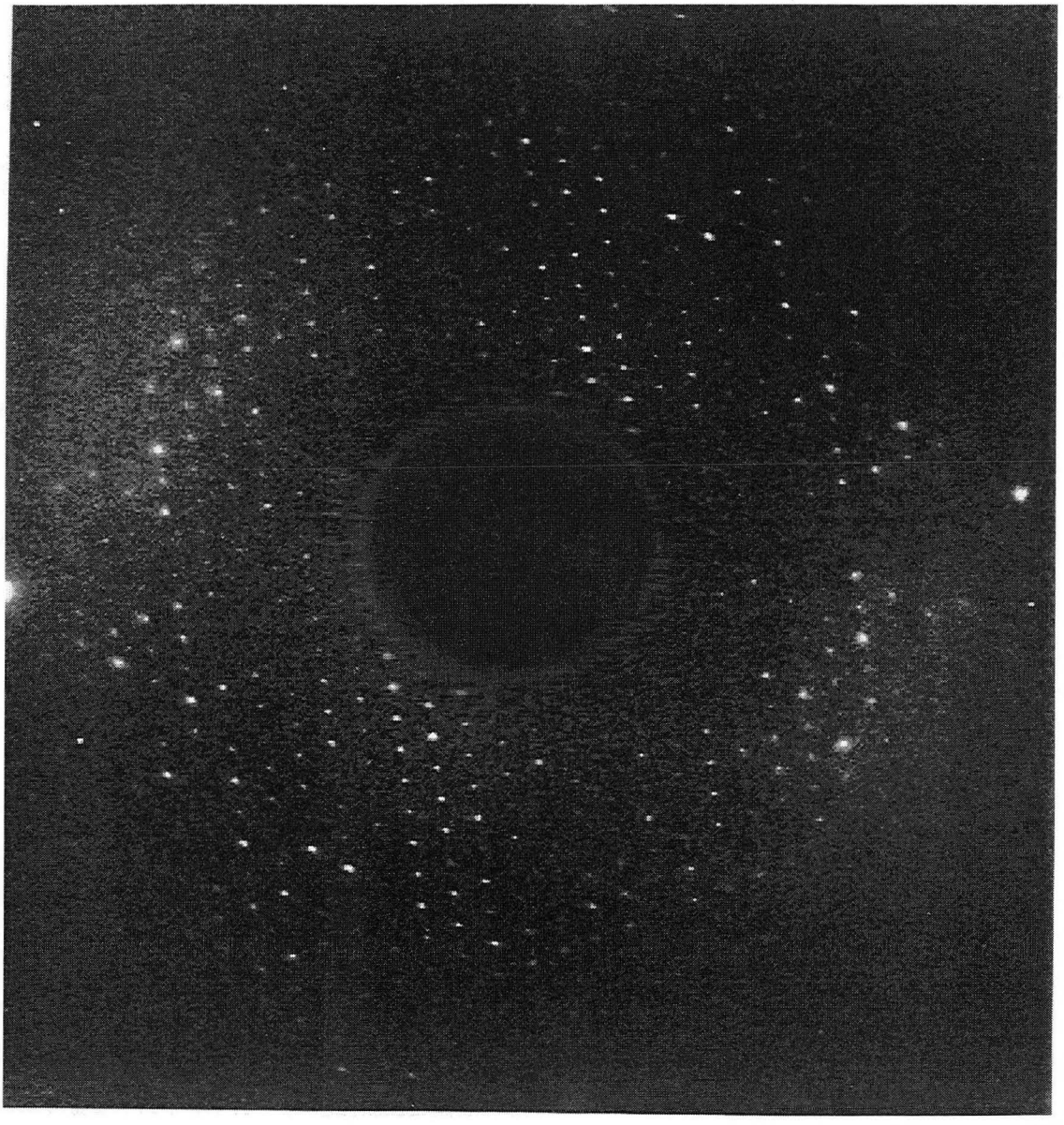

Figure 6-2. An electron diffraction pattern from purple membranes tilted to 45° using Fullam 12020 carbon and Ted-Pella mica.

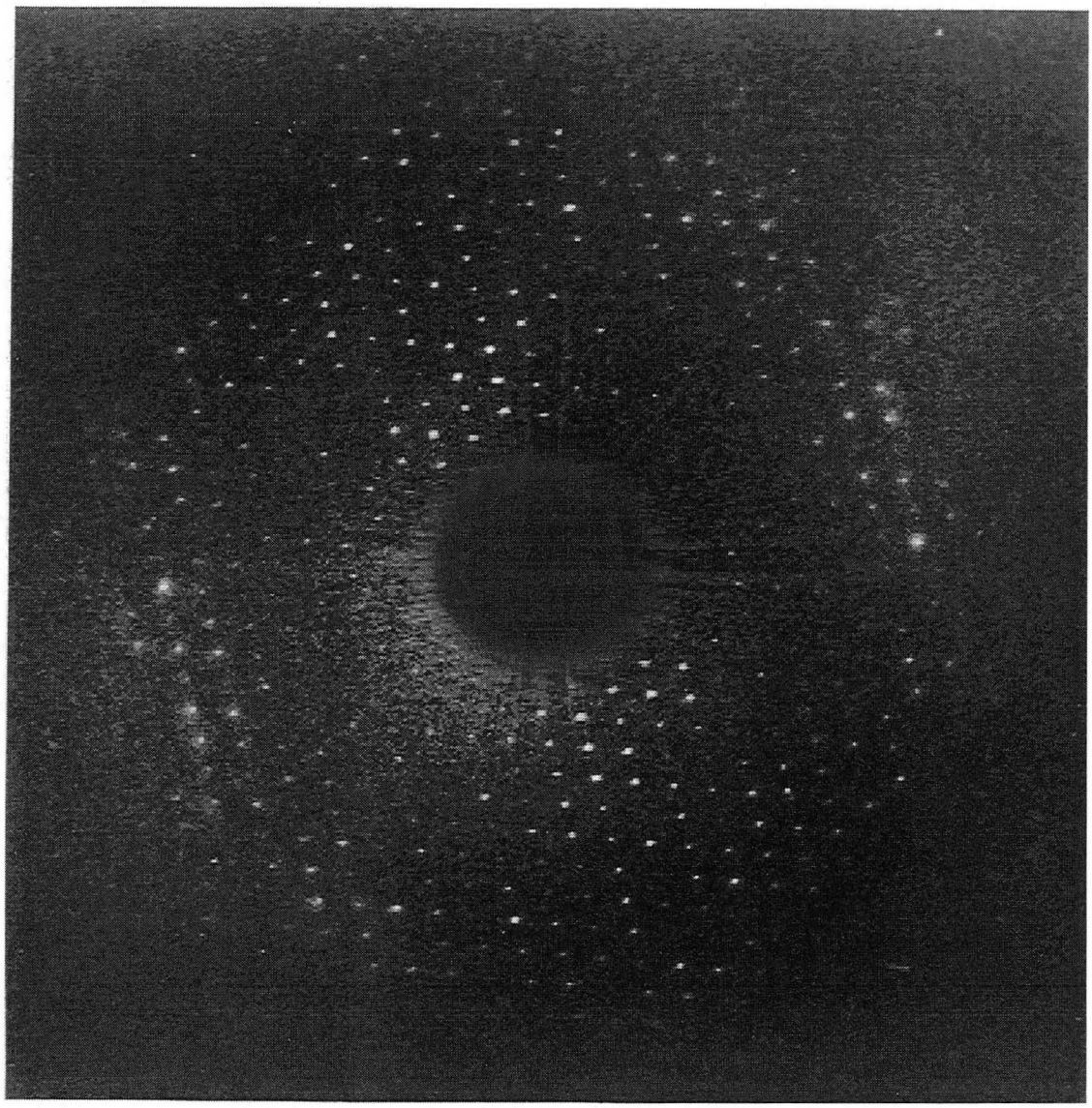

Figure 6-3. An electron diffraction pattern from purple membranes tilted to 45° using Fullam 12020 carbon and Agar mica.

Carbon from Agar (item number:E416), characterized as spectroscopically pure with 20 ppm impurities, also produces quite flat specimens. Four independently made carbon films have been tried from this stock so far, and diffraction patterns at 45° tilt angle were consistently sharp in all four cases.

Carbon from Agar, characterized as spectroscopically pure with 2 ppm impurities, has been tested. This carbon stock is a much softer material than other commercially available carbon, and this softness makes it quite difficult to evaporate the carbon by resistive heating. The one carbon film that we were able to produce from this material resulted in specimens that were not flat enough to give isotropically sharp diffraction patterns at 45° tilt angle.

6.4. Discussion

The type of carbon stock used for evaporation has been found to have a very great influence on specimen flatness of glucose-embedded purple membranes. The starting materials used here have widely different amounts of impurity, ranging from 2 ppm to 1000 ppm. Surprisingly, the residual impurity (ash content) of the starting material does not seem to be an important factor in determining whether a given carbon stock will produce support films that result in flat specimens.

Under the range of the normal laboratory procedures that we use in making evaporated carbon films, specimen flatness is not notably affected by the type of mica used as a substrate, the evaporation vacuum used (0.9×10^{-6} torr vs. 2.0×10^{-6} torr), the evaporation protocol (single, vs. repeated evaporation of successive layers), or even other uncontrolled, day-to-day variations.

We cannot present a physical or chemical explanation of the effect observed with different sources of carbon even though the effect is remarkable. Further characterization of the different carbon surfaces by scanning tunneling microscopy (STM) and by atomic force microscopy (AFM) would be an immediate, next step that could provide further data to understand the observed

differences. STM and AFM images would help to establish whether there is a difference in physical roughness, which correlates with the degree of specimen flatness, as reported by Butt et al. (1991). Other possibilities that would remain, if no difference in roughness can be detected, would be chemical heterogeneity of the carbon surface on a nanometer scale, or other differences in surface chemistry that might affect the stretching (and not infrequent fracture!) of specimens at the last instant of the glucose embedding procedure (Glaeser, 1992).

The important conclusion at this point, however, is that the source of carbon stock should be tested as an experimental variable for any new specimen. We have already found that Fullam 12020 and Agar E416 carbon is much better than Ted-Pella spectrotech 62-106 carbon for preparing 2-D crystals of purple membrane. It would be unjustified at this point, however, to suppose that all types of biological specimens will behave the same way, on any one carbon film.

Chapter 7: A PRELIMINARY THREE-DIMENSIONAL DIFFERENCE MAP OF THE M_{240K} INTERMEDIATE

7.1 Introduction

The high signal-to-noise ratio that I was able to obtain in visualizing structural changes in the formation of the M substates indicates that it is justified to continue these electron diffraction measurements in three dimensions. M_{240K} specimens appear to contain a unique M-substate and are suitable for use in determining 3-D difference maps of this conformational intermediate (Han et al., 1994a).

Our diffraction data from untilted samples also demonstrated that another M-state conformational change occurs after formation of the M_{240K} structures, and this is likely to be similar to the M_N state formed by the D96N mutant. However, the fact that our M_{260K} sample is a mixture of two conformational states makes it less suitable for use in obtaining a 3-D difference map. The use of an appropriate mutant, such as the D96G mutant (Subramaniam et al., 1992), would seem to be a better way to get the 3-D difference map of the M_N intermediate.

7.2 Data collection and refinement

As an intermediate step for the collection of a full 3-dimensional data set, diffraction patterns were recorded at 30° tilt, using Fullam 12020 carbon film which has been shown to produce flat specimens (Han et al., 1994b). One example of the type of diffraction pattern obtained at 30° tilt angle is shown in Fig. 7-1. The diffraction patterns extend almost equally well in all directions, as far as resolution and sharpness is concerned.

Initially, specimen tilt angles, tilt axes, temperature factors, scale factors and twin proportions were calculated by fitting the processed amplitude data to the preexisting reciprocal lattice curves from glucose-embedded purple membranes (Henderson et al., 1990).

Our new method of preparing hydrated, glucose-embedded samples is expected to introduce a significant change in the diffraction amplitudes from Henderson's data, first due to hydration effects for all samples and second due to the conformational changes introduced by the formation of the M intermediate for the M_{240K} data set (Fig. 5-1). These changes in diffraction amplitude make it

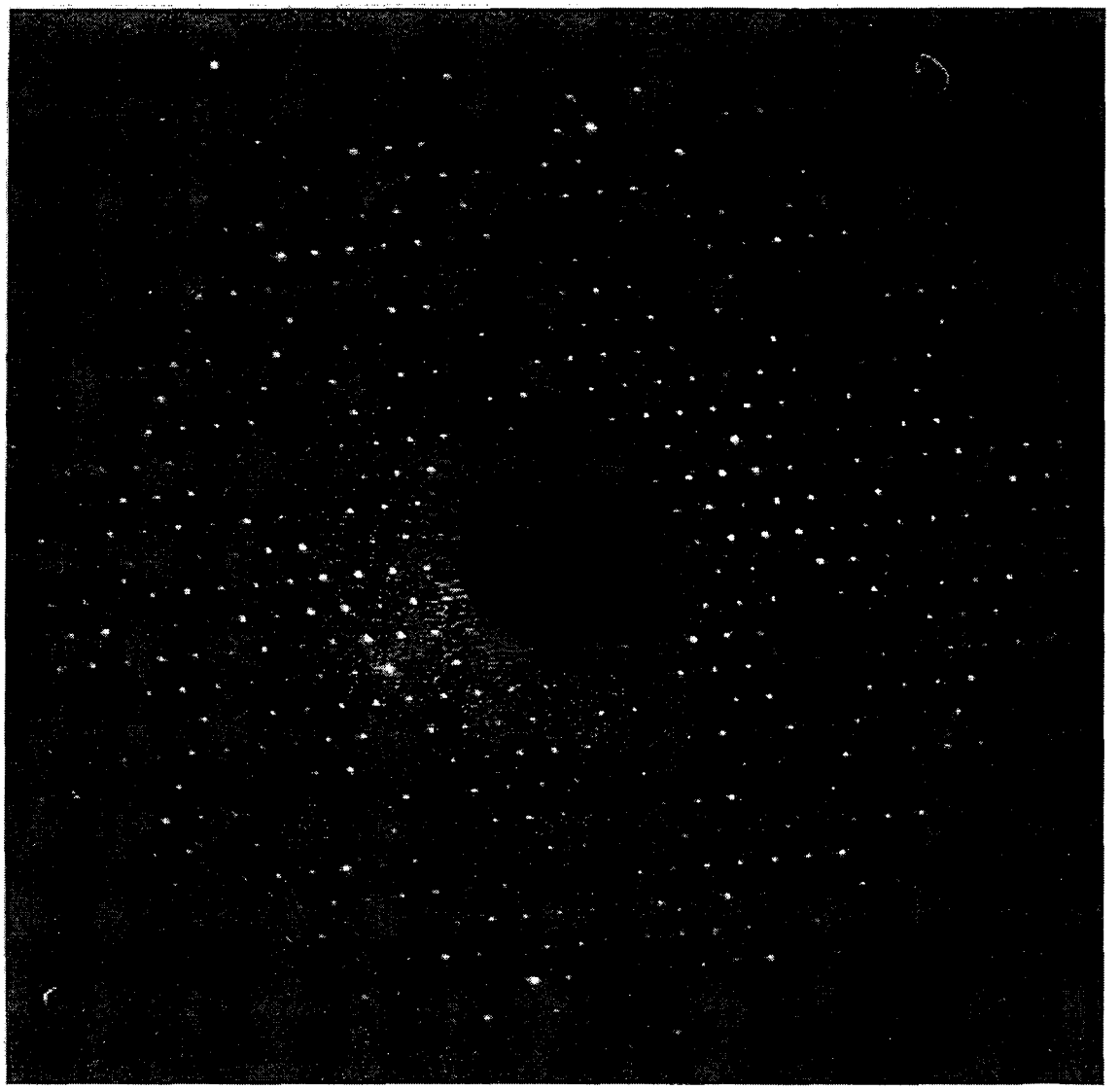

Figure 7-1. An electron diffraction pattern from purple membranes tilted to 30°. The sample is in the M_{240K} state. Fullam 12020 carbon and Agar mica was used.

sensible to recalculate the reciprocal lattice curves for the bR_{240K} and parameters, mentioned in the paragraph above, for each cycle. The untilted amplitude data were not used during the first 5 cycles of iterative refinement. The new curves obtained at the end of one cycle were used to fit the amplitude data in the next refinement cycle. After five iterations, the diffraction data from untilted samples were added and the whole data set was refined for additional five steps. These refinement steps were followed independently for the bR_{240K} and the M_{240K} data.

The discrepancy between the measured diffraction intensities and the refined curves was evaluated from the value of Rmerge (Baldwin and Henderson, 1984), defined as:

$$\text{Rmerge} = \frac{\sum |I_{obs} - I_{curve}|}{\sum I_{curve}}.$$

In order to eliminate bias in this evaluation, three tilted diffraction patterns and three untilted diffraction patterns were kept out of the refinement process. These 3 diffraction patterns were then merged to the refined curves, and Rmerge values were calculated for the data in the three films. These Rmerge values are referred to as the "free Rmerge" values following the terminology of Brünger (1992).

The calculated average values of free Rmerge are shown in Figure 7-2. The X-axis represents the number of refinement cycles, while the Y-axis represents the average of the three free Rmerge values for the tilted and untilted diffraction patterns, respectively. In the 0-th cycle, the diffraction amplitude data were merged to the preexisting reciprocal lattice curves from Henderson et al. (1990). During the next 10 cycles of refinement, the diffraction amplitude data were merged to the new, refined lattice curves. The average free Rmerge for the tilted data was 0.222 when data were merged to the curves from Henderson et al. (1990). After just one refinement step, the free Rmerge for the tilted data dropped to 0.116. In the next 9 refinement cycles, the free Rmerge did not change much. The average free Rmerge for the untilted data started at 0.193, dropped to 0.175 after the first cycle, and stayed almost uniform up to the 5-th cycle. At the 6-th cycle, in which 11 untilted diffraction patterns were included in the refinement, the free Rmerge dropped to 0.116 and stayed almost constant in later refinement cycles.

It is interesting that the free Rmerge values decrease quite significantly after refinement. This result shows that it is worthwhile to make our own lattice line curves. The improved free Rmerge values are probably due in part to the fact that the hydration technique used in our specimen preparation ensures more reproducible diffraction data of bR than the conventional

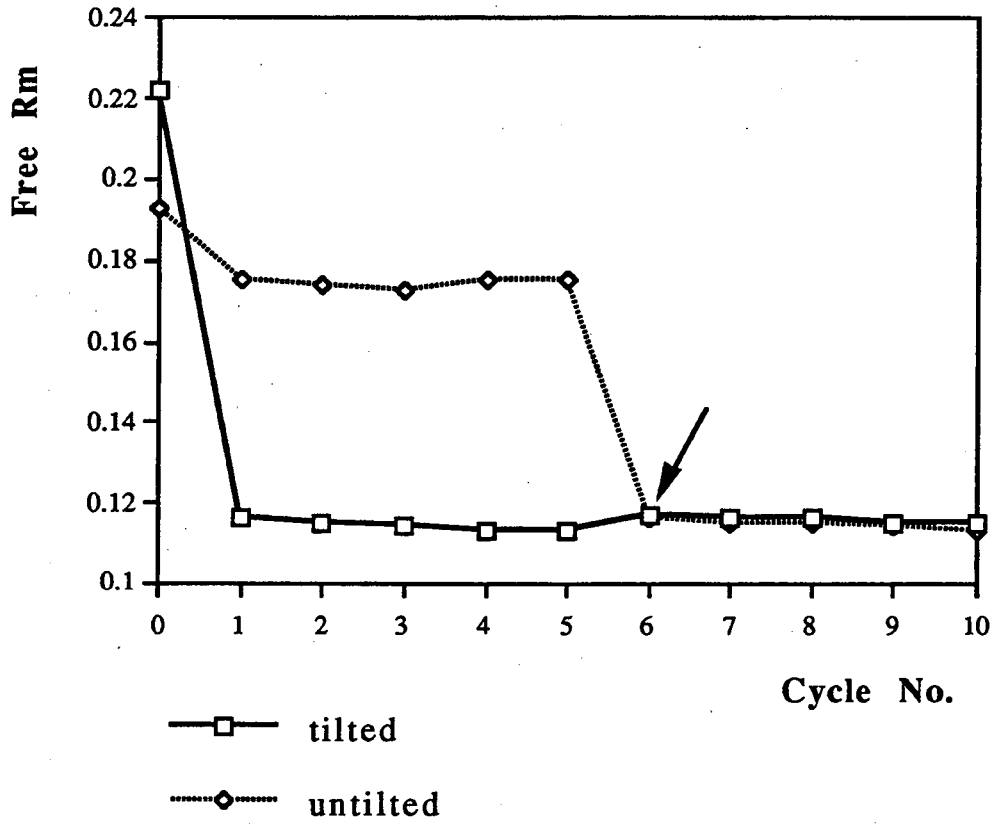

Figure 7-2. Free Rmerge values for refined lattice curves for bR_{240K} data set. In 0-th cycle, the data were merged to Henderson's data set (1990). From the 6-th cycle, designated by an arrow, untilted diffraction data were also included in the refinement cycles. The squares represent free Rmerge values for tilted diffraction patterns and the diamonds represent the free Rmerge values for untilted diffraction patterns.

glucose embedding technique, as has been shown in Chapter 4, Hydration Effect. The Free Rmerge values for tilted diffraction patterns are similar to the free Rmerge values for untilted diffraction patterns. The improved free Rmerge values for tilted diffraction patterns are partially due to the almost isotropic diffraction patterns (Fig. 7-1), that were obtained by using good carbon films, as has been described in Chapter 6, Preparation of Flat Specimens.

One useful indication of the consistency of the data is to compare Rmerge with Rsym. Rsym represents the intensity difference between Friedel-related partners and can be expressed in the mathematical form:

$$Rsym = \frac{\sum |I_1 - I_2|}{\sum \frac{(I_1+I_2)}{2}}.$$

While Rmerge compares each film to the combined data from all films, Rsym measures the experimental discrepancy between pairs of intensity values, on the same film, which are expected to be identical. Figure 7-3 (a) shows a plot of Rmerge versus Rsym for all 85 diffraction patterns when they were first merged with Henderson's lattice curves. Each circle represents one film. Films which are the most different from the average will have the highest values of Rmerge, and will therefore show up at points that are

(a)

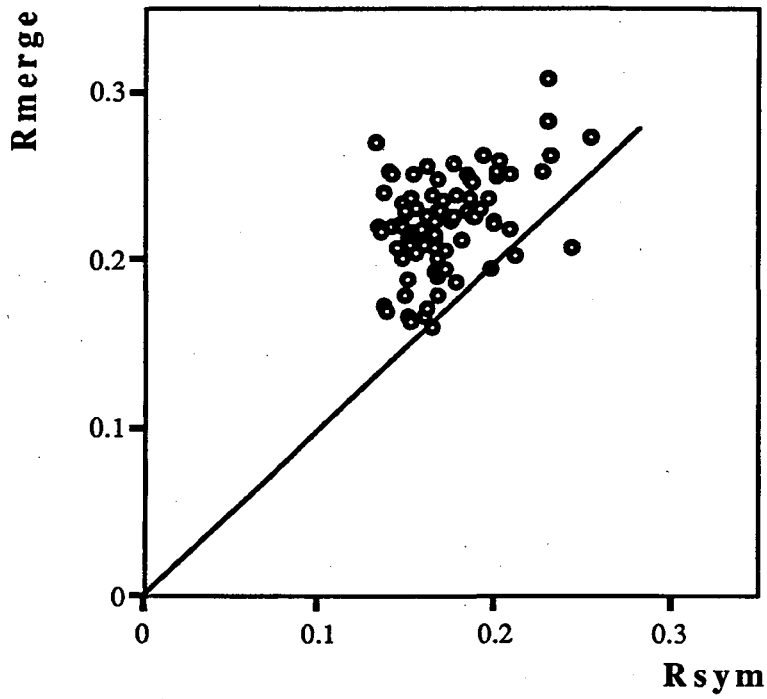

(b)

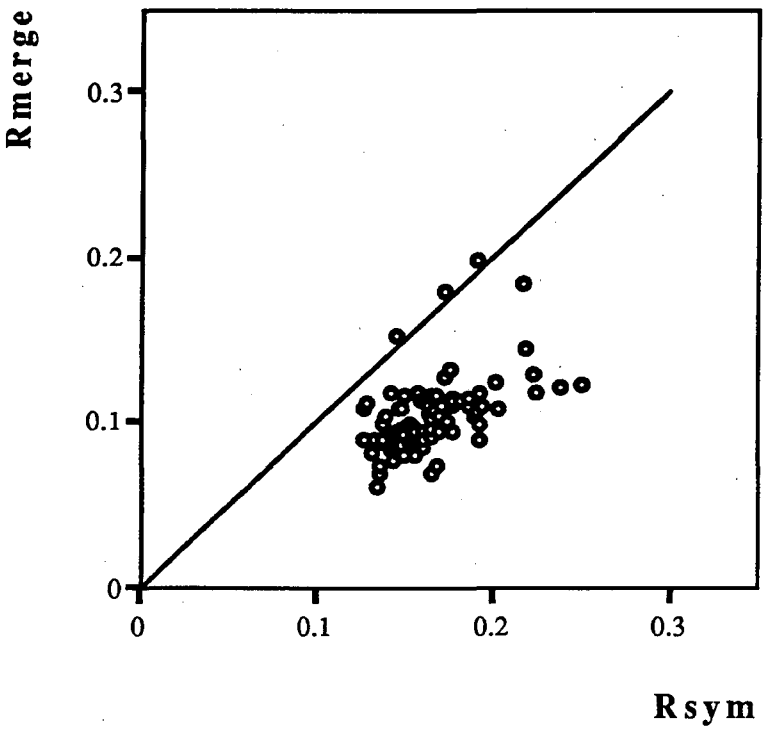

Figure 7-3. Rmerge versus Rsym. Each circle corresponds to one diffraction pattern. A total of 85 diffraction patterns are included. The reference line has slope=1.0. (a) Rmerge versus Rsym values are calculated for the diffraction data when they were first merged to the lattice curves from Henderson et al. (1990). (b) Rmerge values were calculated for the new, refined lattice curves.

farthest above the line of slope=1.0. At this initial stage, almost all diffraction patterns appear above the line of slope=1.0 and the average slope is about 1.3. Figure 7-3 (b) shows Rmerge versus Rsym after refinement. Almost all films are now below the line of slope=1.0 and the average slope is about 0.65, which is much smaller than the slope 1.5 reported by Baldwin and Henderson (1984), reflecting the improvement of data quality in terms of better sample preservation (Chapter 4: Hydration Effect) and flatter specimens (Chapter 5. Preparation of Flat Specimens).

It is quite interesting that Rmerge values in my data set can even be smaller than Rsym values. Rmerge values have been expected to be larger than Rsym values in the sense that Rmerge values reflect not only counting error, as Rsym values do, but also other sources of error due to possible variations in: radiation damage, flatness of different membranes, depth of embedding in glucose, cell dimension changes due to slight changes in lipid proportion, and possible squashing of the protein against the carbon support film, as described by Baldwin and Henderson (1984). My experimental data, showing Rmerge values smaller than Rsym values, may be explained by the following two arguments. In the ideal case of well prepared samples with minimal sample to sample variations, the counting statistics can explain why Rmerge values should be smaller than Rsym values. If σ is the error due just to

counting statistics for one diffraction spot, then the error in comparing two diffraction spots that are expected to have the same intensity (i.e. to get Rsym) will be

$$\sqrt{\sigma_1^2 + \sigma_2^2} = \sqrt{2}\,\sigma$$

If two equivalent diffraction spots are averaged, however, the counting statistics are improved, and the error is reduced to $\sigma/\sqrt{2}$. When this averaged value is compared to an error-free curve (to get Rmerge), the error remains $\sigma/\sqrt{2}$. Qualitatively, it follows that

$$\frac{\text{Rsym}}{\text{Rmerge}} = \frac{\sqrt{2}\,\sigma}{\sigma/\sqrt{2}} = 2 .$$

On the basis of this argument, the expected slope of Rmerge versus Rsym in Figure 7-3 would be 0.5. This theoretical value is more than enough to explain why my data show a slope of 0.65. Another factor that may play a role is related to the dynamic scattering effect. By averaging Friedel pairs in calculating Rmerge, the intrinsic difference between Friedel mates that is due to dynamic scattering can be canceled to first order (Glaeser and Downing, 1993), and this fact will also decrease Rmerge compared to Rsym.

Two examples of refined bR_{240K} lattice curves, obtained after 10 cycles of refinement, are shown in Fig. 7-4. The horizontal axis

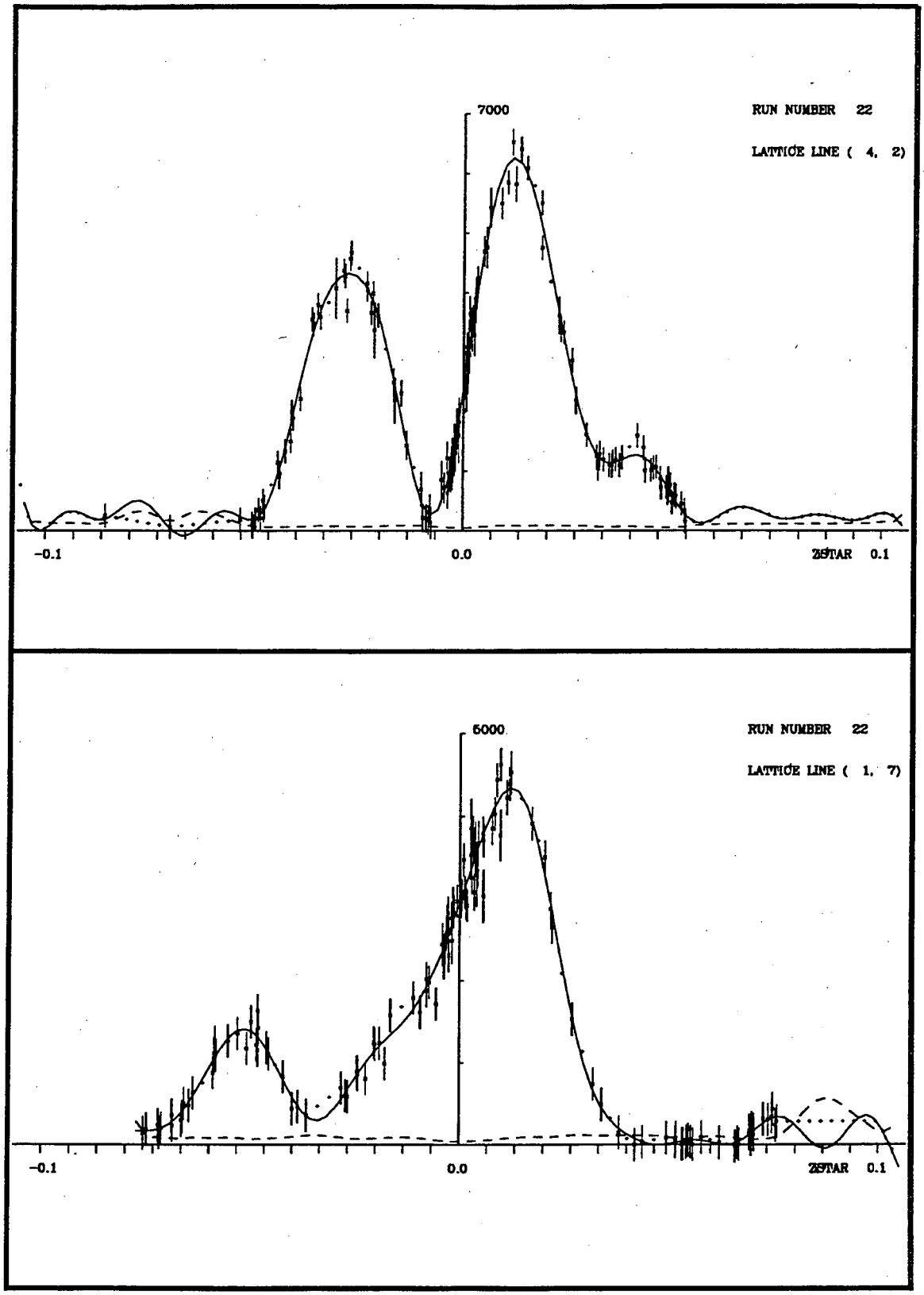
7000
RUN NUMBER 22
LATTICE LINE (4, 2)
-0.1
0.0
2STAR 0.1
6000
RUN NUMBER 22
LATTICE LINE (1, 7)
-0.1
0.0
2STAR 0.1

Figure 7-4. Two examples of the merged electron diffraction data for the refined bR_{240K} lattice curves. A total of 31, 30°-tilted diffraction patterns and 14 untilted diffraction patterns were used. The continuous curves shown are the best fit to the experimental data. The dashed curve near the baseline is the root mean square error in the fitted curve.

represents the z^* axis along the lattice lines (4,2) and (1,7) in reciprocal space. The vertical axis represents diffraction intensity. The continuous curves are the best fit to the experimental data and the dashed curves are the estimated rms error obtained from the fitting procedure. The small bars across the lattice curves are the experimental difference between Friedel mates. A total of 31, 30° tilted diffraction patterns and 14 untilted diffraction patterns have been included for these curves. Since 45 diffraction patterns were used to make these curves, each lattice line has 110-130 spots.

7.3 Three-Dimensional Difference Fourier map

Refined amplitude data sets for the data obtained at 30° tilt angles were combined with experimental phases (Henderson et al., 1990) to produce a three-dimensional difference Fourier map. To visualize the three dimensional conformational changes, the difference Fourier map is displayed as a series of two-dimensional sections. The whole difference Fourier map, sectioned at 2.8 Å intervals in the z-direction, is shown in Appendix A.

The average modulus within each section was plotted against the spatial position along the z axis, and the result is shown as a solid line in Figure 7-5. The fact that the average modulus increased significantly within the envelope of the membrane can be taken as good evidence that there is real signal contained in the measured difference amplitudes. However I wanted to be sure that the increase in modulus in the region of the protein was not an artifact. It might be argued, for example, that the phases are biasing the power to be localized within the membrane even when the power is completely due to noise. To test this possibility I used a set of random difference amplitudes, which had the same average and variance as the experimental values, and which were generated from a Gaussian distribution function. These random difference

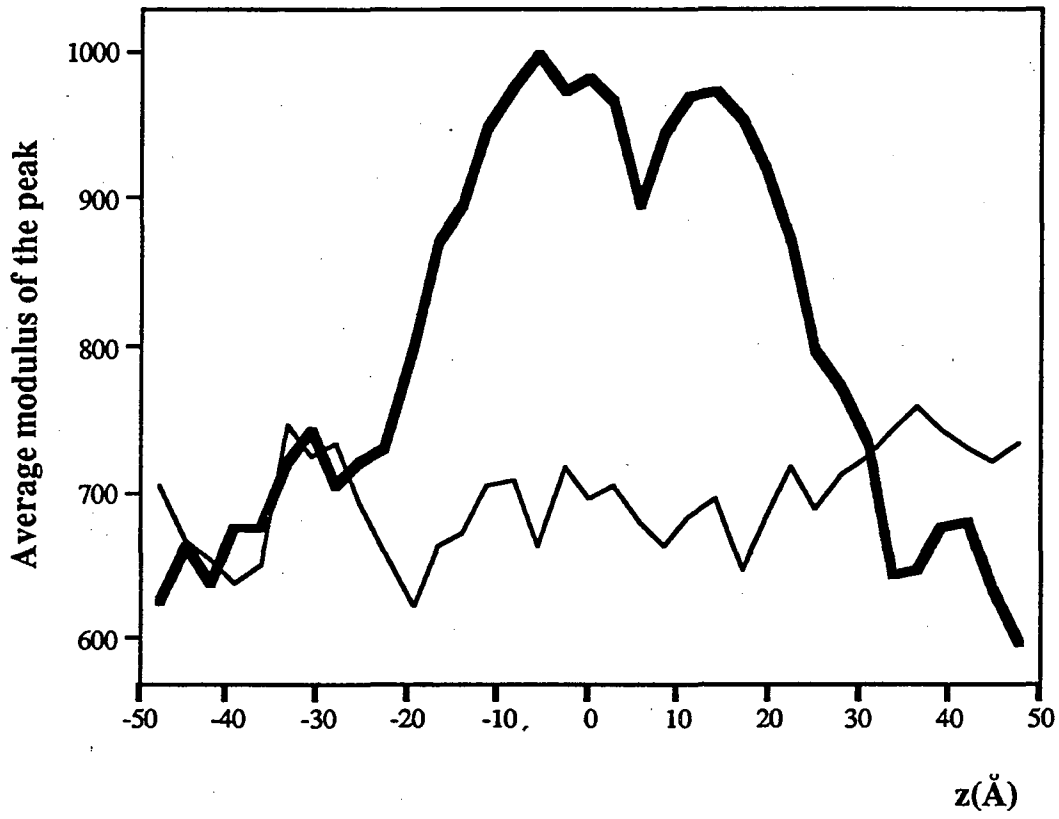
Average modulus of the peak
1000
900
800
700
600
-50
-40
-30
-20
-10
0
10
20
30
40
50
z(Å)

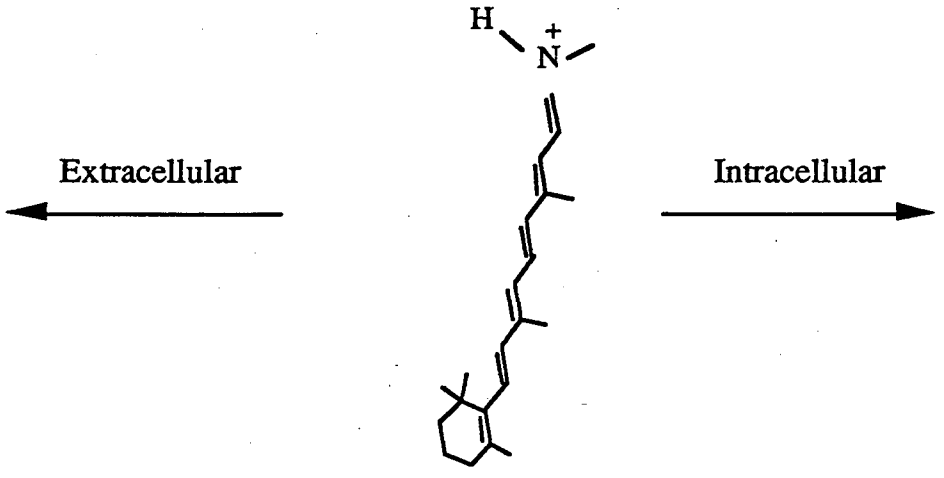
H
N
+
Extracellular
Intracellular

Figure 7-5. Distribution of the average modulus in successive planes of the difference Fourier map, plotted as a function along the z axis. The solid line shows the real experimental map while the thin line shows the map produced with a random distribution of difference amplitudes. As a guide, the approximate position of the retinal molecule is shown by the molecular diagram.

amplitudes were combined with the experimental phases to generate a series of 2-dimensional sections in real space as in the case of the experimental difference map. The average modulus of this noise map along the z axis is shown as the thin line in Figure 7-5. A cartoon showing the z-position of the atoms of retinal is drawn at the bottom, as a reference. The protein chain is confined within about ±25 Å, and this figure shows clearly that the major peaks in the M-bR difference Fourier map are also confined within the protein boundary, while the average modulus of the noise map is completely spread out along the z axis demonstrating that the experimental data are not just random noise.

The missing data extend from 30° to 90° in my preliminary data set, and this is expected to cause a loss in resolution in the vertical direction, as has been discussed in Chapter 2, Theoretical and Technical Aspects of Electron Crystallography. The amount of decrease in resolution can be described quantitatively by a point spread function. The theoretical point spread functions for three incomplete data sets are shown in Figure 7-6, for 60°, 45° and 30° tilt angles, respectively. Continuous lines represent the value of the point spread functions along the x axis, while discontinuous lines represent the value of the degraded point spread functions, in the z direction, i.e. the direction of the missing data. These curves were calculated by Dr. Kenneth Downing (unpublished). For the 30° data

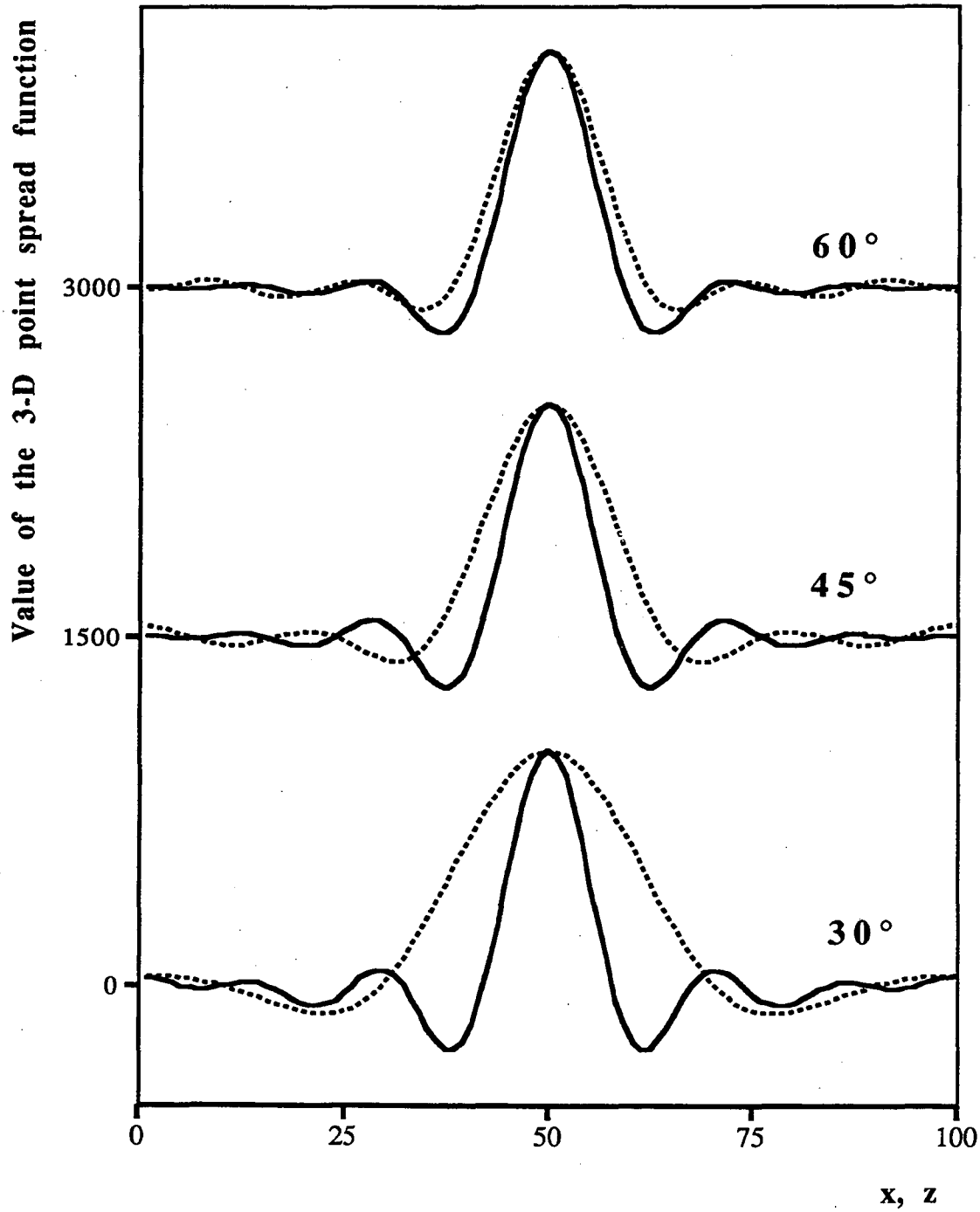
Value of the 3-D point spread function
3000
1500
0
60°
45°
30°
0
25
50
75
100
x, z

Figure 7-6. The point spread function in real space which corresponds to the Fourier transform of an "aperture function" in reciprocal space. The point spread function is represented as line drawings for 30°, 45° and 60° tilted data, respectively. The calculations have been generously provided by Dr. K. H. Downing.

set, the point spread function is elongated by a factor of ~2.4 in the direction of the missing data. This will degrade the resolution of the map from a value of 3.5 Å along the x axis to a value of 8.4 Å along the z axis.

The experimental difference amplitudes have also been combined with phases calculated from the atomic model structure of bR to generate a 3-D difference map. Four examples of sections within the difference Fourier map are shown in Fig. 7-7 to 7-10. All three figures are contoured at the same contour levels. Figure 7-7 shows a section outside the protein boundary and all peaks are lower than three contour levels.

Figure 7-8 shows a section located 8 Å from the center, which contains the Schiff base. The position of the Schiff base in the bR atomic model structure is designated by an arrow. There exists one negative peak close to the position of the Schiff base which deprotonates during the formation of the M intermediate. The negative peak around the Schiff base has three contour levels and is coupled with 2 positive peaks. This may suggest the displacement of the Schiff base, the loss of the positive Coulomb potential due to the deprotonation, or both of these. There is one big negative peak at the position of phenylalanine 88 and one positive peak close to the

negative peak, coupled as a dipole suggesting the possibility of lateral movement.

Figure 7-9 shows a section located 3 Å from the center and this section contains aspartate 85, which protonates during the formation of the M intermediate. The positive peak on the position of the aspartate is not coupled with a negative peak, suggesting the gain of positive potential due to the protonation from the Schiff base or the existence of a more ordered structure after the protonation, or both of these.

Figure 7-10 shows the central section, which contains the ionone ring of the retinal, designated by an arrow. One clear result shown in this map is that there is only one very weak negative peak near the ionone ring in the range of noise. This shows that the ionone ring does not go through any significant displacement during the formation of the M intermediate.

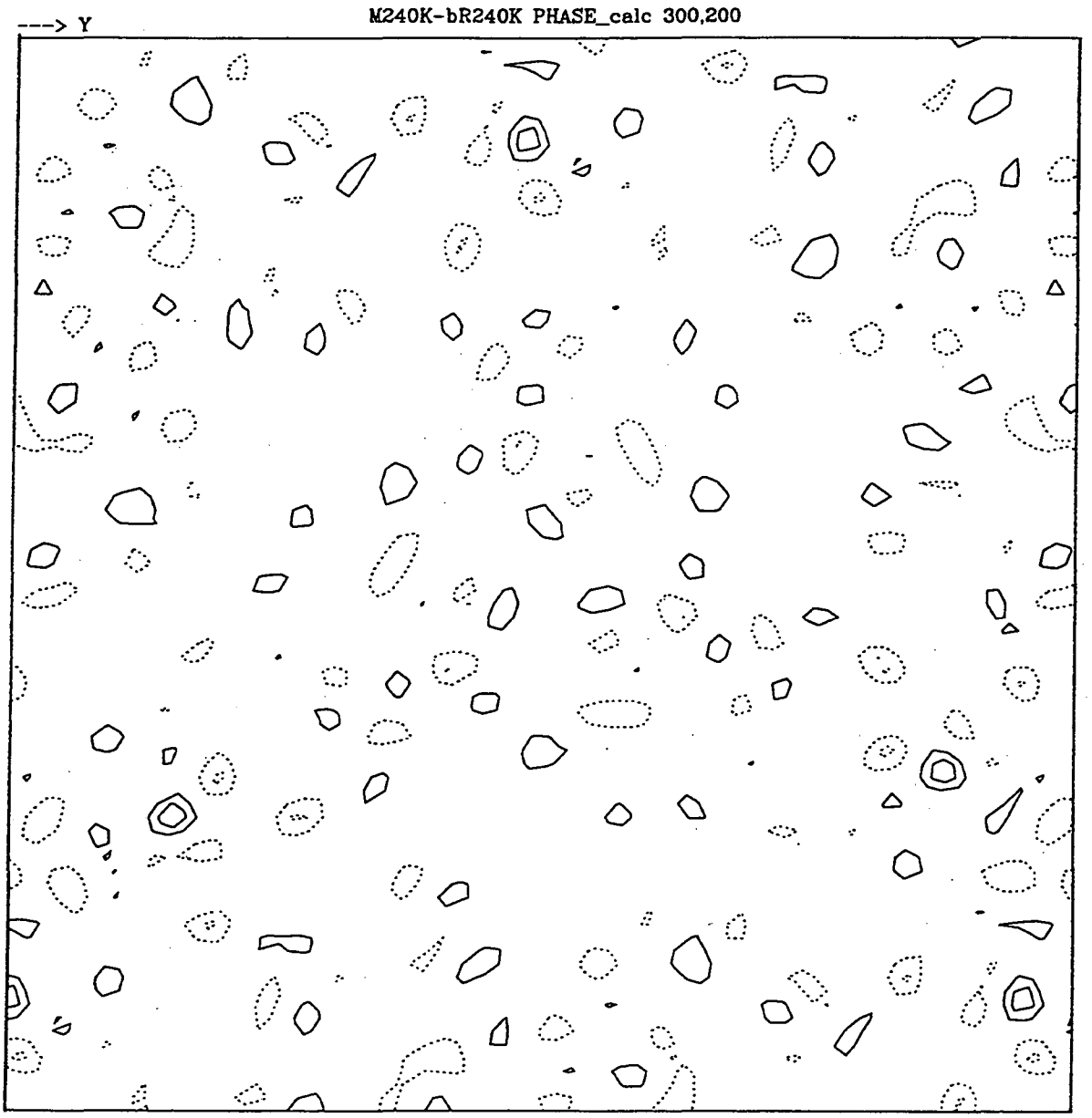
---> Y
M240K-bR240K PHASE_calc 300,200
Scale = 5.0000 mm/A
Section -17
3.5A

Figure 7-7. A section of the M_{240K} minus bR_{240K} difference Fourier map. This figure is a section through a plane -48 Å from the center (Fig. 7-5). The map was contoured from 300 at an interval of 200. The continuous lines represent positive signals and the discontinuous lines represent negative signals.

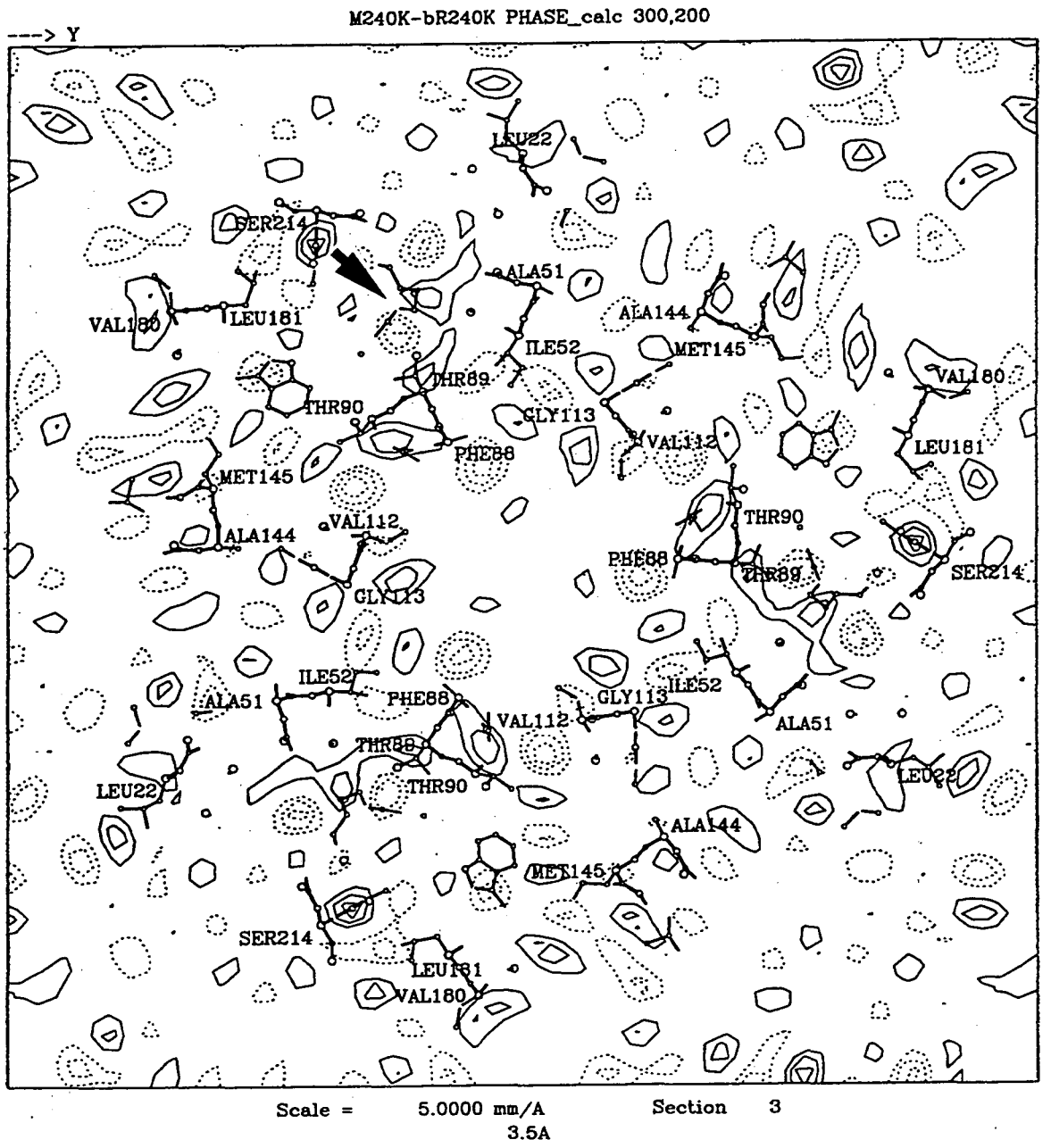
M240K-bR240K PHASE_calc 300,200
---> Y
LEU22
SER214
ALA51
VAL180
LEU181
ILE52
ALA144
MET145
THR89
VAL180
THR90
GLY113
VAL112
PHE88
LEU181
MET145
THR90
VAL112
ALA144
PHE88
THR89
SER214
GLY113
ILE52
ILE52
ALA51
PHE88
GLY113
VAL112
ALA51
THR89
LEU22
LEU22
THR90
ALA144
MET145
SER214
LEU181
VAL180
Scale = 5.0000 mm/A
3.5A
Section 3

Figure 7-8. A section of the M_{240K} minus bR_{240K} difference Fourier map. This figure is a section through a plane 8 Å from the center (Fig. 7-5). As a reference, the atomic model structure from Henderson et al. (1990) is superimposed. The position of the Schiff base is specified by an arrow.

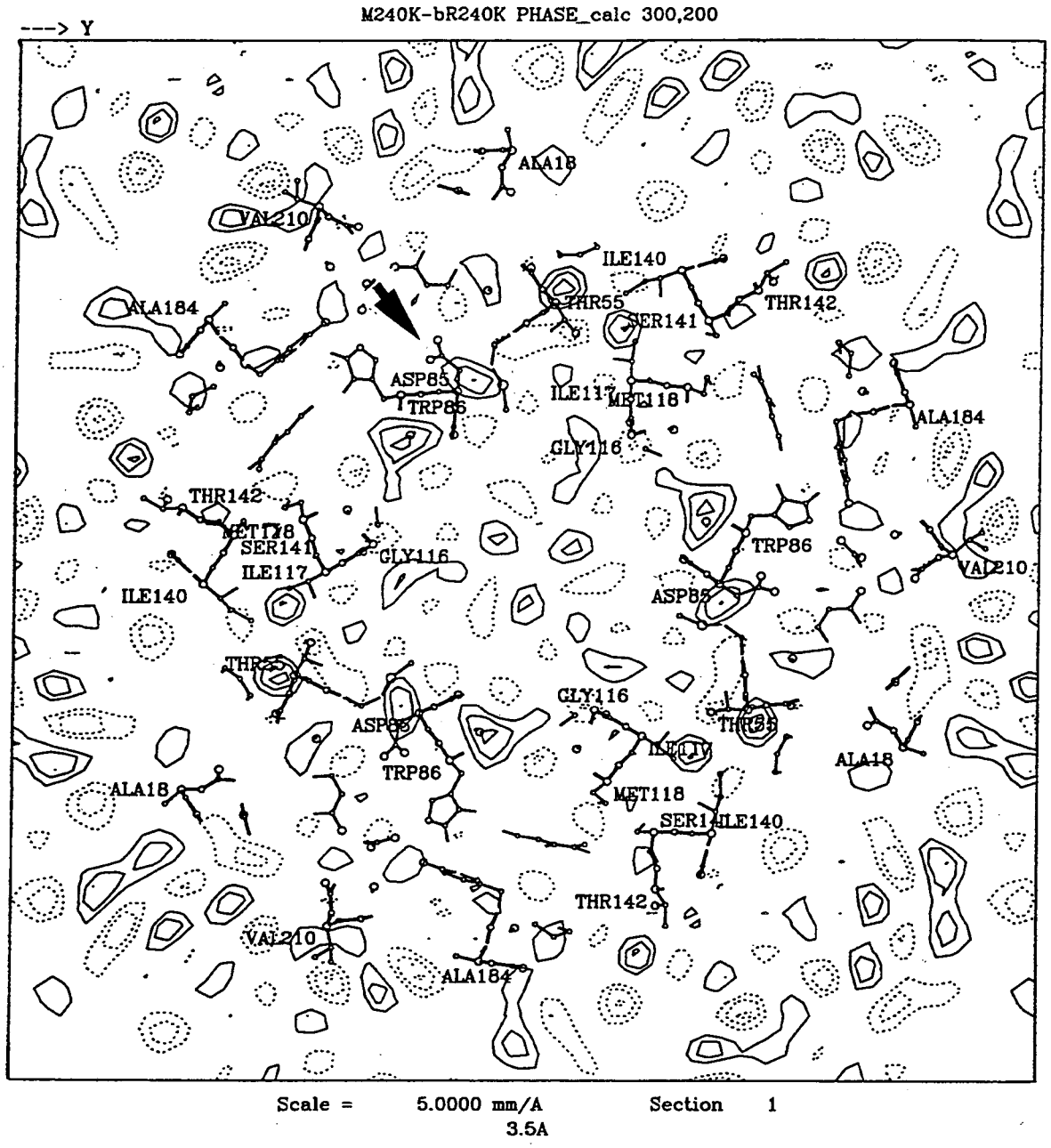

Figure 7-9. A section of the M_{240K} minus bR_{240K} difference Fourier map. This figure is a section through a plane located 3 Å from the center (Fig. 7-5). The position of the aspartate-85 is specified by an arrow.

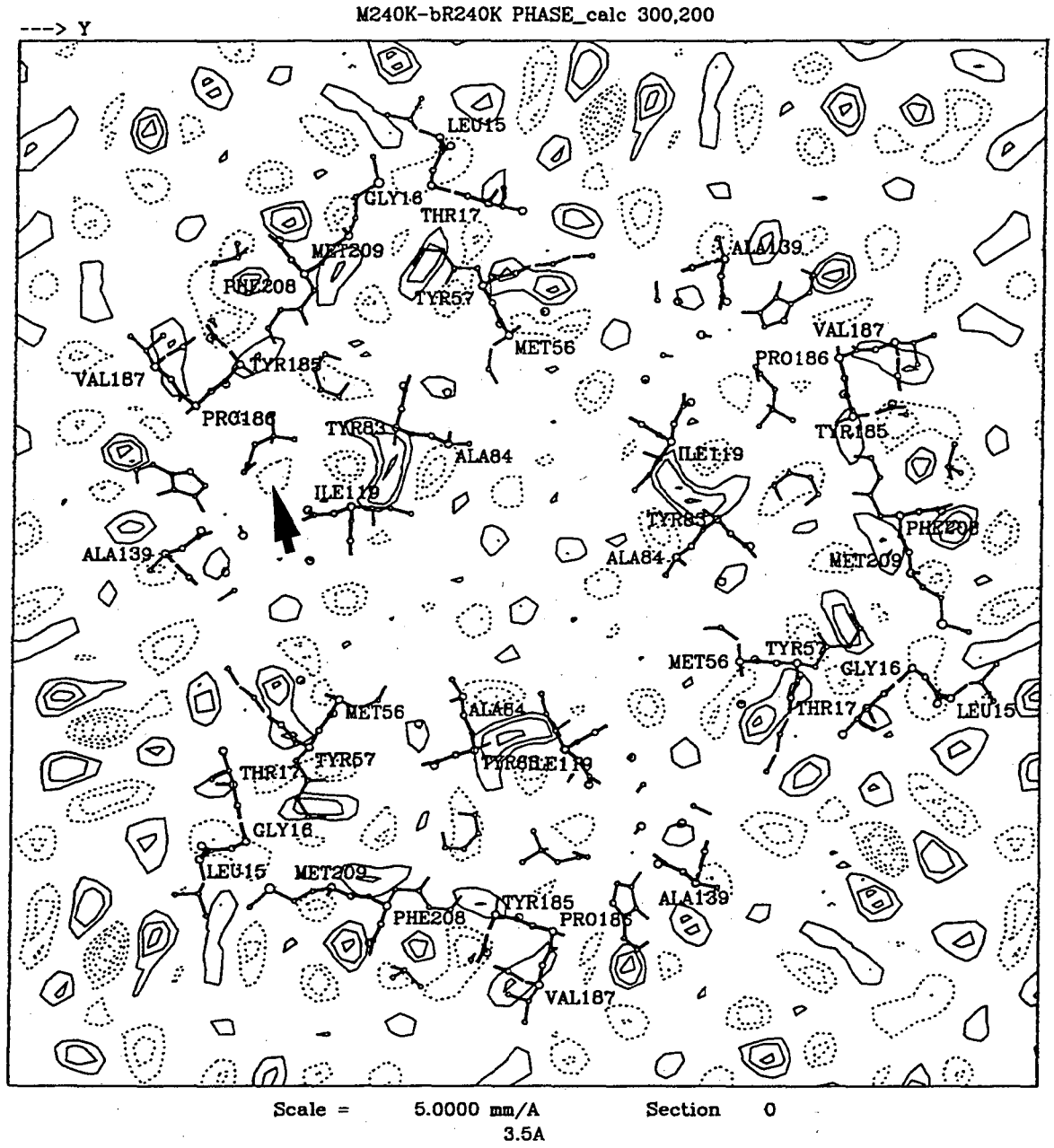

Figure 7-10. A section of the M_{240K} minus bR_{240K} difference Fourier map. This figure is a section through a plane at the center (Fig. 7-5). The position of the ionone ring is specified by an arrow.

7.4 Discussion

Our new sample preparation techniques improved the diffraction data quality significantly at high tilt angles, both in terms of better preservation of samples (Chapter 4; Han et al., 1994a) and in terms of flatter specimens (Chapter 6; Han et al., 1994b). From these improvements, I could easily obtain high quality diffraction data to 30° tilt angles. These diffraction data merged to produce the reciprocal lattice line curves that were much better than the conventional diffraction data, enabling us to measure small amplitude changes caused by the formation of the M intermediate.

Even at this preliminary stage of producing a 3-D map, a number of conclusions can be drawn about the overall nature of the conformational change that occurs during the formation of the M intermediate. Above all, large scale conformational changes, such as the movement of a helix, do not occur during the formation of the M240K intermediate (Han et al., 1994c). Previously, several groups suggested that a 3-dimensional conformational change would be larger than what we have found. Draheim and Cassim (1985) reported the net tilting of the protein polypeptide chain, based upon circular dichroism spectroscopy of oriented films. Wan et al. (1993)

reported that reorientational motion of bR monomers occurs, as detected by the use of linear dichroism spectroscopy. Using electron diffraction data from crystals tilted by only 10°, Subramaniam et al. (1993) suggested that there might be a selective opening of the cytoplasmic half of the channel, which would require some tilting of helices. These differences between our experiment and that of Subramaniam now can be explained in terms of different proportions of the M and M_N intermediates, however (Sasaki et al., 1992; Perkins et al., 1992; Han et al., 1994a; Vonck et al., 1994).

We think that our M intermediate is different from Subramaniam's (1993). Sasaki et al. (1992) recently showed the existence of an intermediate (which they called M_N) with the protein structure of N but a deprotonated Schiff base indicative of M. This intermediate was trapped in the D96N mutant (which lacks the aspartate group that reprotonates the Schiff base in the M to N step), at high pH (to prevent Schiff base reprotonation from the medium). Apparently the protein structural change giving rise to the N intermediate had taken place in this sample, but due to lack of a proton to reprotonate the Schiff base, the retinal remained in the deprotonated configuration specific for M. Although Subramaniam did not use spectroscopy to characterize the exact nature of the M intermediate trapped in this mutant protein, it is most likely that he has trapped predominantly M_N, because reprotonation of the Schiff

base is blocked by removal of the proton donor, aspartate 96. It is more likely that there will be helix tilts or bends in N (or M_N), and Subramaniam may have already seen this.

The difference in the amount of conformational changes between M_{240K} and M_N may be explained mechanistically. The idea that active transport (and exchange transport) membrane proteins should cycle between an inward facing and an outward facing conformation is well-established (Stoeckenius, 1979; Nagle and Mille, 1981; Chou, 1993, Vonck et al., 1994). It is most likely that the outward facing channel closes just before the M_{240K} intermediate is formed, and the inward facing channel opens when the M_{240K} intermediate converts to the M_N intermediate. It is expected that there should be a large conformational change required to open the quite long, hydrophobic, inward facing channel during the formation of M_N. On the contrary, just a slight change in orientation of the Schiff base nitrogen lone pair from a direction facing the hydrophilic channel to one that faces the hydrophobic environment (Mathies et al., 1991) or removal of one or two water molecules (Chou et al., 1993) will be enough to "close" the outward facing channels.

My preliminary, three-dimensional difference Fourier map shows a clear indication of numerous small, conformational changes,

which may be interpretable in terms of vertical or horizontal movements of amino acid residues. Several important peaks around the Schiff base and the aspartate 85 could be detected. The negative peak near the Schiff base and the positive peak on the aspartate 85 are well correlated with the biochemical fact that a proton moves from the Schiff base to aspartate 85. The map also shows that the ionone ring of the retinal does not move at all during the formation of the M intermediate. Using polarized absorption spectroscopy, Otto and Heyn (1991) showed that the transition dipole moment of retinal moves about 3° toward the outside of the cell during the formation of the M intermediate. The result from polarized absorption spectroscopy suggests that the 13-cis chromophore in the M_{240K} intermediate should be accommodated not by movement of the ionone ring but by the rearrangement of the lysine-216 side chain. This conclusion is strongly supported from my difference map which shows quite strong peaks around lysine-216, but none in the region of the ionone ring.

As shown in Figure 7-6, it will be necessary to increase the tilt angles to 45°, and even further up to 60°, to improve the resolution of the map in the z-direction. The poor resolution in the third dimension, due to the presently missing cone of data of ±60°, makes it rather difficult to assign peaks in the difference Fourier map in terms of vertical or horizontal movements of amino acid residues.

The future for obtaining more highly tilted diffraction data is quite bright, however, in the sense that we can now produce good carbon films consistently.

Many strong negative peaks in my difference Fourier map appear at the place where there are no corresponding amino acid residues in the model structure. This suggests that it will be necessary to refine the atomic model structure of bR before it is possible to make a full interpretation of the difference Fourier map. Of course, the difference Fourier map itself could provide useful information which was not available previously for refining the atomic model structure. The final difference map, constructed by using diffraction amplitude data at 45° tilt angles and phases from the refined atomic model structure, will help us understand the structural basis for the proton pumping mechanism in bR at atomic resolution.

Appendix A: A three dimensional M_{240K} minus bR_{240K} difference Fourier map

This difference Fourier map was prepared from untilted and 30° tilted diffraction data sets. The difference amplitude data were combined with phases calculated from the atomic model (Henderson et al., 1990). The map was contoured from 300 with intervals of 200. The continuous lines represent positive peaks and the discontinuous lines represent negative peaks. The positions of the amino residues were obtained from the atomic model (Henderson et al., 1990). The whole map was sectioned in 2.8 Å intervals along the z axis. The relative position of the retinal is shown in Figure 7-5. The positive values along the z-axis represent the cytoplasmic domain while the negative values represent the extracellular domain.

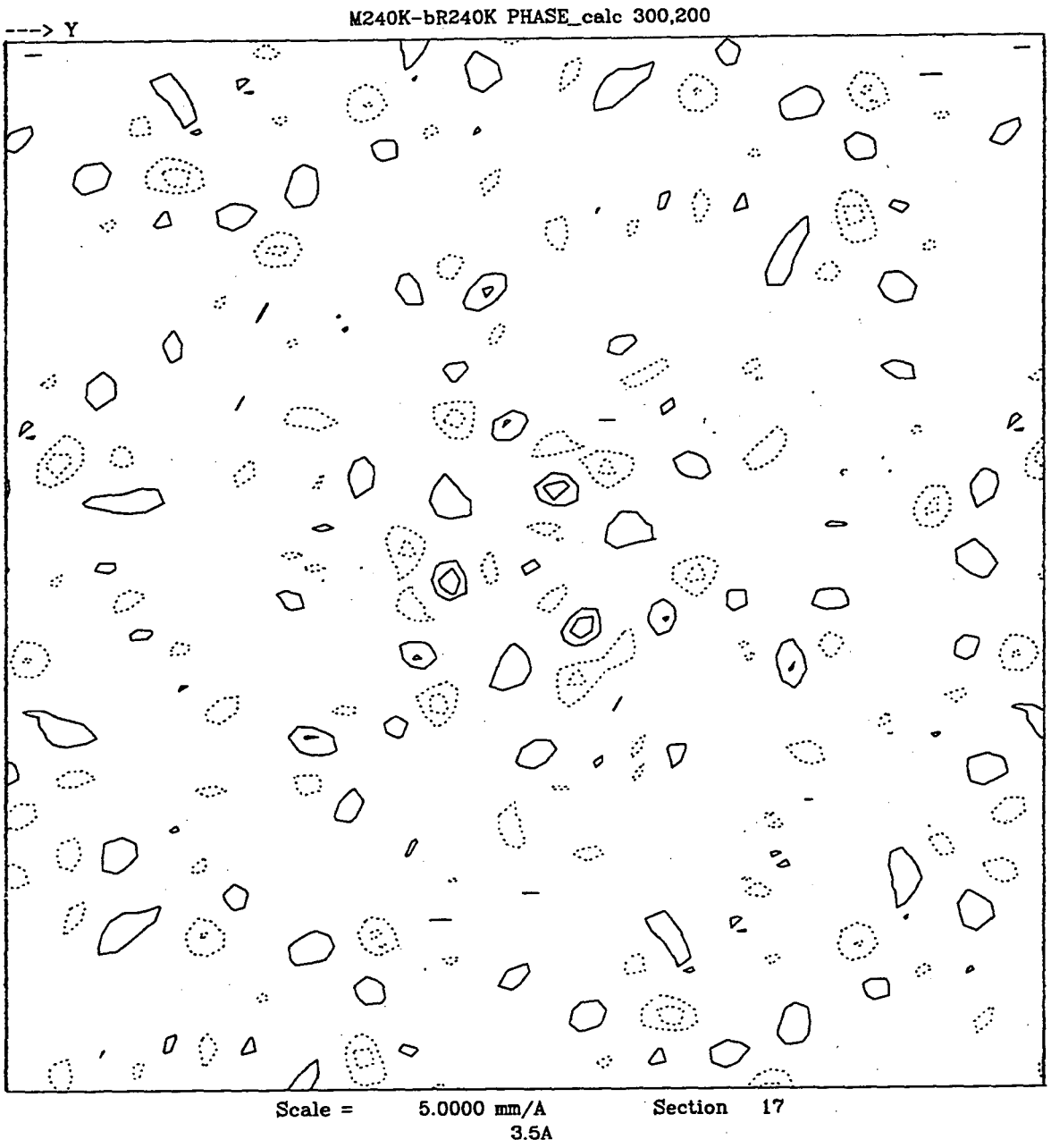

Position along z axis: **48 Å**

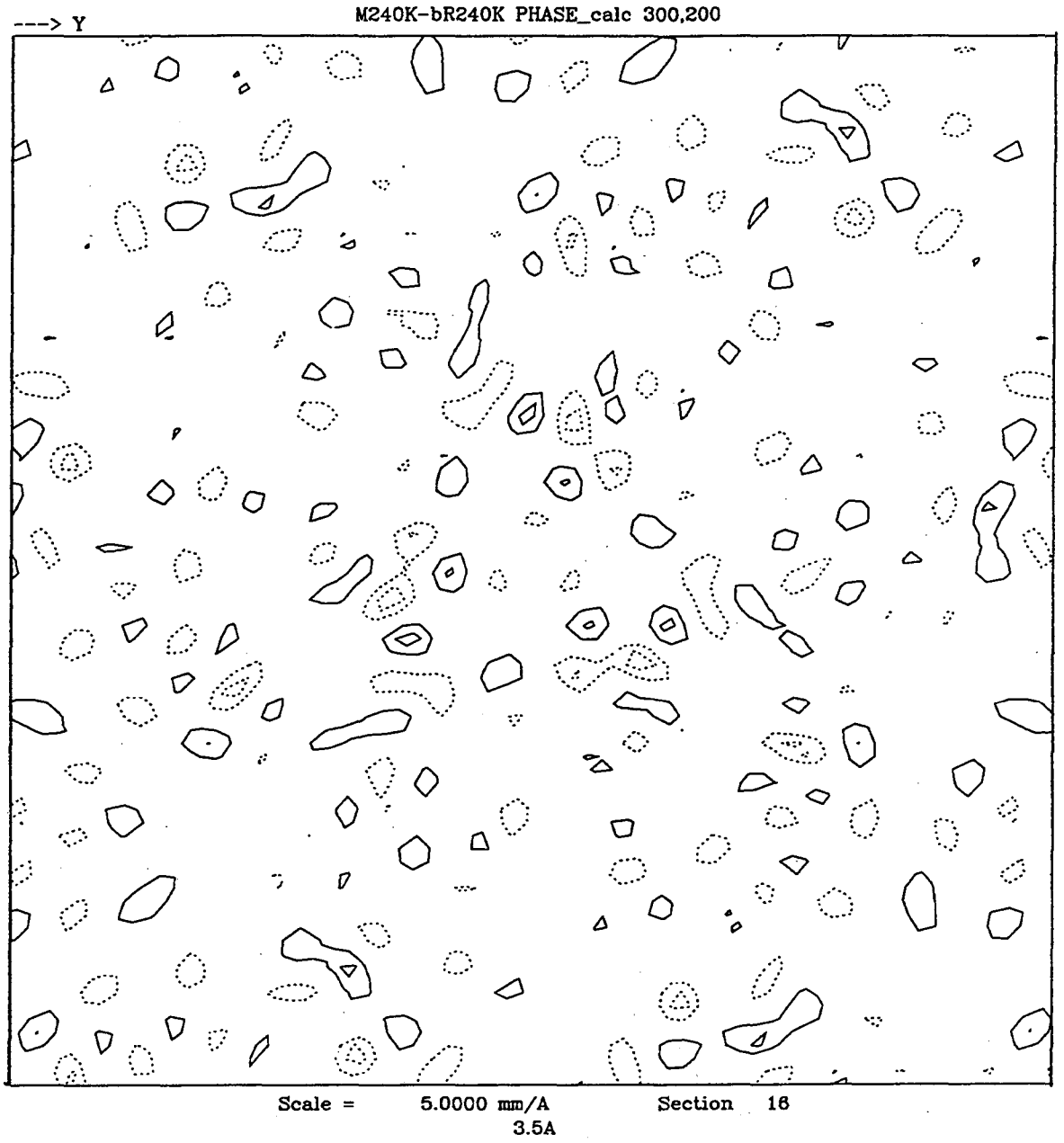

Position along z axis: **45 Å**

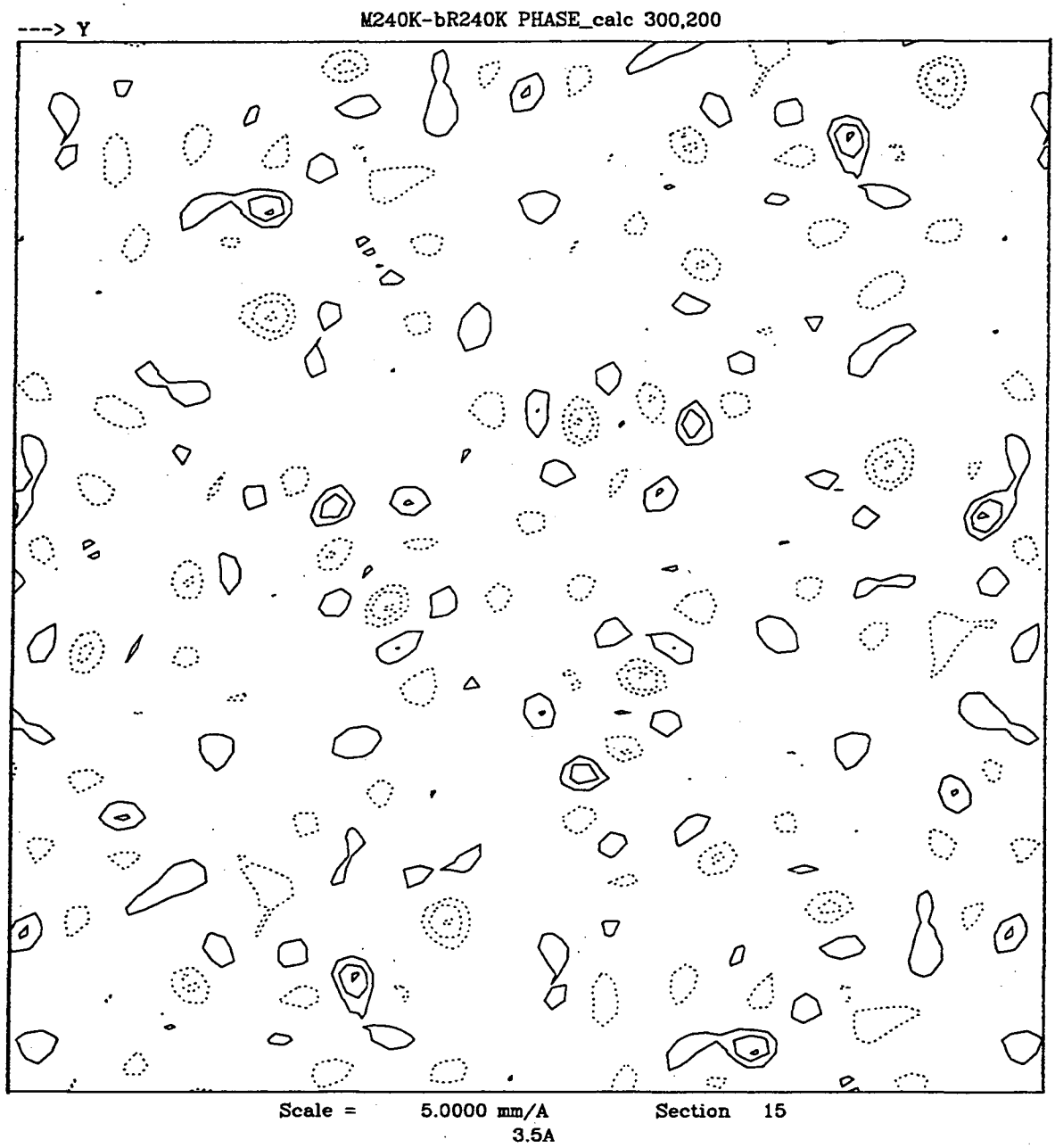

Position along z axis: **42 Å**

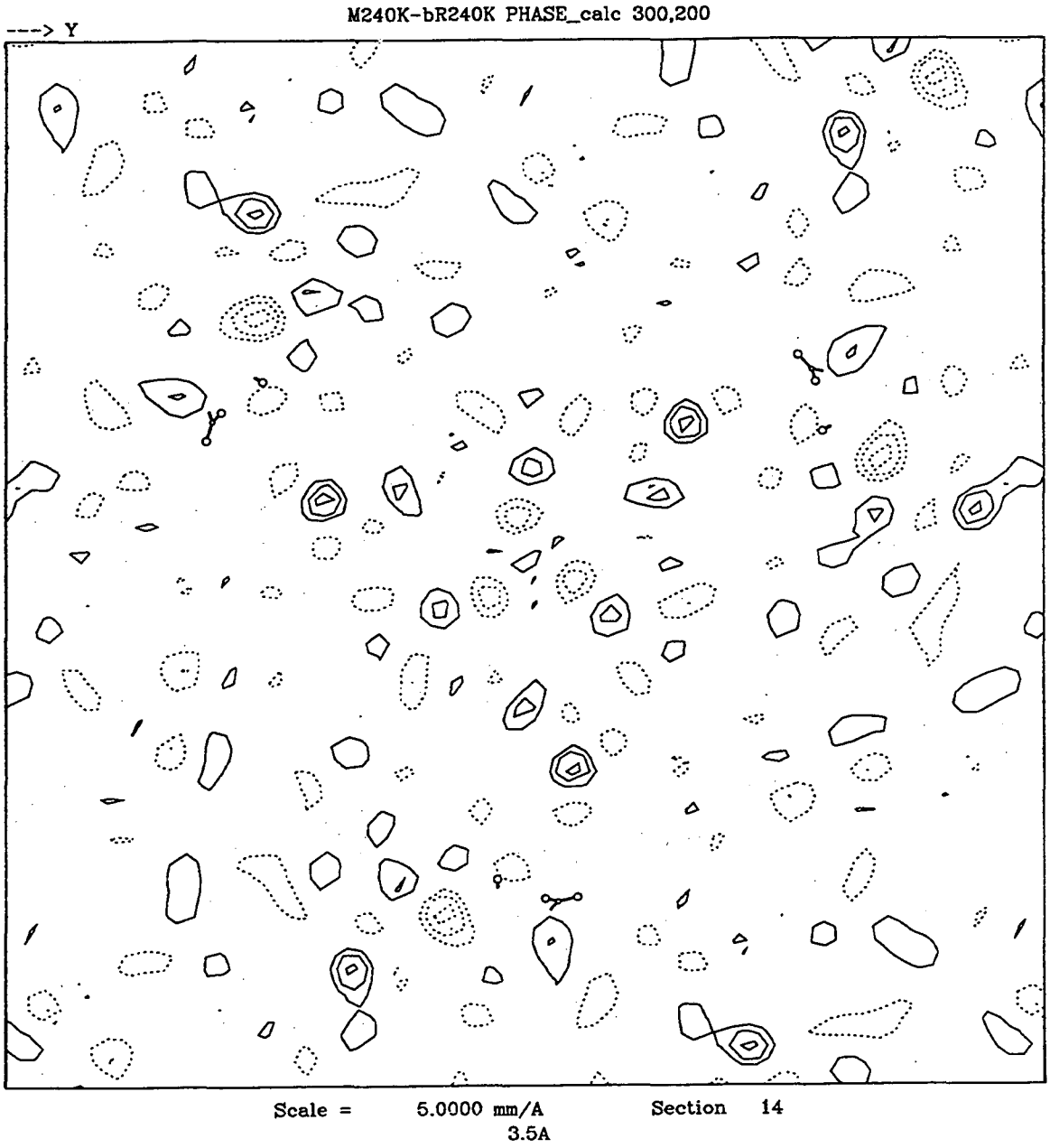

Position along z axis: **39** Å

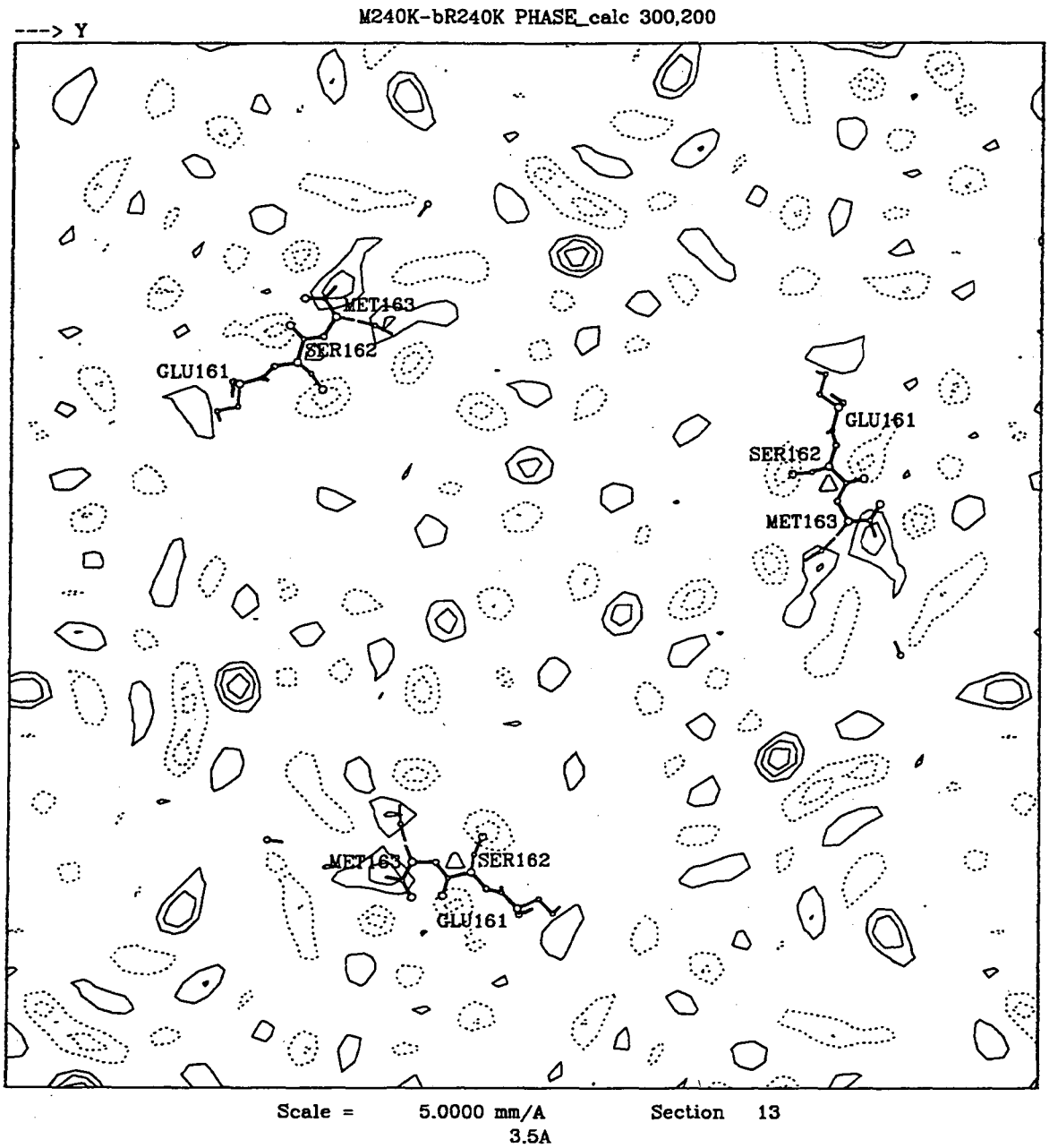

Position along z axis: **36 Å**

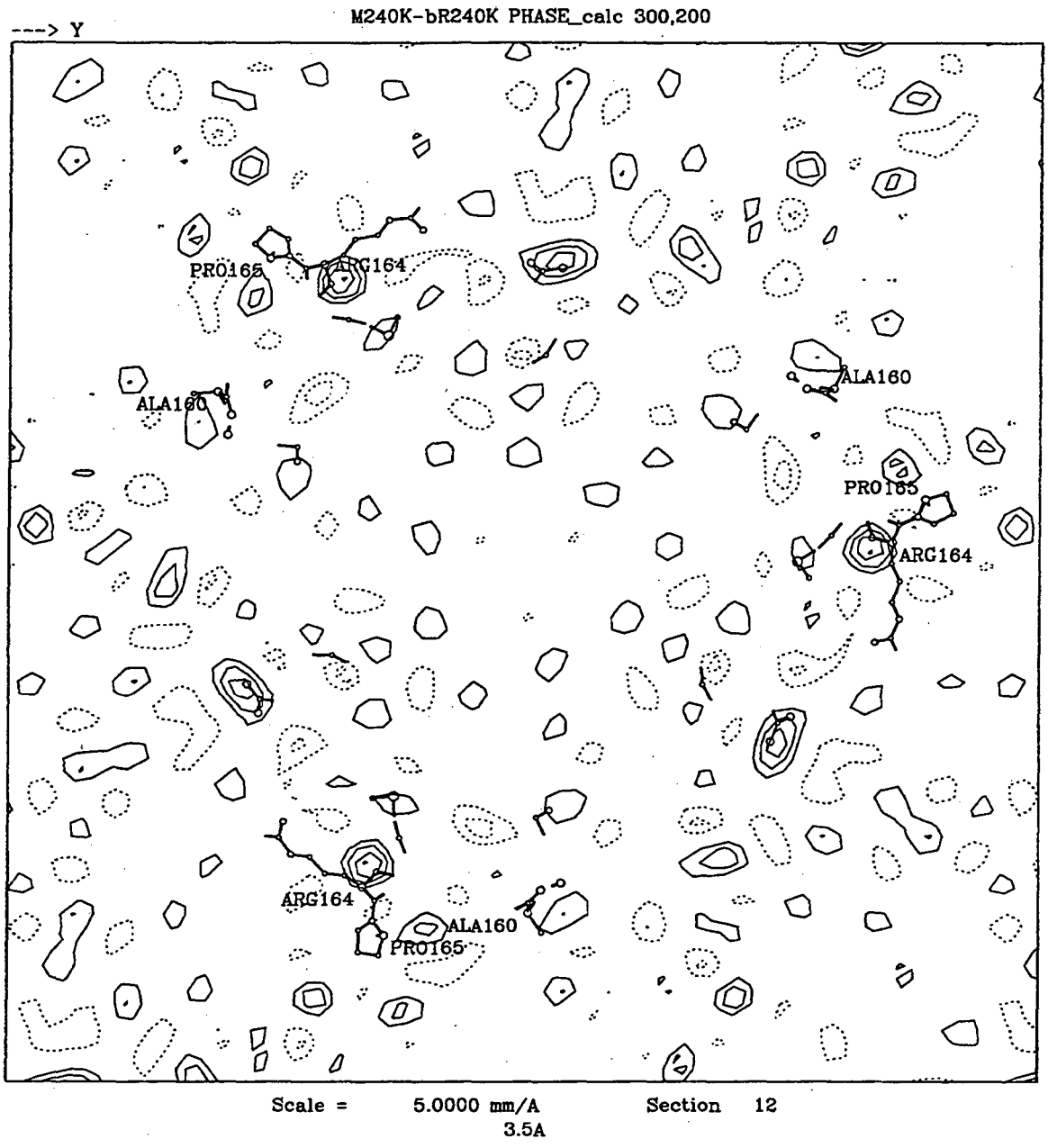

Position along z axis: **34 Å**

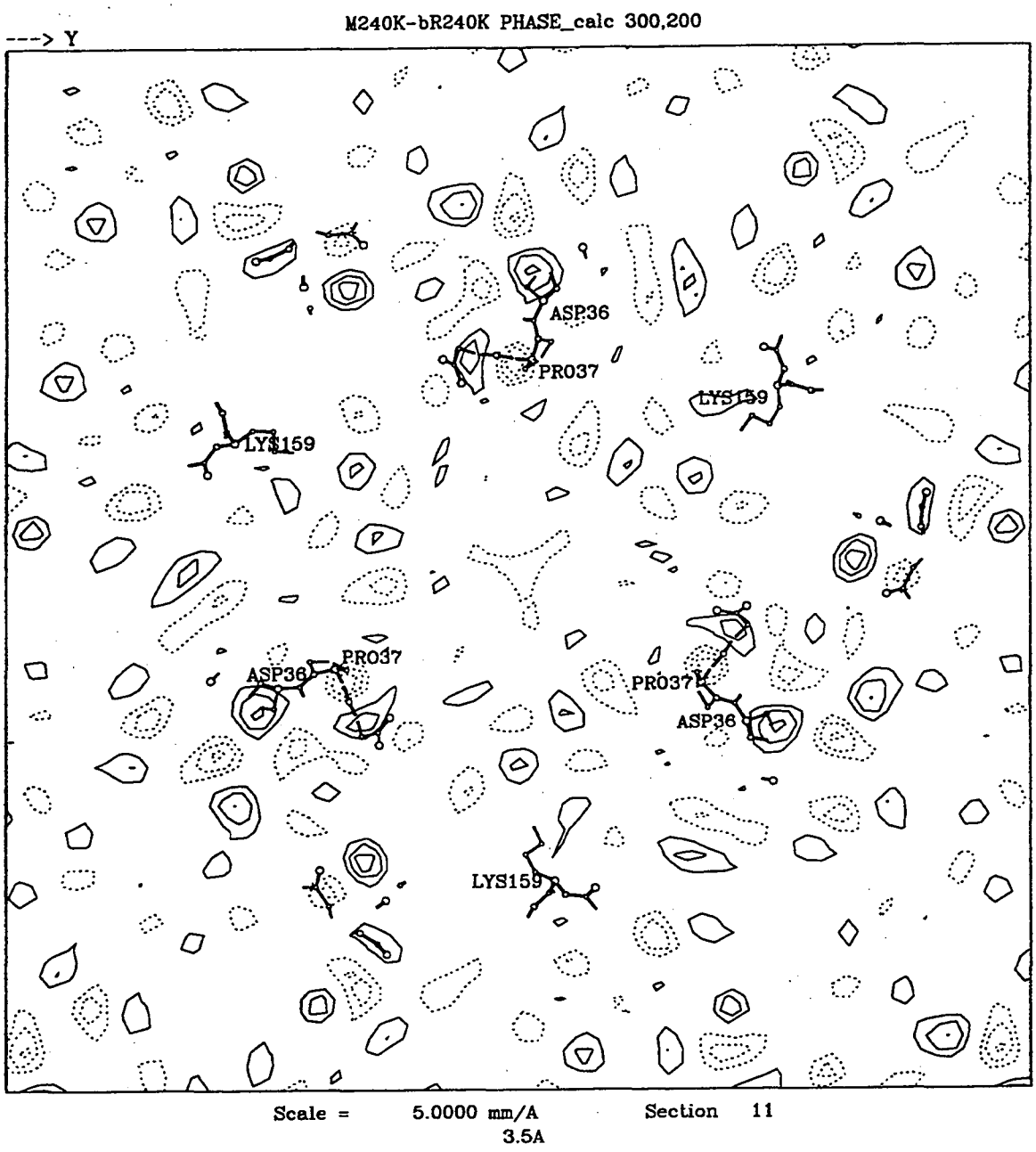

Position along z axis: **31** Å

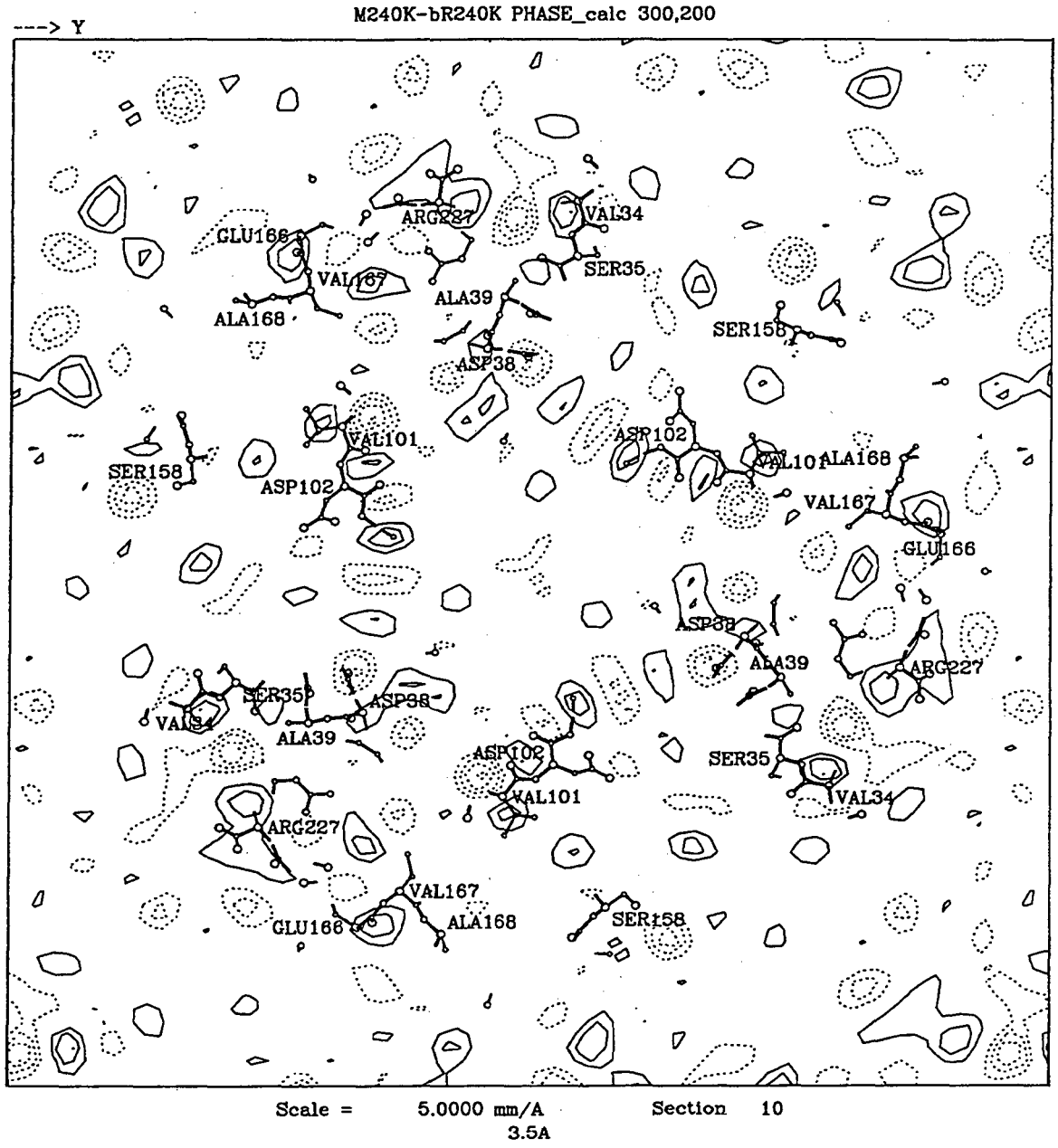

Position along z axis: **28 Å**

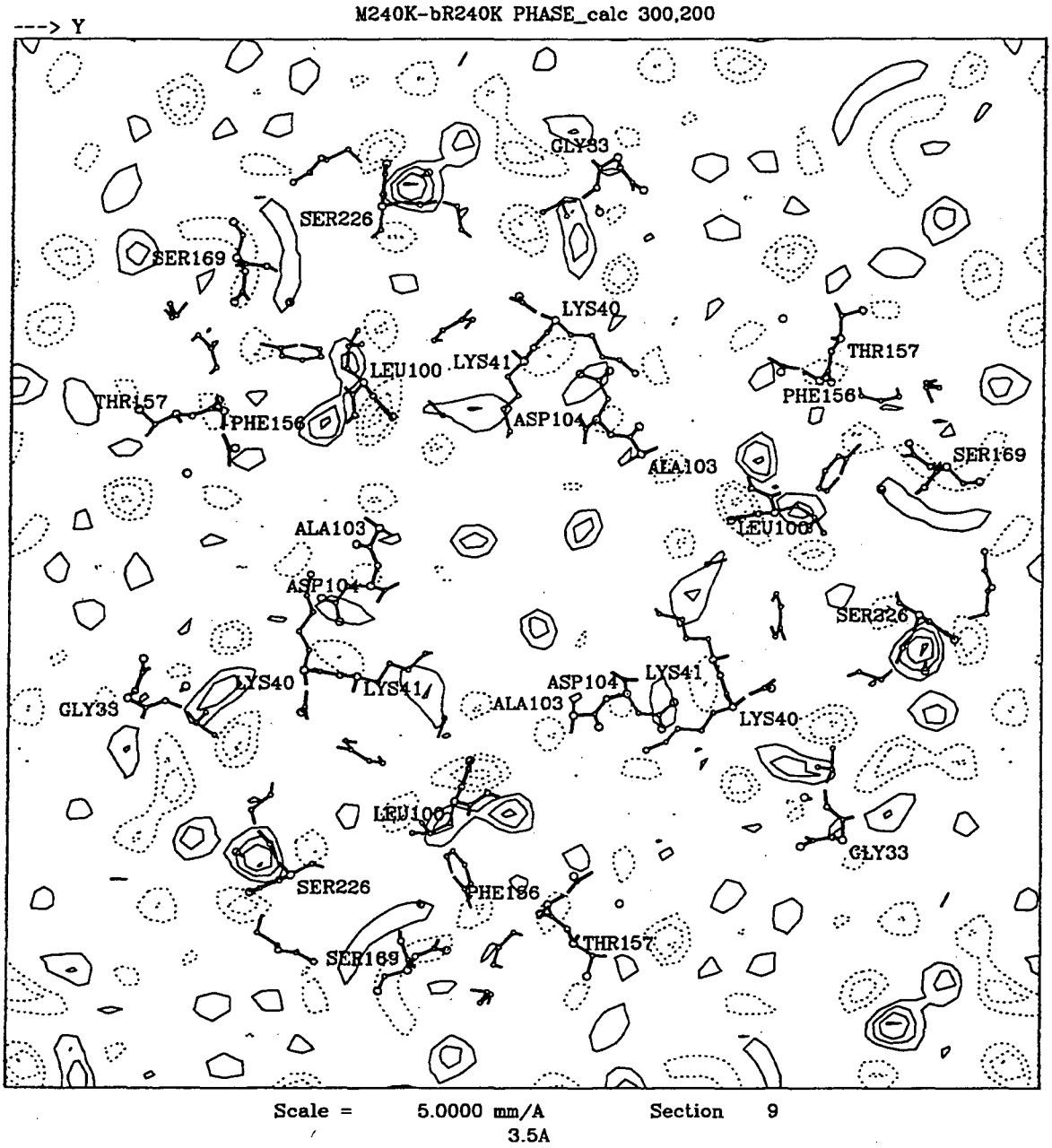

Position along z axis: **25 Å**

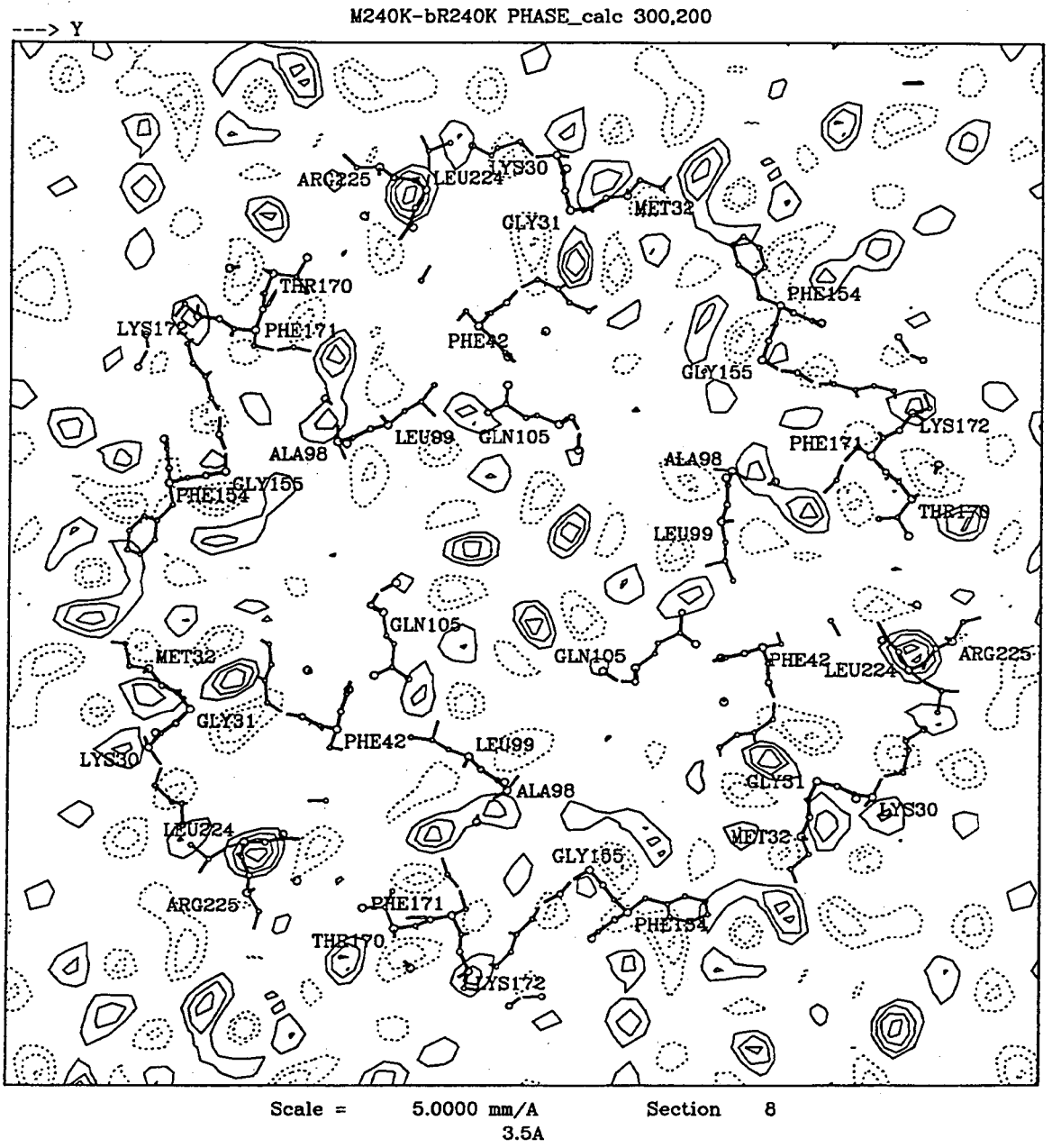

Position along z axis: **22** Å

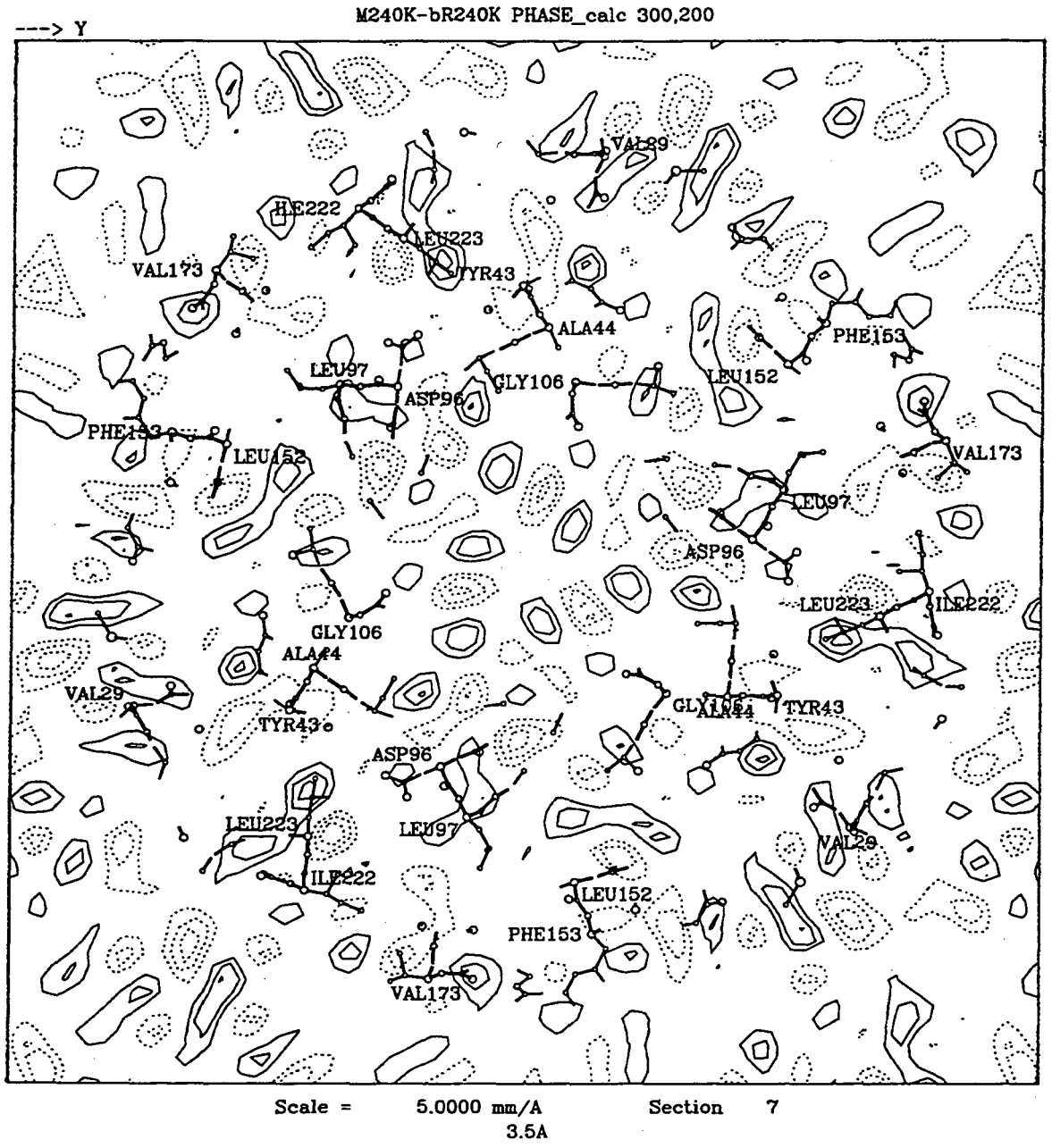

Position along z axis: **20 Å**

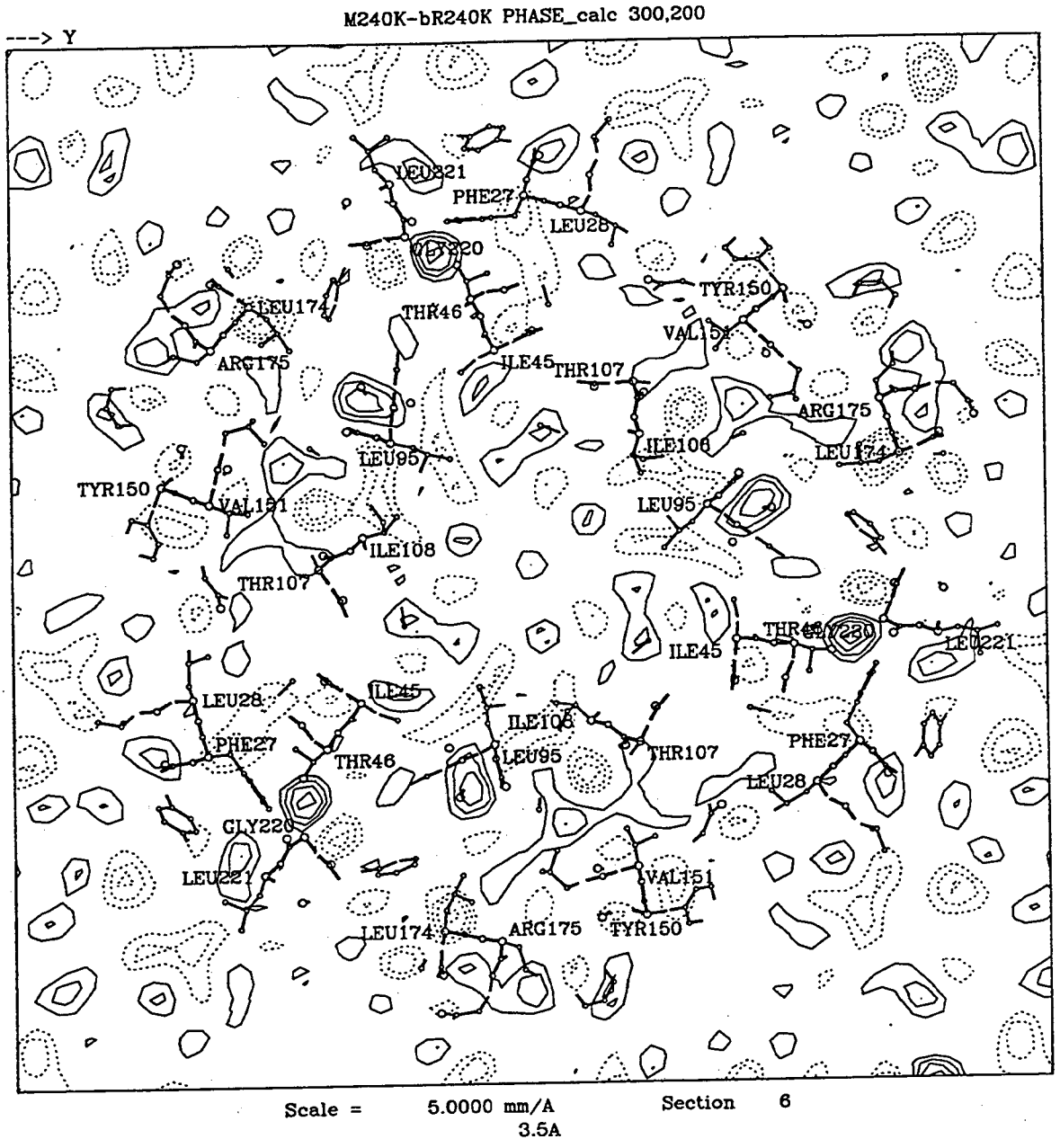

Position along z axis: **17 Å**

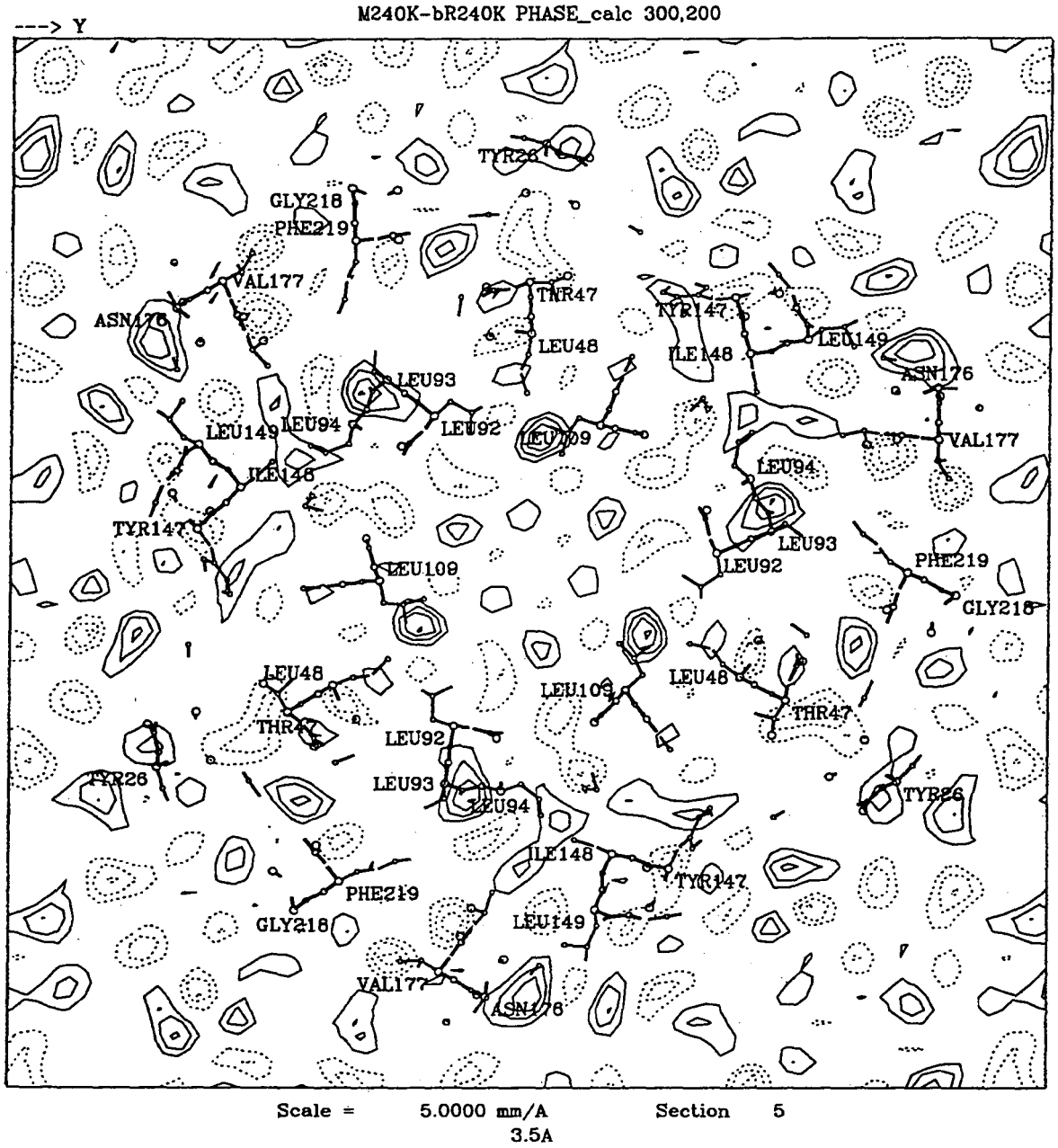

Position along z axis: **14** Å

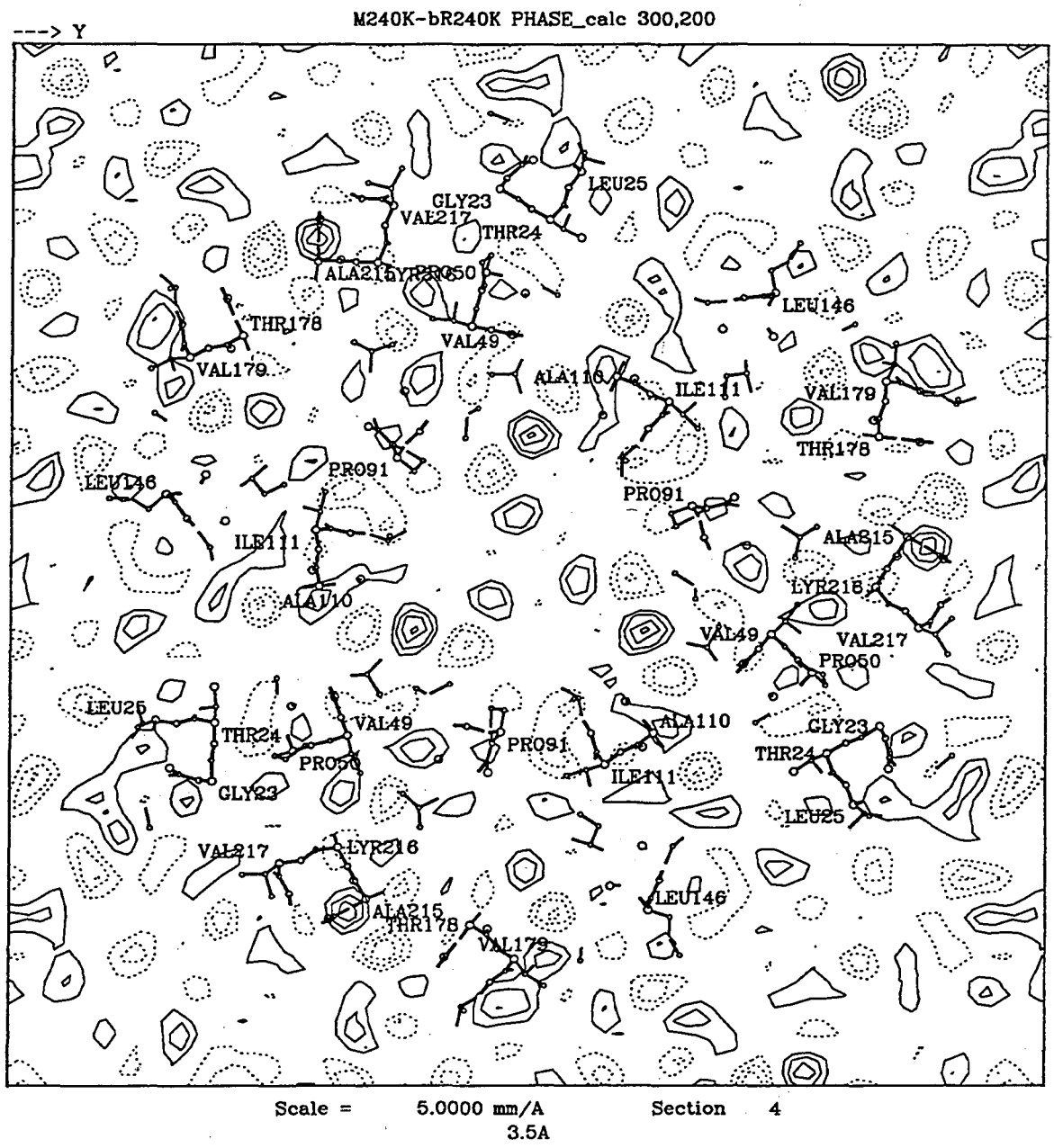

Position along z axis: **11 Å**

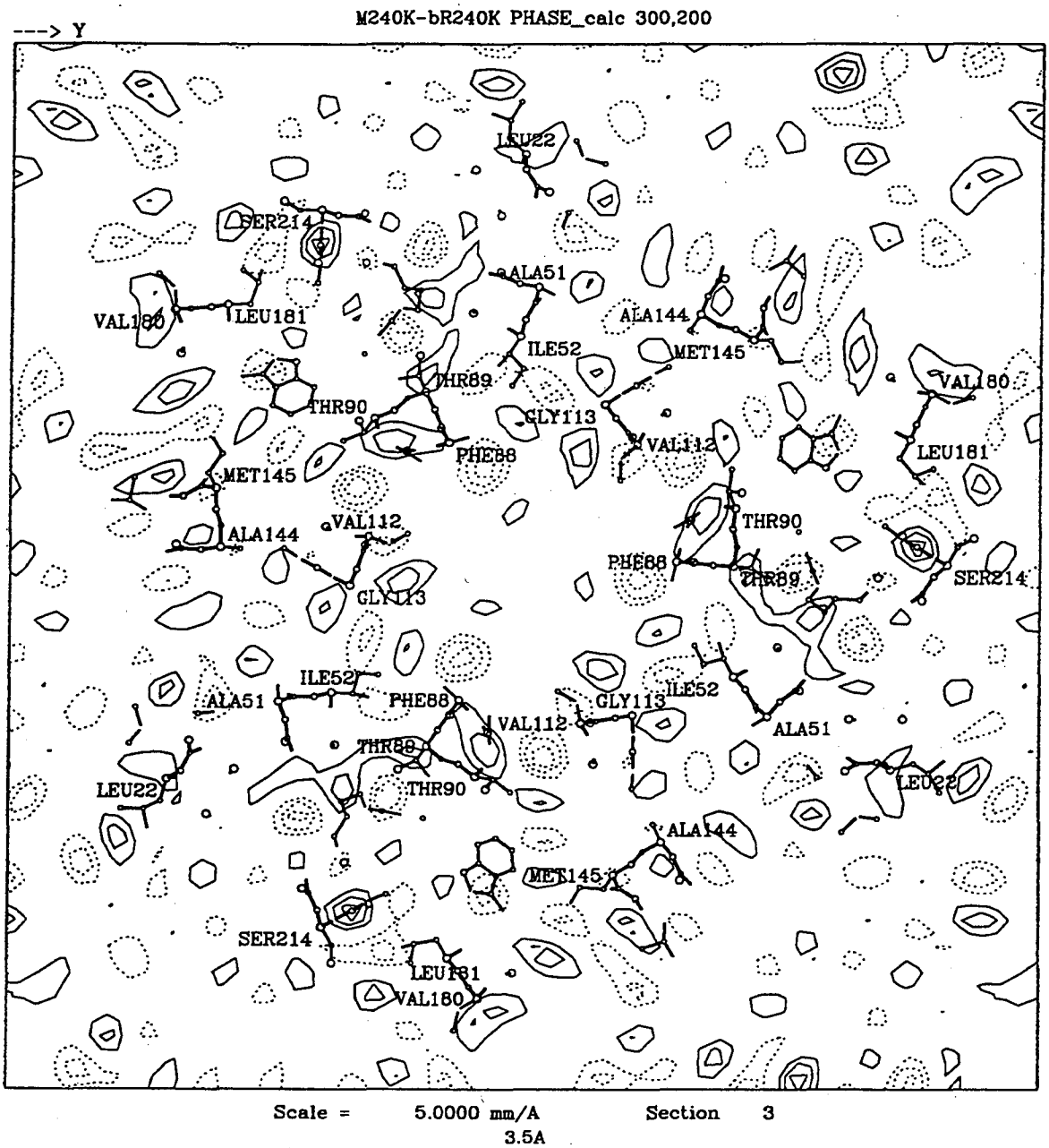

Position along z axis: **8 Å**

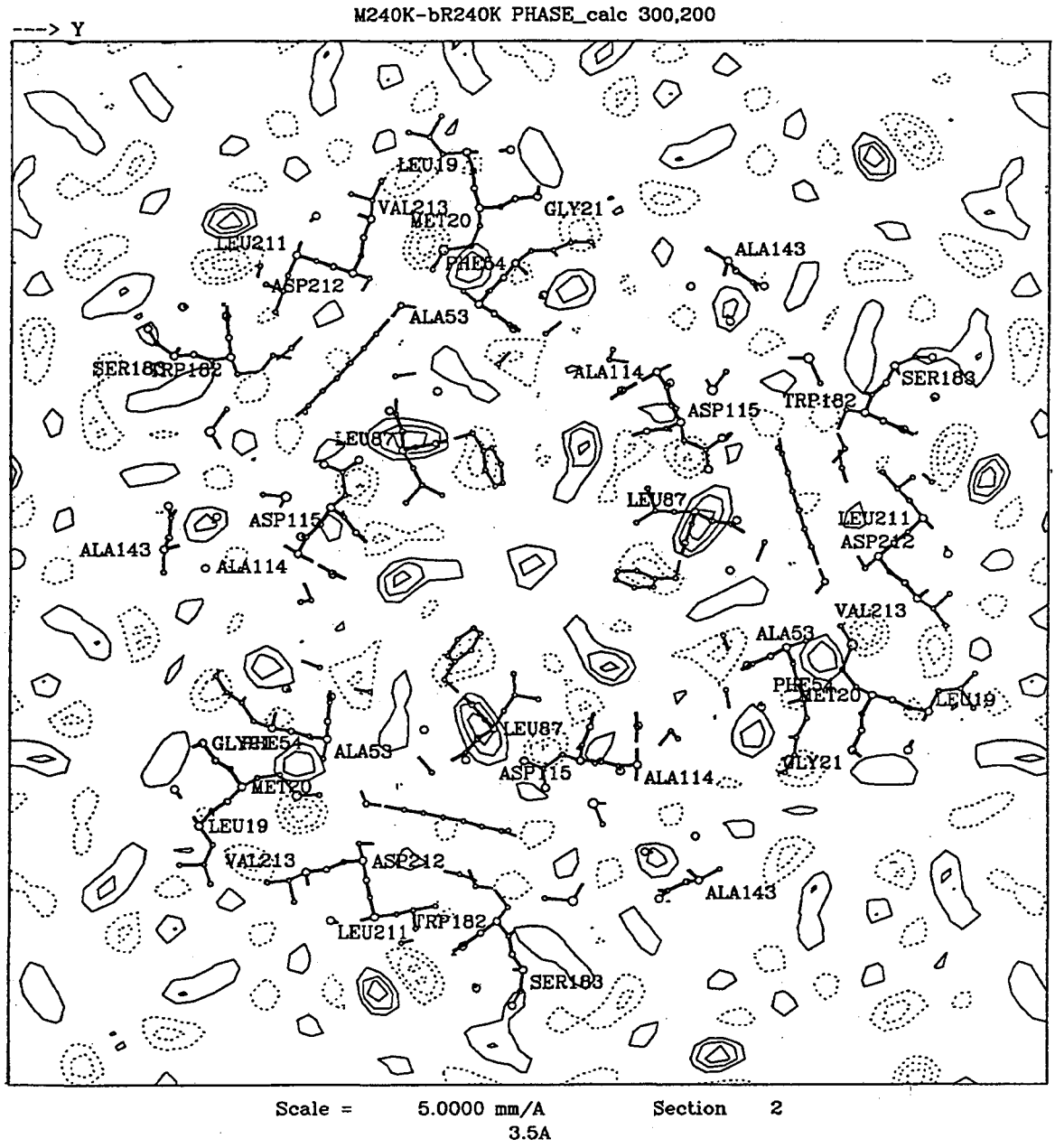

Position along z axis: **6** Å

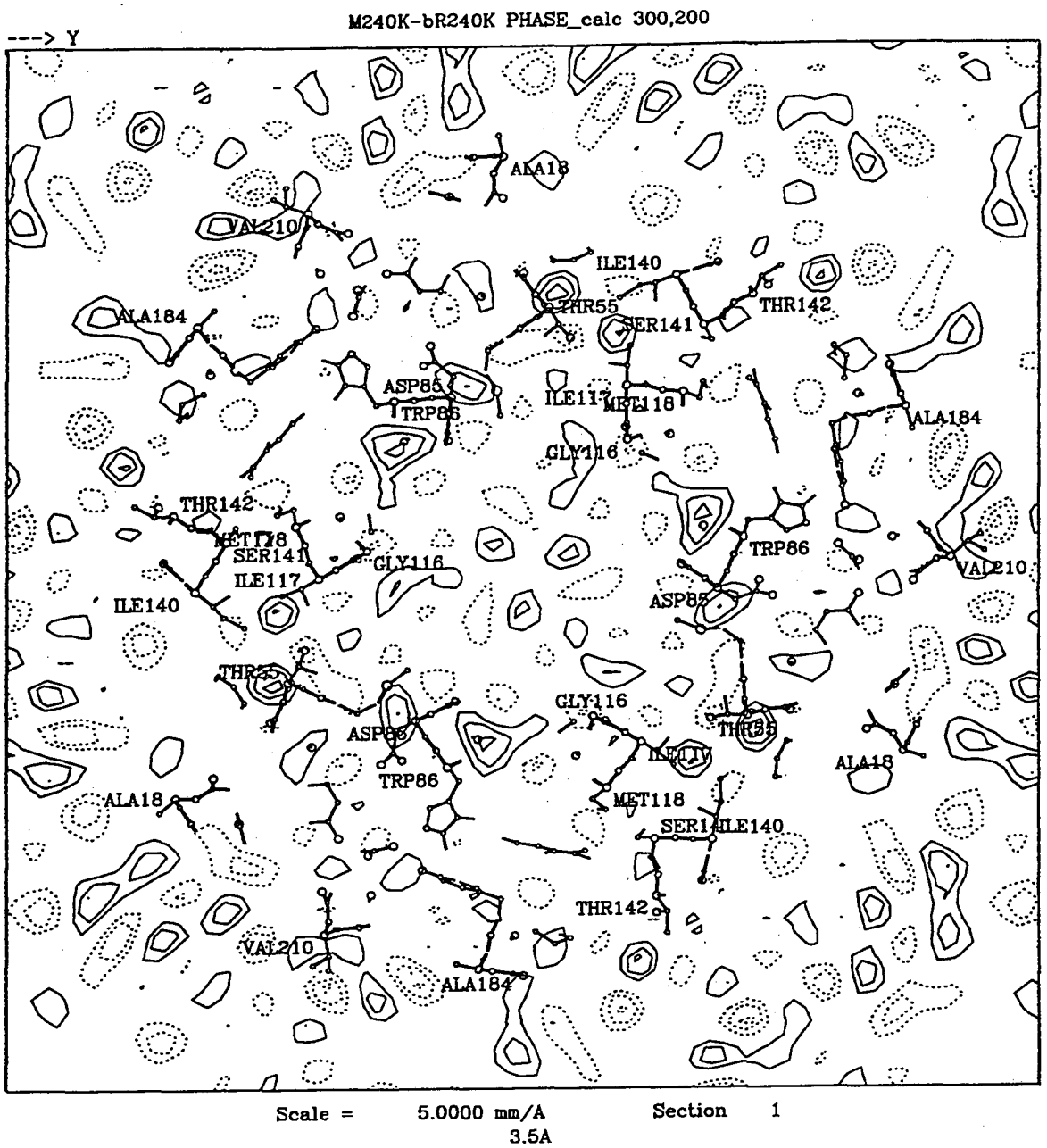

Position along z axis: 3 Å

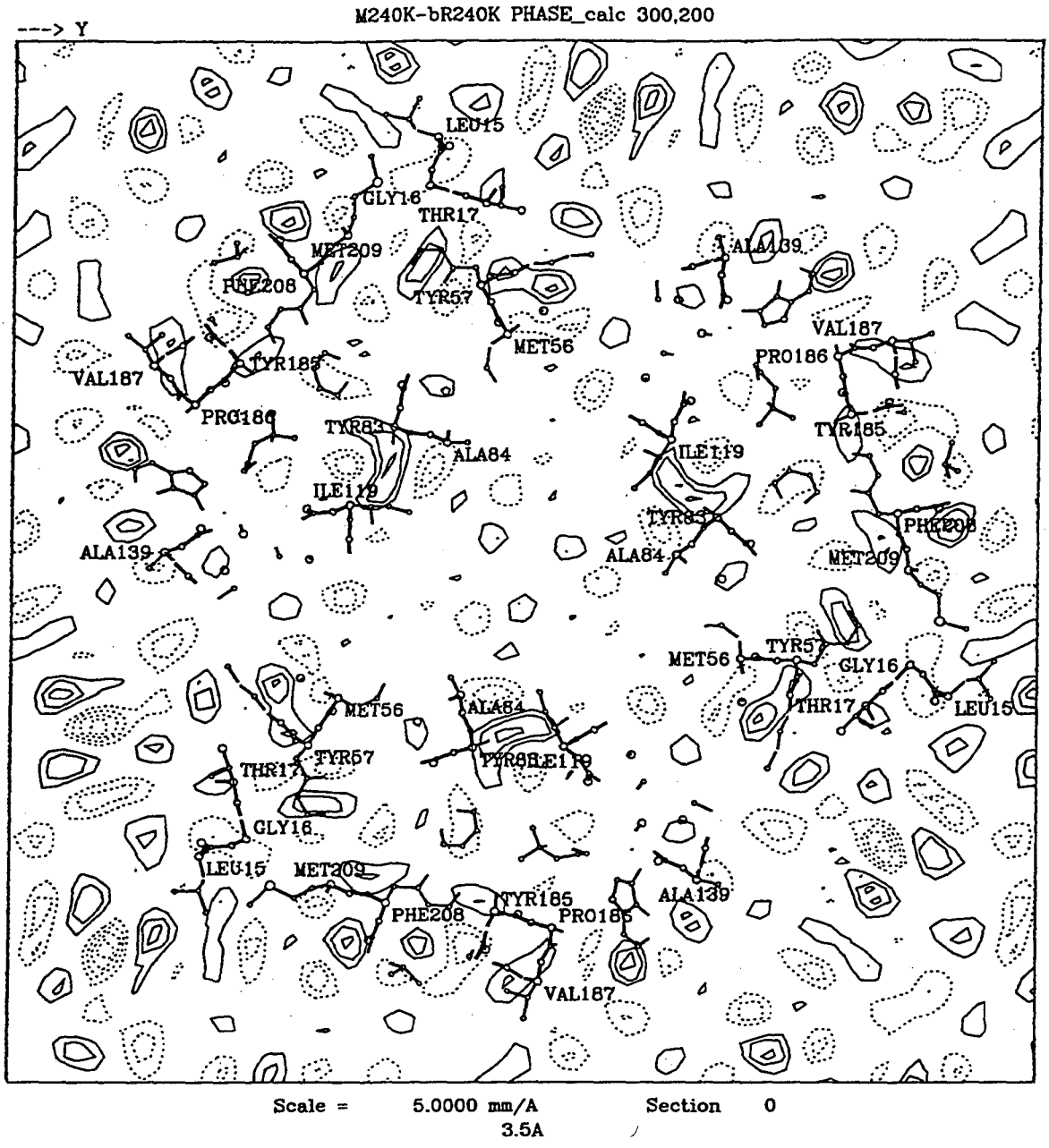

Position along z axis: **0** Å

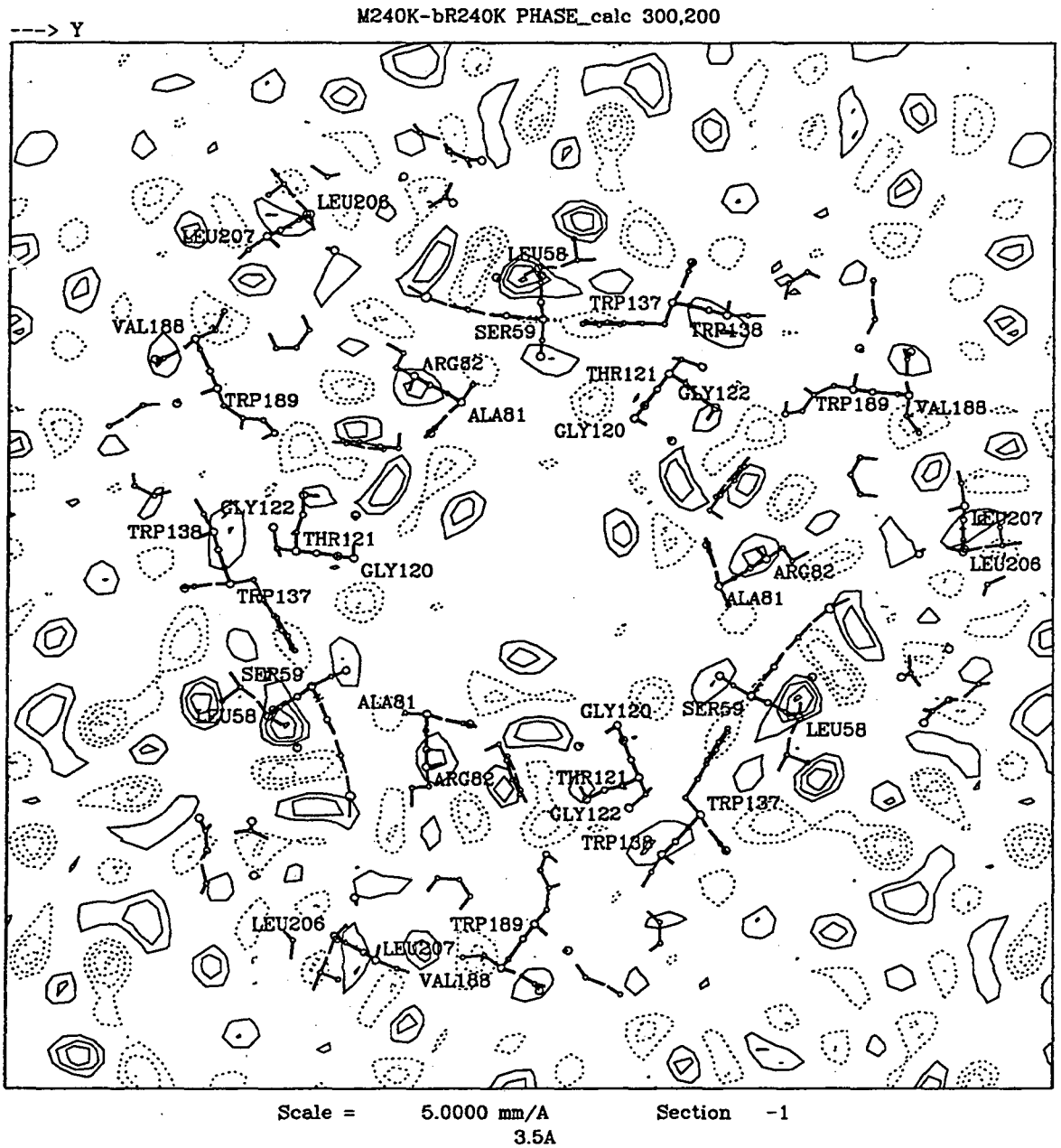

Position along z axis: **-3 Å**

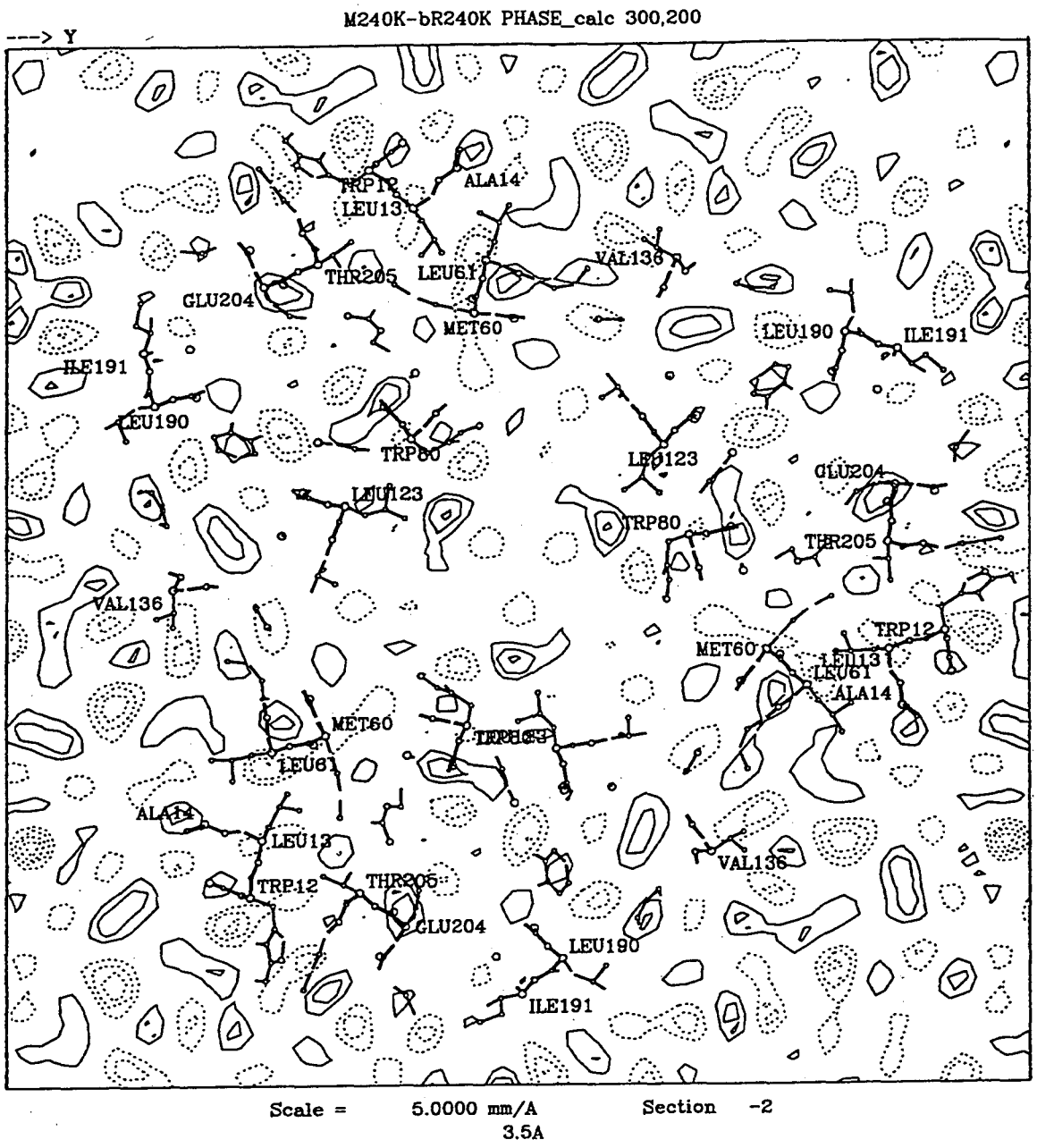

Position along z axis: **-6 Å**

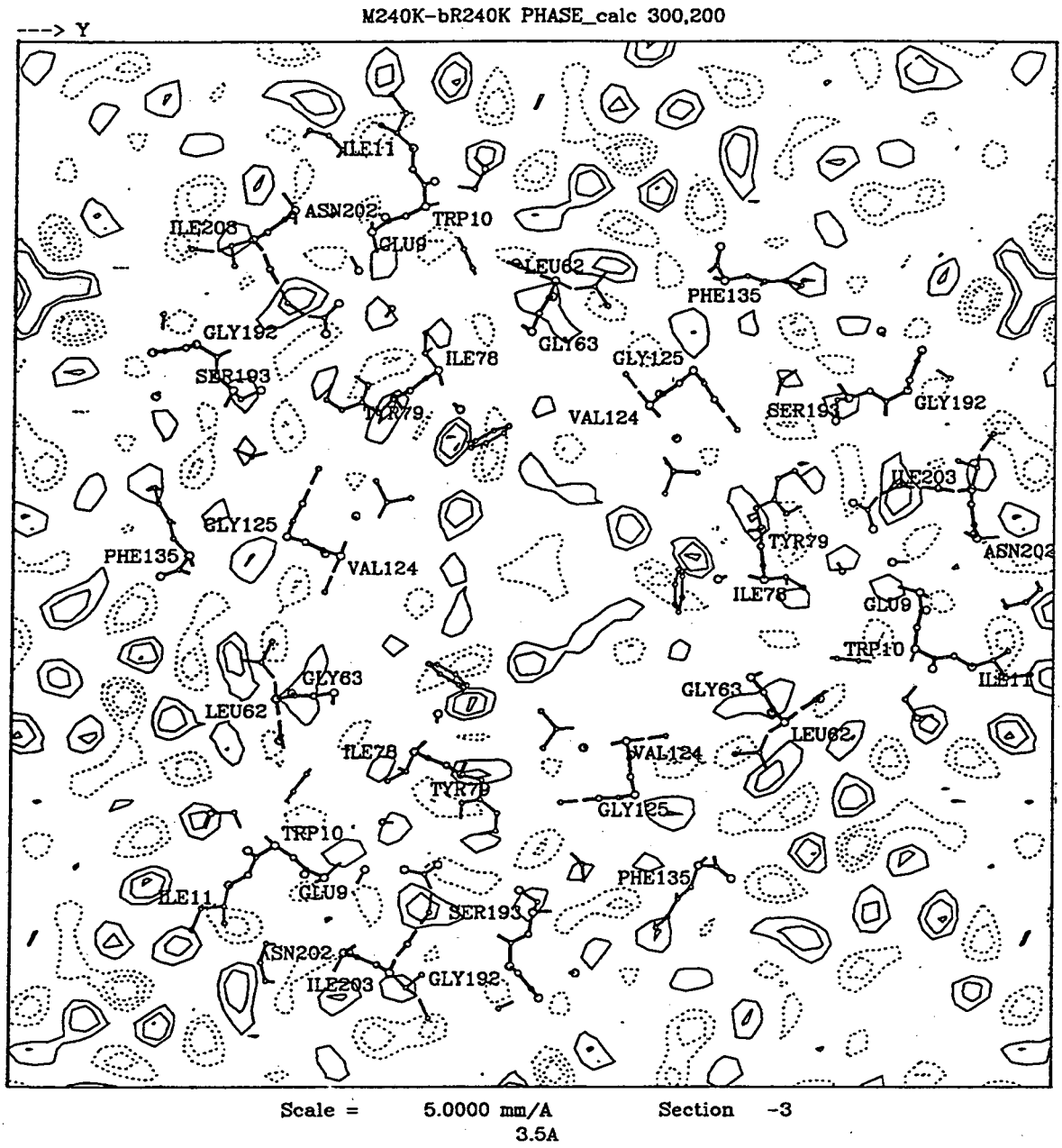

Position along z axis: **-8 Å**

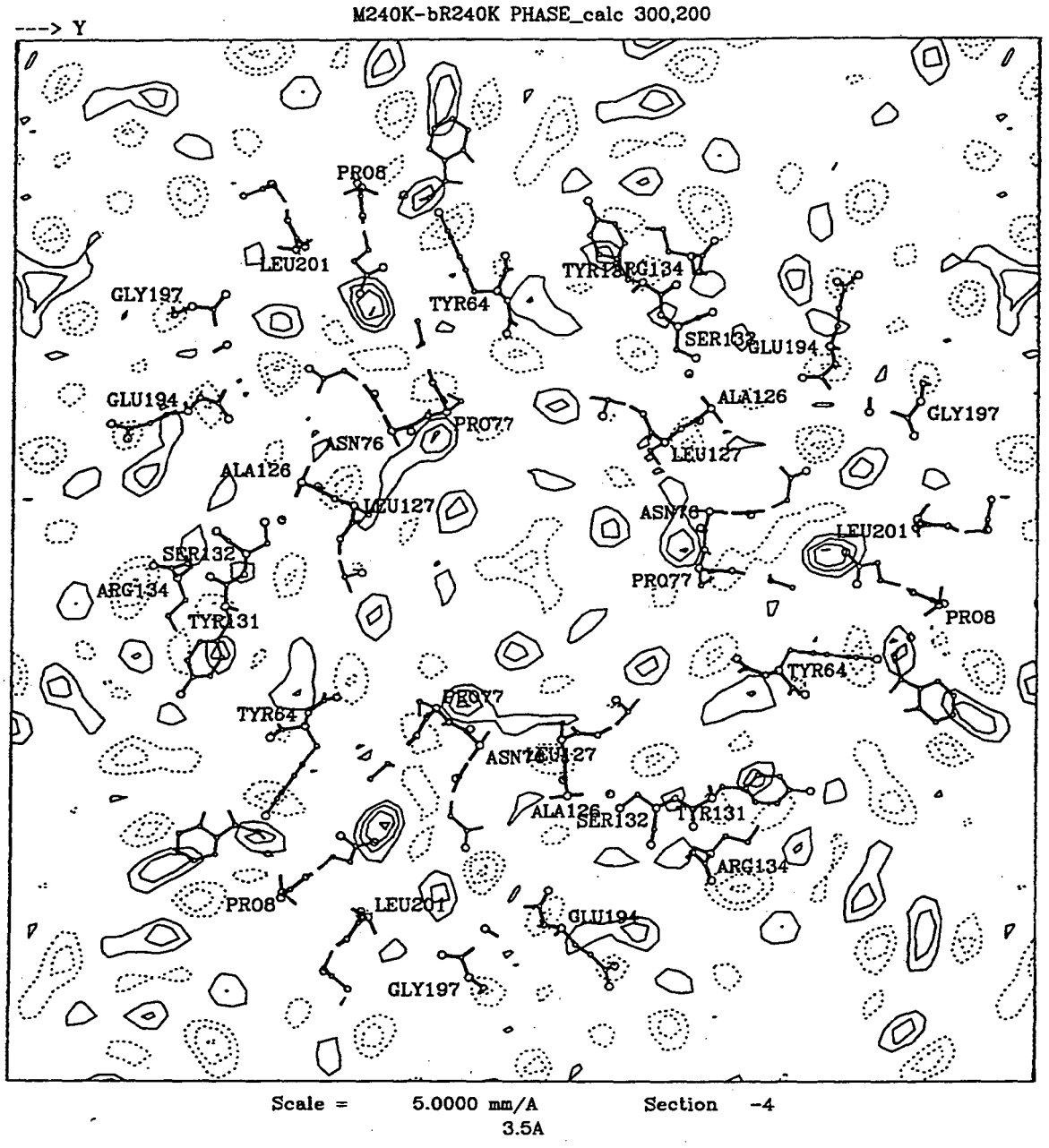

Position along z axis: **-11 Å**

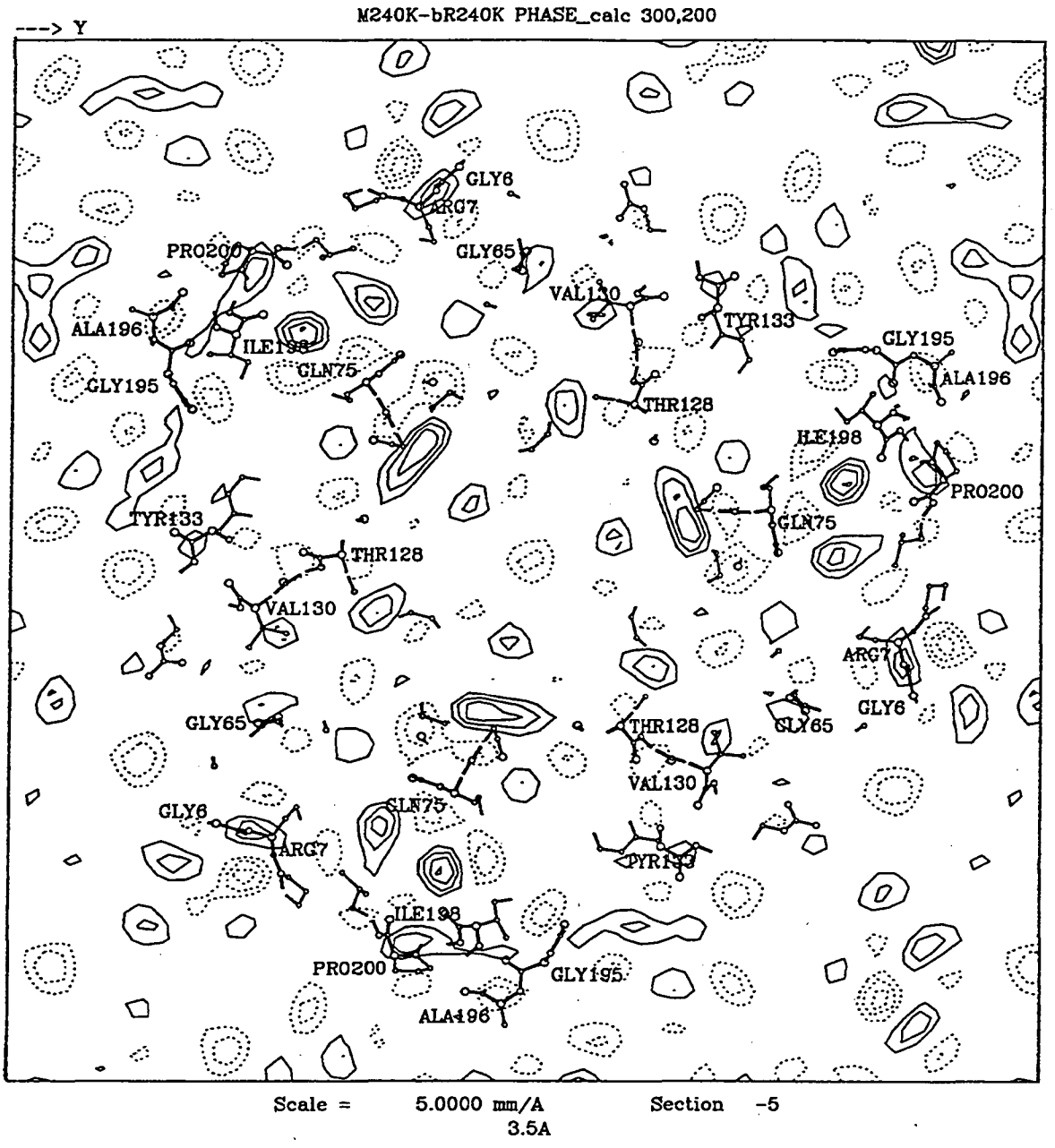

Position along z axis: **-14 Å**

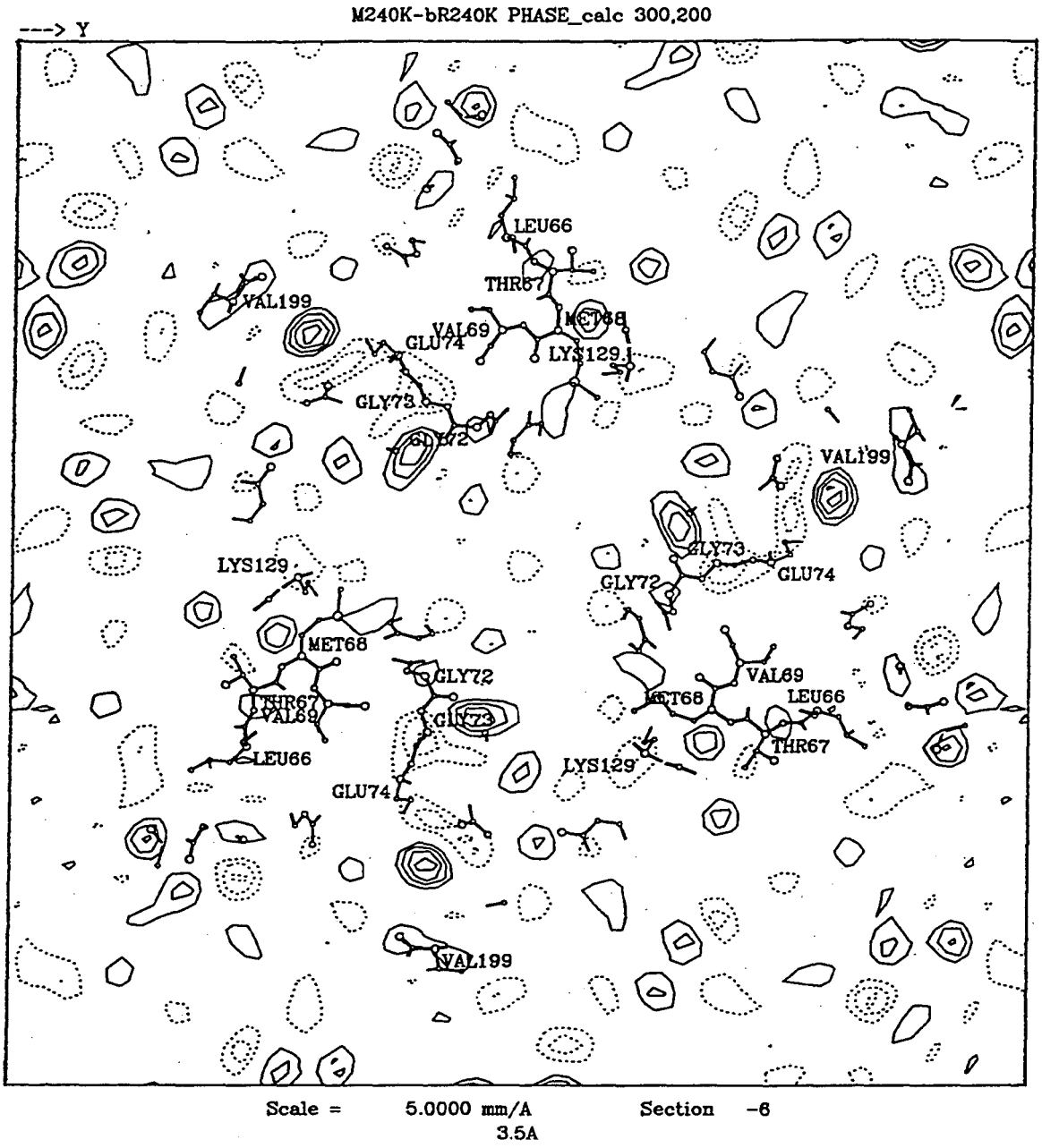

Position along z axis: **-17 Å**

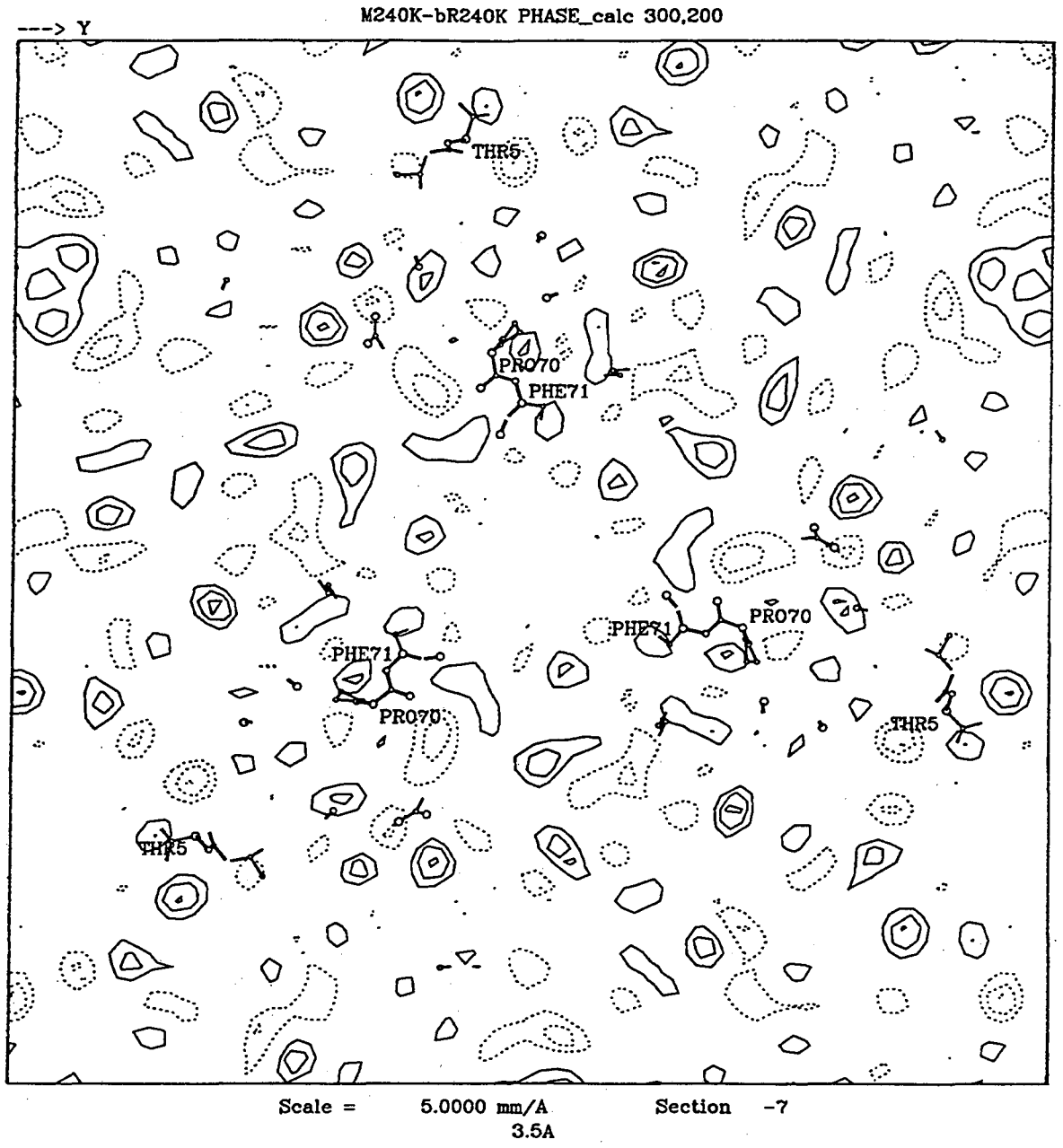

Position along z axis: **-20 Å**

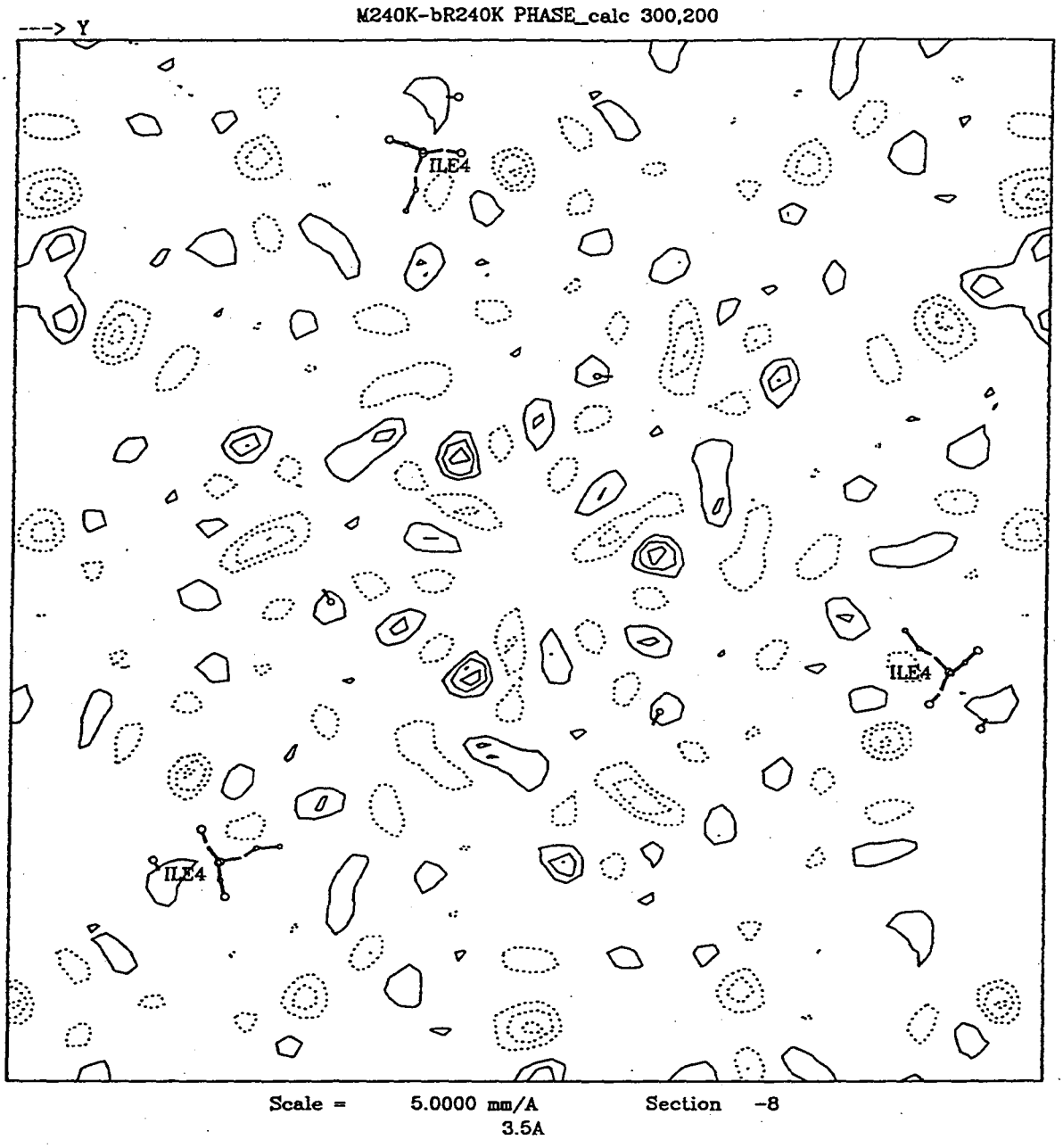

Position along z axis: **-22 Å**

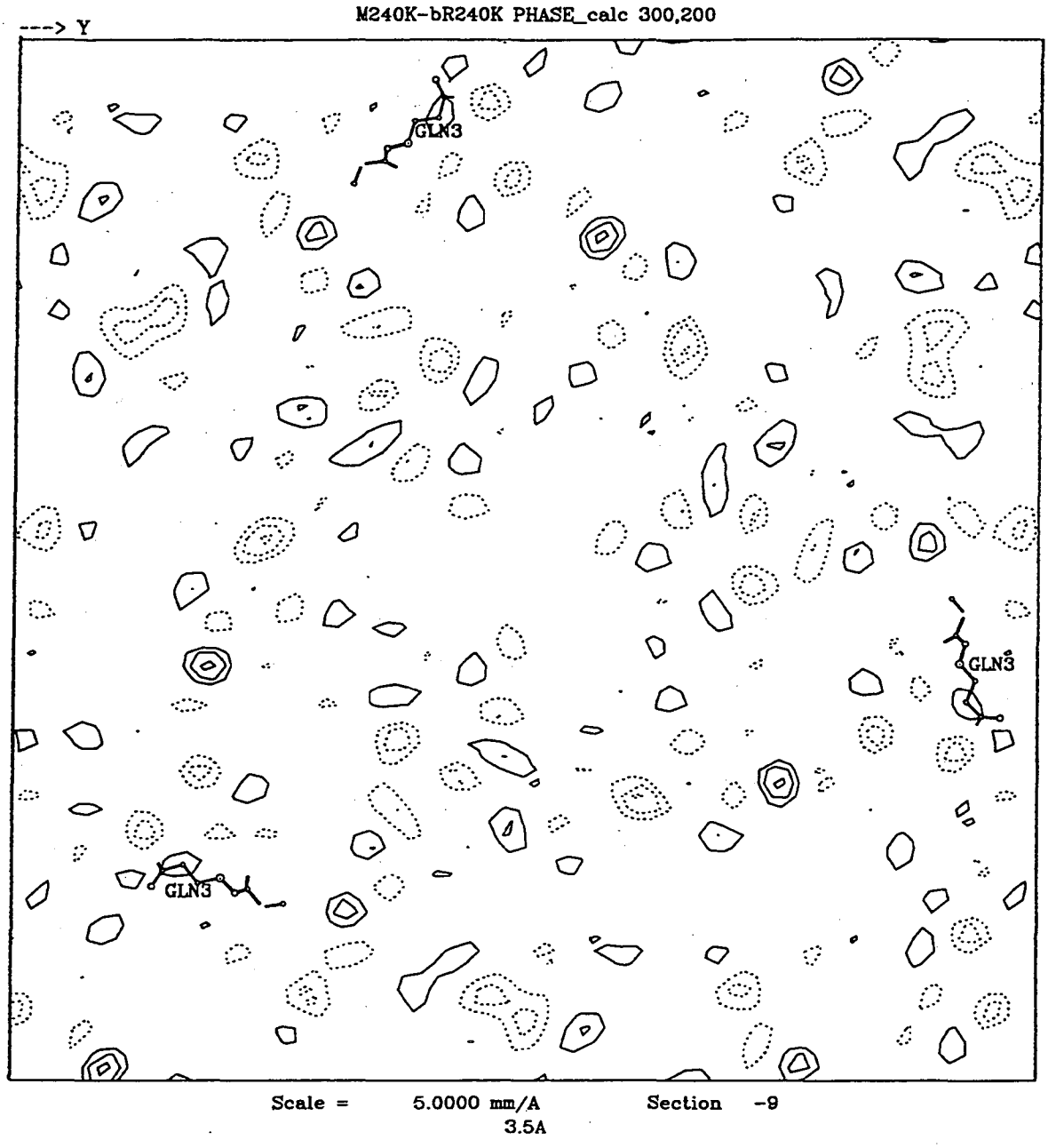

Position along z axis: **-25 Å**

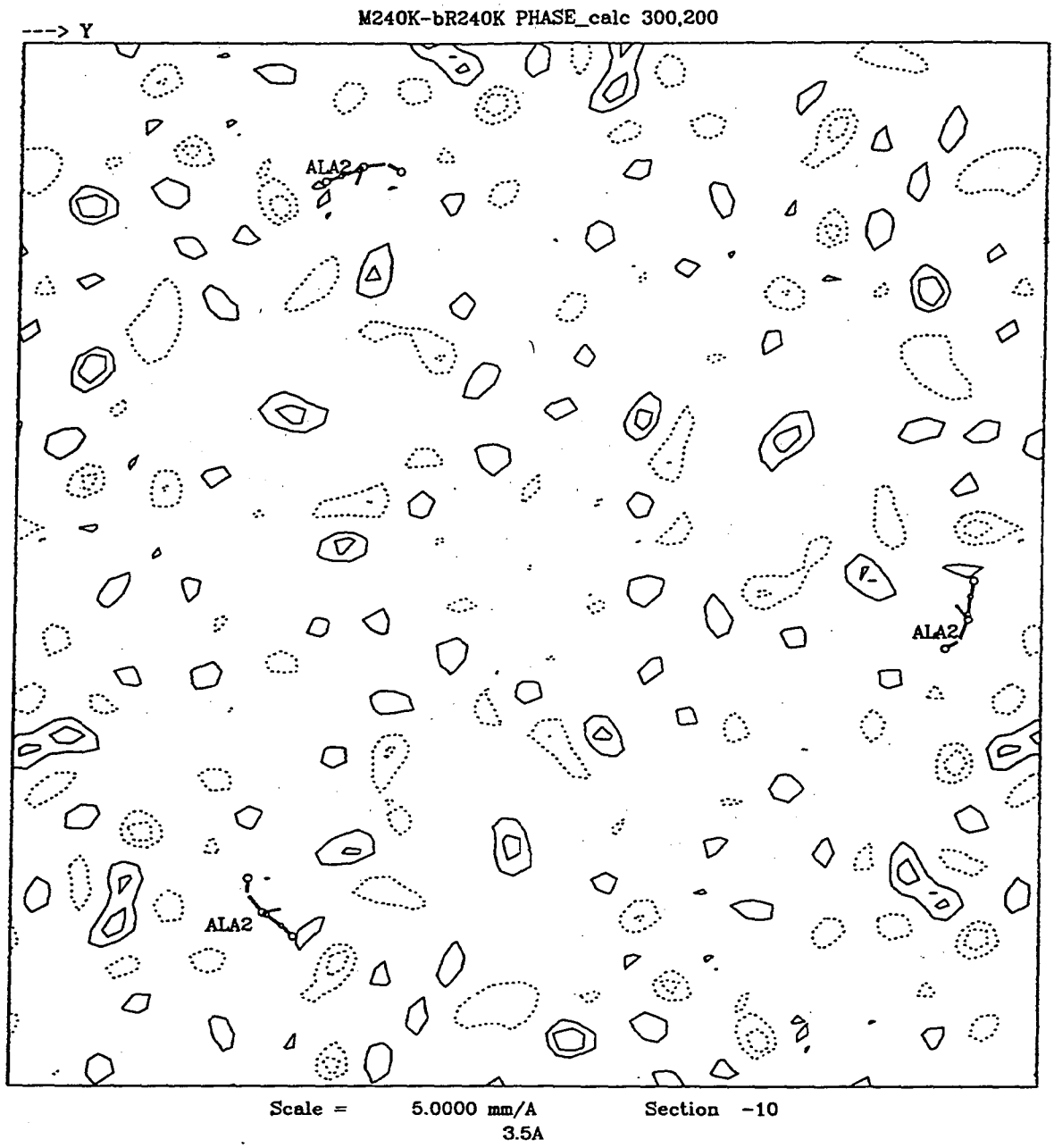

Position along z axis: **-28 Å**

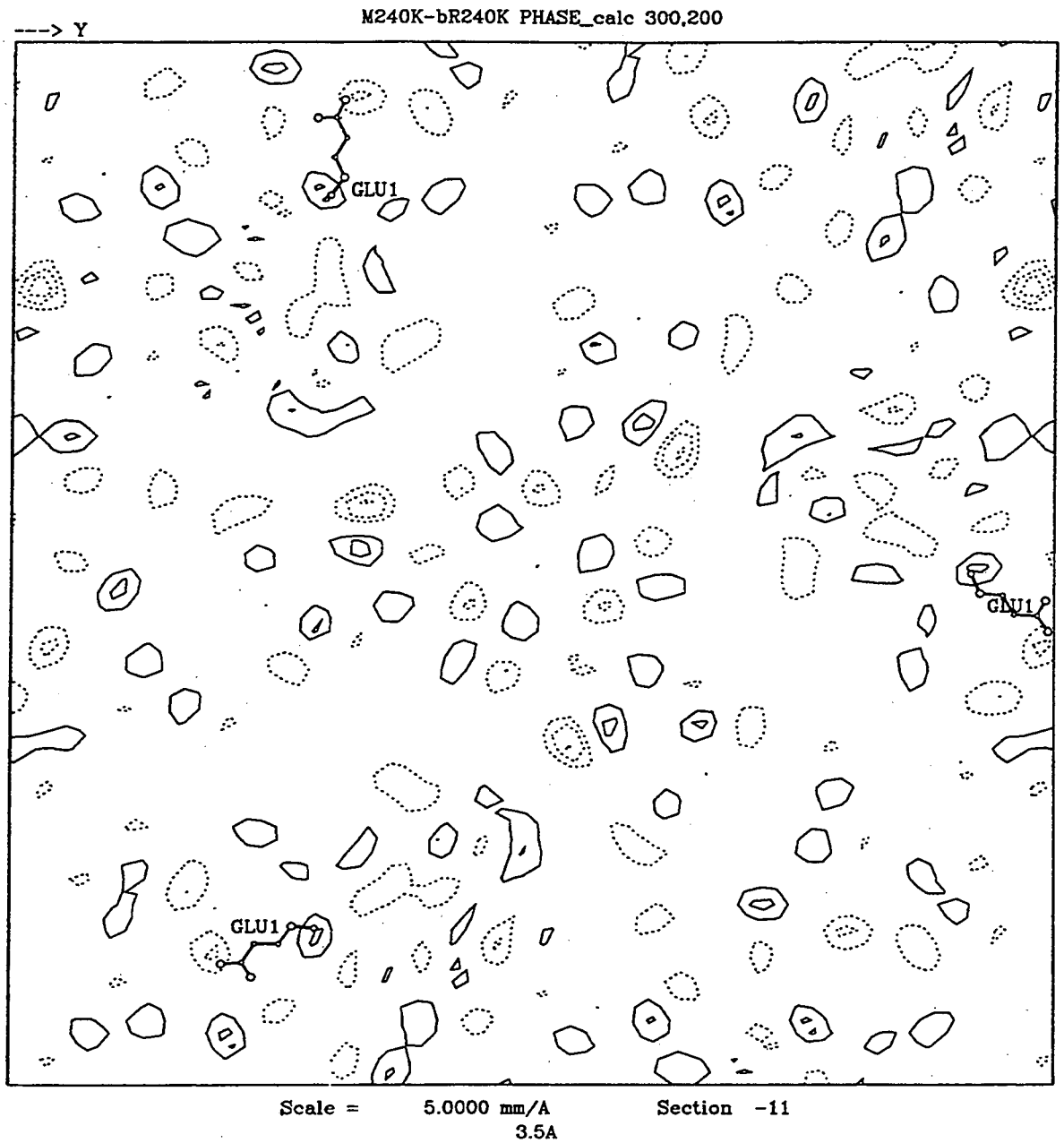

Position along z axis: **-31 Å**

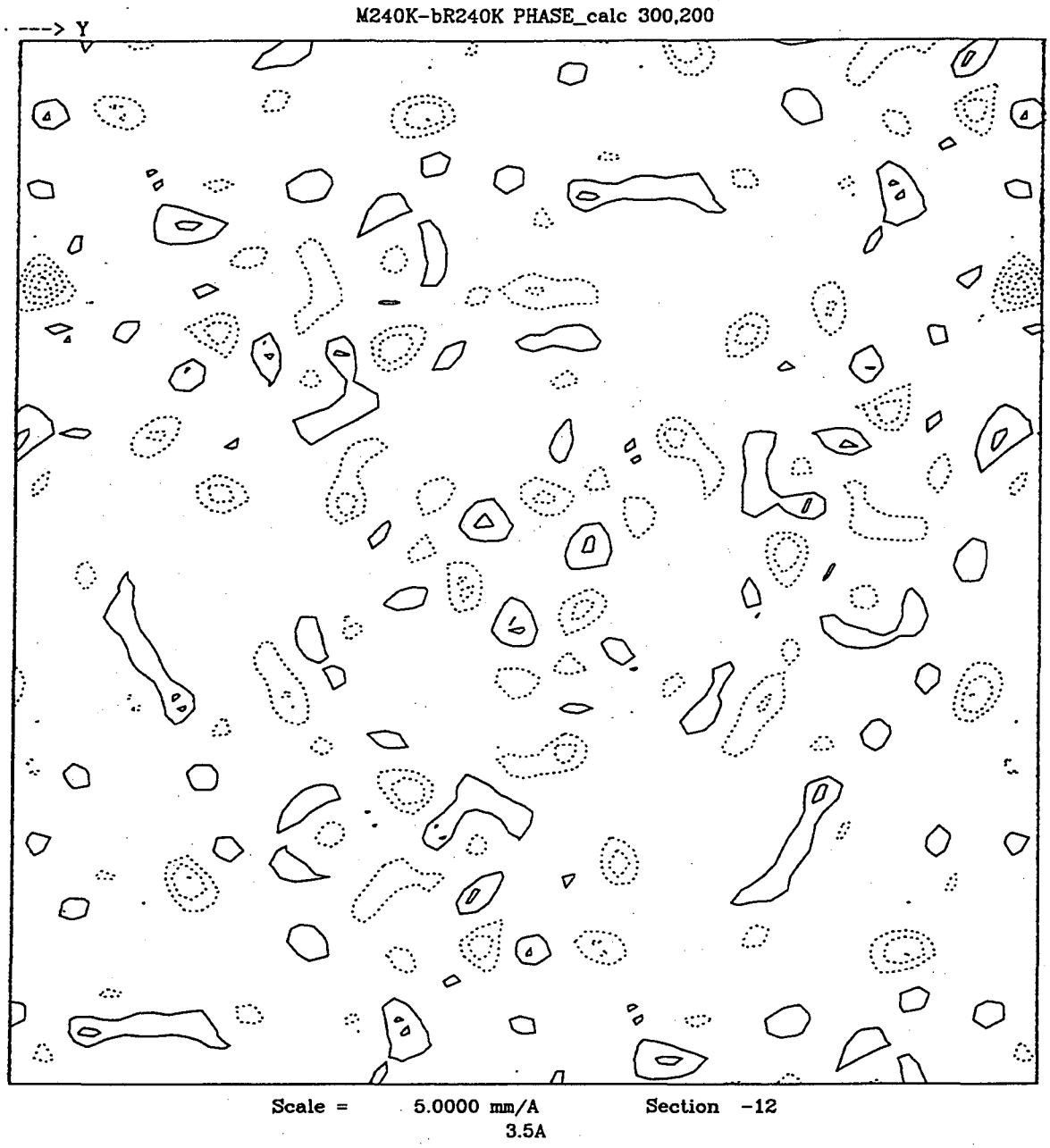

Position along z axis: **-34 Å**

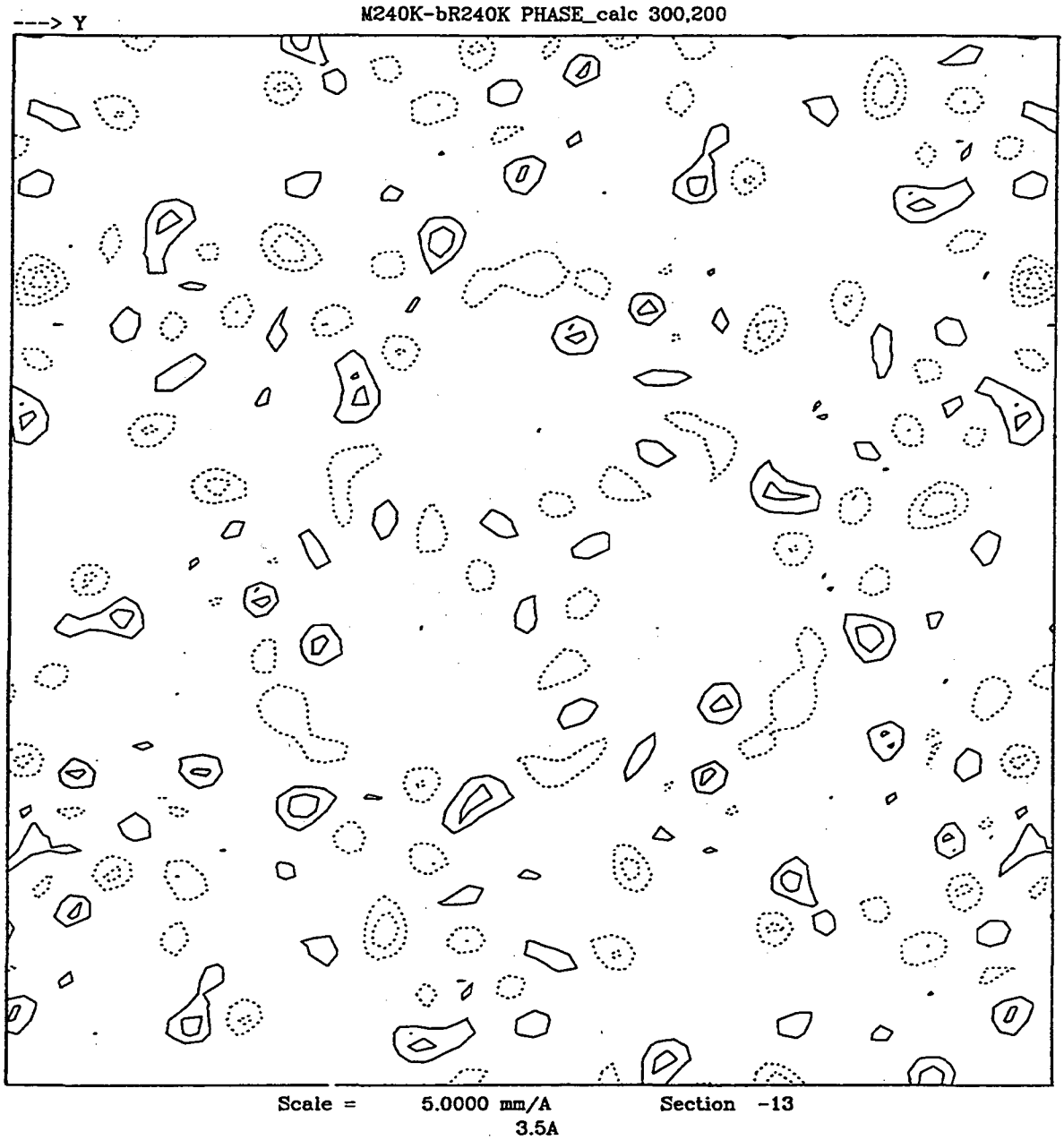

Position along z axis: **-36 Å**

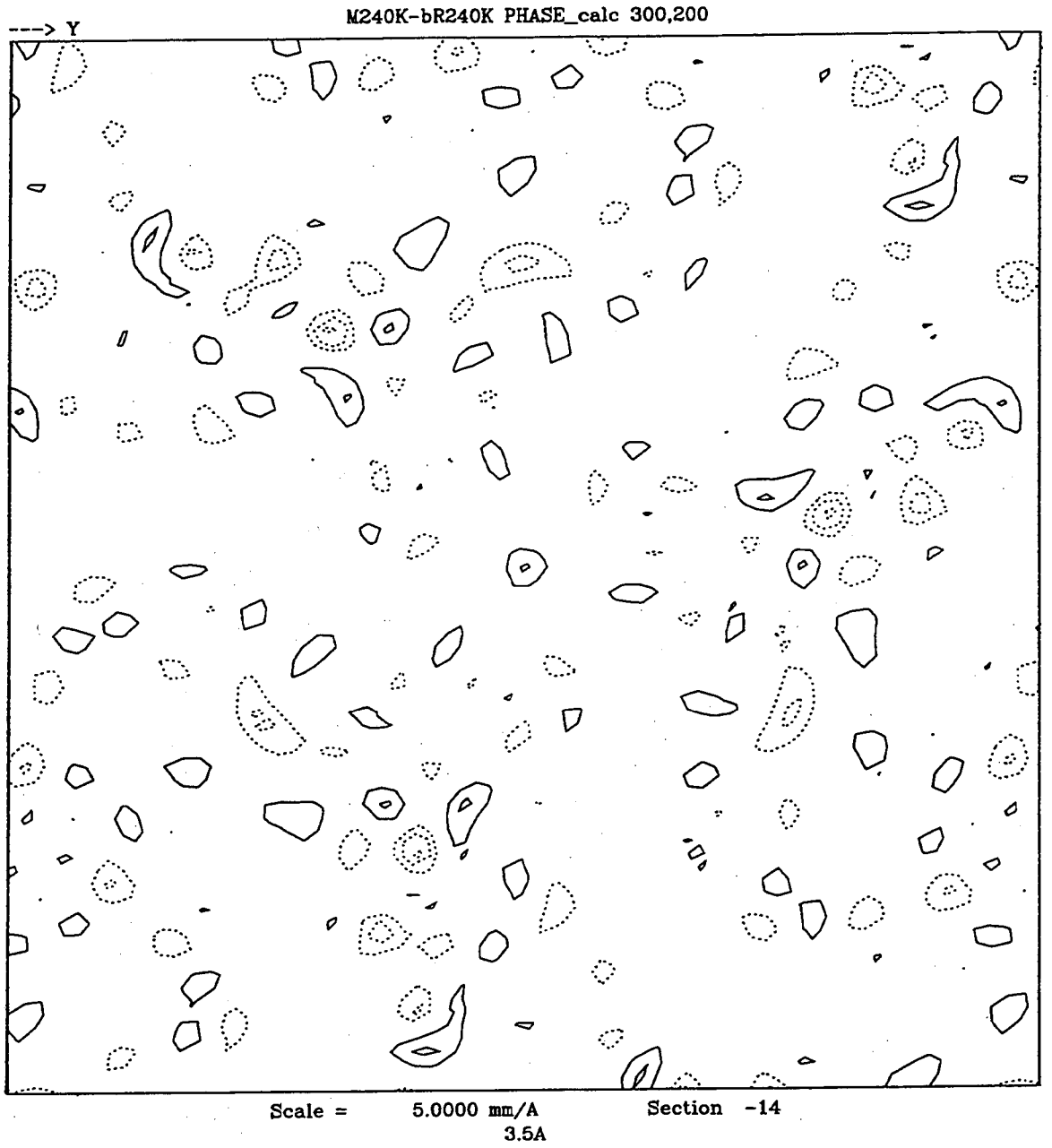

Position along z axis: **-39 Å**

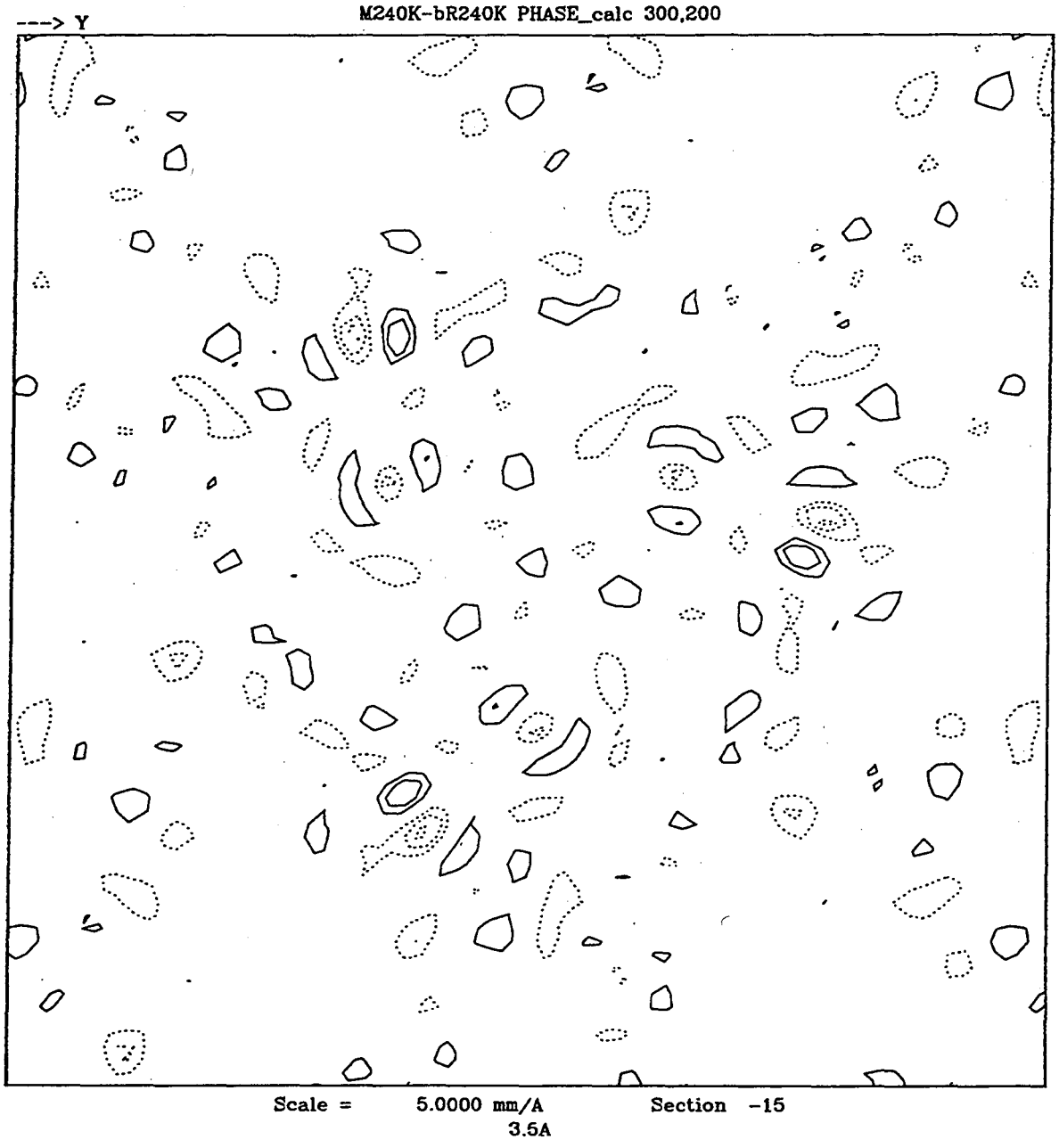

Position along z axis: **-42 Å**

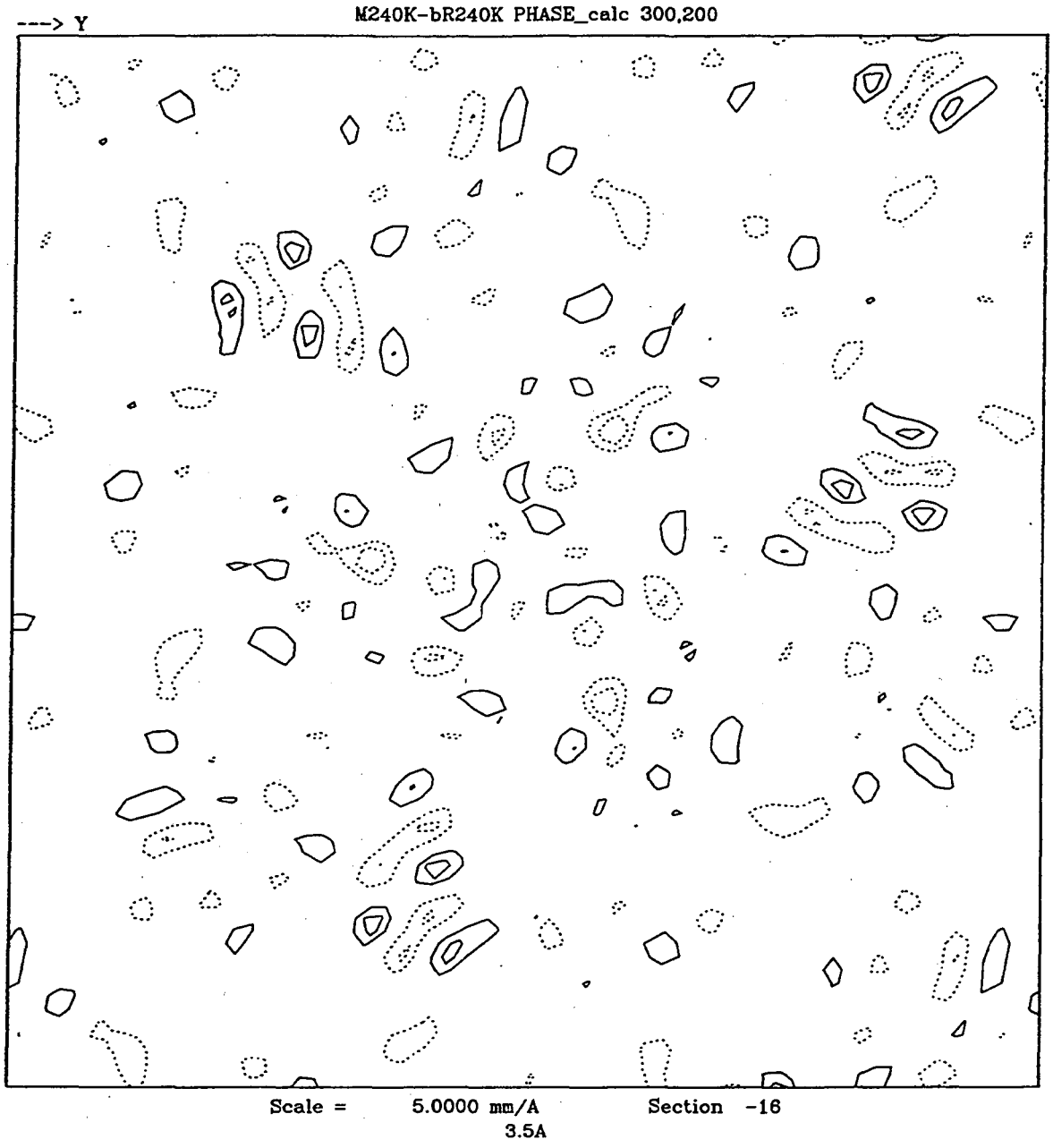

Position along z axis: **-45 Å**

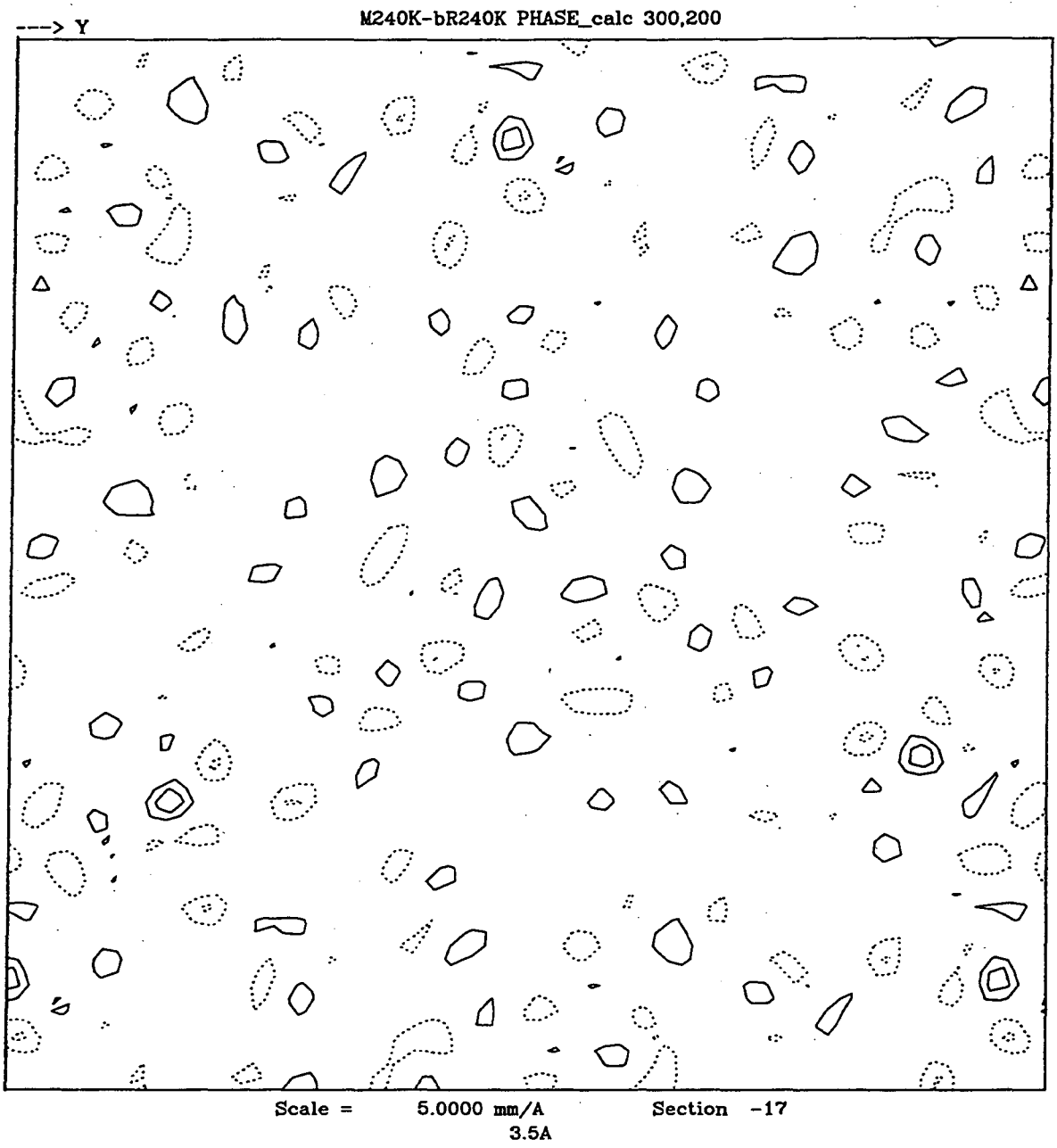

Position along z axis: **-48 Å**

REFERENCES

Amos, L. A., R. Henderson, and P. N. T. Unwin. 1982. Three-dimensional structure determination by electron microscopy of two-dimensional crystals. 1982. *Prog. Biophy. Molec. Biol.* 39:183-231.

Baldwin, J., and R. Henderson. 1984. Measurement and evaluation of electron diffraction patterns from two-dimensional crystals. *Ultramicroscopy.* 14:319-336.

Baldwin, J. M., R. Henderson, E. Beckman, and F. Zemlin. 1988. Images of purple membrane at 2.8Å resolution obtained by cryo-electron microscopy. *J. Mol. Biol.* 202:585-591.

Bamberg, E., J. Tittor, and D. Oesterhelt. 1993. Light-driven proton or chloride pumping by halorhodopsin. *Proc. Natl. Acad. Sci. USA.* 90:639-643.

Blanck, A., and D. Oesterhelt. 1987. The halo-opsin gene. II. Sequence, primary structure of halorhodopsin and comparison with bacteriorhodopsin. *EMBO J.* 6:265-273.

Blank, A., D. Oesterhelt, E. Ferrando, E. S. Schegk, and F. Lottspeich. 1989. Primary structure of sensory rhodopsin I, a prokaryotic photoreceptor. *EMBO J.* 8:3963-3971.

Booy, F. P., and J. B. Pawley. 1993. Cryo-crinkling: what happens to carbon films on copper grids at low temperature. *Ultramicroscopy.* 48:273-280.

Bousche, O., E. N. Spudich, J. L. Spudich, and K. J. Rothschild. 1991. Conformational changes in sensory rhodopsin I: Similarities and differences with bacteriorhodopsin, halorhodopsin, and rhodopsin. *Biochemistry.* 30:5395-5400.

Braiman, M. S., and R. Mathies. 1982. Resonance Raman spectra of bacteriorhodopsin's primary photoproduct: evidence for a distorted 13-cis retinal chromophore. *Proc. Natl. Acad. Sci. USA.* 79:403-407.

Brown, L. S., L. Bonet, R. Needleman, and J. K. Lanyi. 1993. Estimated acid dissociation constants of the Schiff base, Asp-85, and Arg-82 during the bacteriorhodopsin photocycle. *Biophys. J.* 65:124-130.

Brünger, A. T. 1992. Free R value: a novel statistical quantity for assessing the accuracy of crystal structures. *Nature.* 355:472-475.

Butt, H.-J., D. N. Wang, P. K. Hansma, and W. Kühlbrandt. 1991. Effect of surface of roughness of carbon support films on high-resolution electron diffraction of two-dimensional protein crystals. *Ultramicroscopy*. 36:307-318.

Cao, Y., G. Varo, M. Chang, B. Ni, R. Needleman, and J. Lanyi. 1991. Water is required for proton transfer from Aspartate-96 to the bacteriorhodopsin Schiff base. *Biochemistry*. 30:10972-10979.

Chiu, W., M. F. Schmid, and B. V. V. Prasad. 1993. Teaching electron diffraction and imaging of macromolecules. *Biophys. J.* 64:1610-1625.

Chou, K.-C. 1993. Conformational changes during the photocycle of bacteriorhodopsin and its proton-pumping mechanism. *Journal of Protein Chemistry*. 12:337-350.

Danon, A., and W. Stoeckenius. 1974. Photophosphorylation in *Halobacterium halobium*. *Proc. Natl. Acad. Sci. USA*. 71:1234-1238.

Deamer, D. W., and J. W. Nichols. 1989. Proton flux mechanisms in model and biological membranes. *J. Membrane Biol.* 107:91-103.

Dencher, N., G. Dresselhaus, G. Zaccai, and G. Buldt. 1989. Structural changes in bacteriorhodopsin during photon translocation revealed by neutron diffraction. *Proc. Natl. Acad. Sci. USA.* 86:7876-7879.

DeRosier D. J. 1993. Turn-of-the-century electron microscopy: Electron crystallography is becoming increasingly successful as a technique for solving biological macromolecular structures at up to atomic resolution. *Current Biology.* 3:690-692.

Draheim, J. E., and J. Cassim. 1985. Large scale global structural chages of the purple membran during the photocycle. *Biophysical Journal.* 47:497-507.

Fodor, S., J. Ames, R. Gebhard, E. V. D. Berg, W. Stoeckenius, J. Lugtenberg, and R. Mathies. 1988. Chromophore structure in bacteriorhodopsin's N intermediate: Implications for the proton pumping mechanism. *Biochemistry.* 27:7097-7101.

Fodor, S. P. A., R. Gebhard, J. Lugtenburg, R. A. Bogomolni, R. A. Mathies. 1989. Structure of the retinal chromophore in sensory rhodopsin I from resonance Raman spectroscopy. *J. Biol. Chem.* 264:18280-18283.

Glaeser, R. M., and K. A. Taylor. 1978. Radiation damage relative to transmission electron microscopy of biological specimens at low temperature: a review. *Journal of Microscopy.* 112:127-138.

Glaeser, R. M. 1982. Electron microscopy. *Methods Exptl. Phys.* 20:391-444.

Glaeser, R. M., J. M. Baldwin, T. A. Ceska, and R. Henderson. 1986. Electron diffraction analysis of the M412 intermediate of bacteriorhodopsin. *Biophys. J.* 50:913-920.

Glaeser, R. M., L. Tong, and S.-H. Kim. 1989. Three-dimensional reconstruction from incomplete data: interpretability of density maps at "atomic" resolution. *Ultramicroscopy.* 27:307-318.

Glaeser, R. M., and K. H. Downing. 1990. The "specimen flatness" problem in high-resolution electron crystallography of biological macromolecules. *Proc. XIIth Int. Congr. El. Micr.* Vol. 1. pp 98-99.

Glaeser, R. M., A. Zilker, M. Radermacher, H. E. Gaub, T. Hartmann, and W. Baumeister. 1991. Interfacial energies and surface-tension forces involved in the preparation of thin, flat crystals of biological macromolecules for high-resolution electron microscopy. *Journal of Microscopy.* 161:21-45.

Glaeser, R. M. 1992. Specimen flatness of thin crystalline arrays: influence of the substrate. *Ultramicroscopy*. 46:33-43.

Glaeser, R. M. 1992. Electron crystallography of membrane proteins. Membrane proteins: structures, interactions and models. Kluwer Academic Publishers. pp:1-9.

Glaeser, R. M., and K. H. Downing. 1993. High-resolution electron crystallography of protein molecules. *Ultramicroscopy*. 52:478-486.

Han, B.-G. 1993. High resolution electron diffraction analysis of structural changes associated with the photocycle of bacteriorhodopsin. 51st Ann. Meet. M.S.A. pp:680-681.

Han, B.-G., J. Vonck, and R. M. Glaeser. 1994a. The bacteriorhodopsin photocycle: Direct structural study of two substates of the M-intermediate. Submitted for publication.

Han, B.-G., S. Wolf, J. Vonck, and R. M. Glaeser. 1994b. Specimen flatness in electron crystallography of glucose-embedded biological materials is affected significantly by the choice of carbon evaporation stock. Submitted for publication.

Han, B.-G., J. Vonck, K. H. Downint, T. Earnest, and R. M. Glaeser. 1994c. Structural changes in the bacteriorhodopsin M-state intermediates are limited to shifts at the single-residue level. In preparation.

Havelka, W. A., R. Henderson, J. A. W. Heymann, and D. Oesterhelt. 1993. Projection structure of halorhodopsin from *Halobacterium halobium* at 6 Å resolution obtained by electron cryo-microscopy. *J. Mol. Biol.* 234:837-846.

Hayward, S. B., and R. M. Glaeser. 1979. Radiation damage of purple membrane at low temperature. *Ultramicroscopy*. 4:201-210.

Hegemann, P., D. Oesterhelt, and M. Steiner. 1985. The photocycle of the chloride pump halorhodopsin. I: azide-catalyzed deprotonation of the chromophore is a side reaction of photocycle intermediates inactivating the pump. *EMBO J.* 4:2347-2350.

Henderson, R. and P. N. T. Unwin. 1975. Three-dimensional model of purple membrane obtained by electron microscopy. *Nature*. 257:28-32.

Henderson, R., J. M. Baldwin, T. A. Ceska, F. Zemlin, E. Beckmann, and K. H. Downing. 1990. Model for the structure of bacteriorhodopsin

based on high-resolution electron cryo-microscopy. *J. Mol. Biol.* 213:899-929.

Heyn, M. P., R. J. Cherry, and U. Muller. 1977. Transient and linear dichroism studies on bacteriorhodopsin: determination of the orientation of the 568 nm all-trans retinal chromophore. *J. Mol. Biol.* 117:607-620.

Heyn, M. P., J. Westerhausen, I. Wallat, and F. Seiff. 1988. High-sensitivity neutron diffraction of membranes; Location of the Schiff base end of the chromophore of bacteriorhodopsin. *Proc. Natl. Acad. Sci. USA.* 85:2146-2150.

Heymann, J. A. W., W. A. Havelka, and D. Oesterhelt. 1993. Homologous overexpression of a light-driven anion pump in an archaebacterium. *Mol. Microbiol.* 7:623-630.

Hoel, P. G. 1971. Introduction to Mathematical Statistics. Fourth Ed. John Wiley & Sons, New York. 164.

Holz, M., L. A. Drachev, T. Mogi, H. Otto, A. D. Kaulen, M. P. Heyn, V. P. Skulachev, and H. G. Khorana. 1989. Replacement of aspartic acid-96 by asparagine in bacteriorhodopsin slows both the decay of the M

intermediate and the associated proton movement. *Proc. Natl. Acad. Sci. USA.* 86: 2167-2171.

Huang, K., R. Radhakrishnan, H. Bayley, and G. Khorana. 1982. Orientation of retinal in bacteriorhodopsin as studied by cross-linking using a photosensitive analog of retinal. *J. Biol. Chem.* 257:13616-13620.

Jap, B. K., K. H. Downing, and P. J. Walian. 1990. Structure of PhoE porin in projection at 3.5 A resolution. *J. Struct. Biol.* 103:57-63.

Khorana, H. G. 1993. Two light-transducing membrane proteins: Bacteriorhodopsin and the mammalian rhodopsin. *Proc. Natl. Acad. Sci. USA.* 90:1166-1171.

Koch, M., N. Dencher, D. Oesterhelt, H. Phohn, G. Rapp, and G. Buldt. 1991. Time-resolved X-ray diffraction study of structural changes associated with the photocycle of bacteriorhodopsin. *EMBO J.* 10:521-526.

Kong, T. 1989. Reconstitution of halorhodopsin. Ph. D. thesis. University of California, Berkeley.

Kühlbrandt, W., and K. H. Downing. 1989. Two-dimensional structure of plant light-harvesting complex at 3.7 A resolution by electron crystallography. 1989. *J. Mol. Biol.* 207:823-828.

Kühlbrandt, W., and D. N. Wang. 1991. Three-dimensional structure of plant light-harvesting complex determined by electron crystallography. *Nature.* 350:130-134.

Lin, S. and R. Mathies. 1989. Orientation of the protonated Schiff base group in bacteriorhodopsin from absorption linear dichroism. Biophysical J. 56:653-660.

Lozier, H. L., and W. Niederberger. 1977. The photochemical cycle of bacteriorhodopsin. *Fed. Proc.* 36:1805-1809.

Martelli, S., J. Urban, and B. Tesche. 1983. Carbon clusters in an electron beam evaporator. *Thin Solid Films.* 105:49-60.

Mathies, R. A., S. W. Lin, J. B. Ames, and W. T. Pollard. 1991. From femtoseconds to biology: Mechanisms of bacteriorhodopsin's light-driven proton pump. *Annu. Rev. Biophys. Chem.* 20:491-518.

Michel, H., and D. Oesterhelt. 1980. Three-dimensional crystals of membrane proteins: Bacteriorhodopsin. *Proc. Natl. Acad. Sci. USA.* 77:1283-1285.

Nakasako, M., M. Kataoka, Y. Amemiya, and F. Tokunaga. 1991. Crystallographic characterization by X-ray diffraction of the M-intermediate from the photo-cycle of bacteriorhodopsin at room temperature. *FEBS Lett.* 292:73-75.

Nagle, J. 1987. Theory of passive proton conductance in lipid bilayers. *J. Bioenerg. Biomembr.* 19:413-426.

Nagle, J. M. and M. Mille. 1981. Molecular models of proton pumps. *J. Chem. Phys.* 74:1367-1372.

Needleman, R., M. Chang, B. Ni, G. Varo, J. Fornes, S. H. White, and J. K. Lanyi. 1991. Properties of Asp^{212}->Asn bacteriorhodopsin suggest that Asp^{212} and Asp^{85} both participate in a counterion and proton acceptor complex near the Schiff base. *J. Biol. Chem.* 266:11478-11484.

Oesterhelt, D., and W. Stoeckenius. 1971. Rhodopsin-like protein from the purple membrane of *Halobacterium halobium. Nature New Biol.* 233:149-152.

Oesterhelt, D., J. Tittor, and E. Bamberg. 1992. A unifying concept of ion translocation by retinal proteins. *J. Bioenerg. Biomembr.* 24:181-191.

Ormos, P. 1991. Infrared spectroscopic demonstration of a conformational change in bacteriorhodopsin involved in proton pumping. *Proc. Natl. Acad. Sci. USA.* 88:473-477.

Ormos, P., K. Chu, and J. Mourant. 1992. Infrared study of the L, M, and N intermediates of bacteriorhodopsin using the photoreaction of M. *Biochemistry.* 31:6933-6937.

Otto, H., T. Marti, M. Holz, T. Mogi, M. Lindau, H. G. Khorana, and M. P. Heyn. 1989. Aspartic acid-96 is the internal proton donor in the reprotonation of the Schiff base of bacteriorhodopsin. *Proc. Natl. Acad. Sci. U.S.A.* 86:9228-9232.

Otto, H., and M. P. Heyn. 1991. Between the ground- and M-state of bacteriorhodopsin the retinal transition dipole moment tilt out of the plane of the membrane by only 3°. *FEBS.* 293:111-114.

Perkins, G., F. Burkard, E. Liu, and R. M. Glaeser. 1993. Glucose alone does not completely hydrate bacteriorhodopsin in glucose-embedded purple membrane. *J. Microsc.* 169:61-65.

Perkins, G., E. Liu, F. Burkard, E. Berry, and R. M. Glaeser. 1992. Characterization of the conformational change in the M_1 and M_2 substates of bacteriorhodopsin by the combined use of visible and infrared spectroscopy. *J. Structural Biol.* 109:142-151.

Sakmar, T. P., R. R. Franke, and H. G. Khorana. 1989. Glutamic acid-113 serves as the retinylidene Schiff base counterion in bovine rhodopsin. *Proc. Natl. Acad. Sci. USA.* 86:8309-8313.

Sasaki, J., Y. Shichida, J. Lanyi, and A. Maeda. 1992. Protein changes associated with reprotonation of the Schiff base in the photocycle of Asp^{96} -> Asn bacteriorhodopsin. *J. Biol. Chem.* 267:20782-20786.

Schertler, G. F., C. Villa, and R. Henderson. 1993. Projection structure of rhodopsin. 1993. *Nature.* 362:770-772.

Schobert, B., J. K. Lanyi. 1982. Halorhodopsin is a light-driven chloride pump. *J. Biol. Chem.* 257:10306-10313.

Souviginier, G., and K. Gerwert. 1992. Proton uptake mechanism of bacteriorhodopsin as determined by time-resolved stroboscopic-FTIR-spectroscopy. *Biophys. J.* 63:1393-1405.

Spudich, J. L., and R. A. Bogomolni. 1984. Mechanism of color discrimination by a bacterial sensory rhodopsin. *Nature*. 312:509-513.

Stoeckenius, W. 1979. A model for the function of bacteriorhodopsin. In membrane transaction mechanisms. R. A. Cone and J. E. Dowling, editors. Raven Press, New York. 39-47

Subramaniam, S., M. Gerstein, D. Oesterhelt, and R. Henderson. 1993. Electron diffraction analysis of structural changes in the photocycle of bacteriorhodopsin. *EMBO J.* 12:1-8.

Tittor, J., C. Soell, D. Oesterhelt, H.-J. Butt, and E. Bamberg. 1989. A defective proton pump, point-mutated bacteriorhodopsin Asp96→Asn is fully reactivated by azide. *EMBO J.* 8:3477-3482.

Varo, G., and J. Lanyi. 1991a. Kinetic and spectroscopic evidence for an irreversible step between deprotonation and reprotonation of the Schiff base in the bacteriorhodopsin photocycle. *Biochemistry*. 30:5008-5015.

Varo, G., and J. Lanyi. 1991b. Thermodynamic and energy coupling in the bacteriorhodopsin photocycle. *Biochemistry*. 30:5016-5022.

Varo, G., and J. Lanyi. 1991c. Distortions in the photocycle of bacteriorhodopsin at moderate dehydration. *Biophys. J.* 59:313-322.

Vonck, J., B.-G. Han, F. Burkard, and R. M. Glaeser. 1994. Two progressive substates can be identified in glucose-embedded, wild-type bacteriorhodopsin. Submitted for publication.

Wan, C., J. Qian, and C. K. Johnson. 1993. Light-induced reorientation in the purple membrane. *Biophysical Journal*. 65:927-938.

Zimanyi, L, Y. Cao, M. Chang, B. Ni, R. Needleman, and J. K. Lanyi. 1992. The two consecutive M substates in the photocycle of bacteriorhodopsin are affected specifically by the D85N and D96N residue replacements. *Photochemistry and Photobiology*. 56:1049-1055.

LAWRENCE BERKELEY LABORATORY
UNIVERSITY OF CALIFORNIA
TECHNICAL INFORMATION DEPARTMENT
BERKELEY, CALIFORNIA 94720